EXPERIMENTAL INVESTIGATIONS AND DESIGN TOOL DEVELOPMENT FOR SURFACE WATER HEAT PUMP SYSTEMS

By

MATT SANDY MITCHELL

Bachelor of Science in Mechanical Engineering
Brigham Young University—Idaho
Rexburg, Idaho
2010

Submitted to the Faculty of the
Graduate College of
Oklahoma State University
in partial fulfillment of
the requirements for
the Degree of
MASTER OF SCIENCE
May, 2014

EXPERIMENTAL INVESTIGATIONS AND DESIGN TOOL DEVELOPMENT FOR SURFACE WATER HEAT PUMP SYSTEMS

Thesis Approved:

Jeffrey D. Spitler

Thesis Advisor

Daniel E. Fisher

Lorenzo Cremaschi

ACKNOWLEDGMENTS

To my wife, Shelley: thank you for your love, support, and encouragement through the long hours and late nights.

To my children, Lily and Levi: thank you for your bright eyes and smiling faces to greet me daily.

To my parents, Sandy and Linda Mitchell: thank you for constantly encouraging me and guiding me throughout my life.

To my advisor, Jeffrey Spitler: thank you for your constant example of excellence and for your unparalleled knowledge and guidance.

To the many others who contributed to this work: thank you!

I would also like to extend thanks to several organizations for the funding and other financial support provided during this work. Thanks to go to ASHRAE for funding the research project (1385-RP) under which this work was performed. Thanks also go to the Conoco-Phillips Graduate Research Fellowship, and the Collins Fellowship for the generous support provided during this work.

Acknowledgments reflect the views of the author and are not endorsed by committee members or Oklahoma State University.

Name: MATT SANDY MITCHELL

Date of Degree: MAY, 2014

Title of Study: EXPERIMENTAL INVESTIGATION AND DESIGN TOOL DEVELOPMENT FOR SURFACE WATER HEAT PUMP SYSTEMS

Major Field: MECHANICAL AND AEROSPACE ENGINEERING

This study reports on experiments which were performed on spiral-helical surface water heat exchangers. These heat exchangers, when used as part of a geothermal heat pump system, serve as an alternative means whereby the system can reject heat to or extract heat from the environment. These systems are known as surface water heat pump systems and they serve as a less expensive, yet effective application of geothermal energy. Prior to this work, there was little information available to designers of surface water heat pump system regarding the performance of these heat exchangers. This work serves to bridge some of the remaining gaps by correlating heat exchanger performance in heat rejection and heat extraction modes of operation. From these correlations, design graphs were developed to allow designers of surface water heat pump systems to accurately size the surface water heat exchanger.

TABLE OF CONTENTS

LIST OF TABLES

LIST OF FIGURES

NOMENCLATURE

Acronyms/Abbreviations

dia.	Diameter
ft.	Feet
GHX	Ground heat exchanger
gpm	Gallons per minute
H	Horizontal
HDPE ...	High density polyethylene
in.	inch
lb	Pound
MBTUh .	1,000 British Thermal Units
N	Newton
PG	Propylene Glycol
SDR	Standard diameter ratio
SWC	Surface water cooling
SWHE ...	Surface water heat exchanger
SWHP ...	Surface water heat pump
TEHDPE	Thermally enhanced high density polyethylene
V	Vertical

Variables

A	Area (ft^2) [m^2]
A	Coefficent for Steinhart & Hart (1968) equation
B	Coefficent for Steinhart & Hart (1968) equation
C	Coefficent for Steinhart & Hart (1968) equation
D	Coefficent for Steinhart & Hart (1968) equation
c_p	Constant pressure specific heat (BTU/ft^2-°F) [J/kgK]
Δx	Horizontal tube-tube spacing from center-center (in.) [mm]
Δy	Vertical tube-tube spacing from center-center (in.) [mm]
Err	Error
F	Any function of multiple variables
g	Gravity (ft/s^2) [m/s^2]
k	Thermal conductivity (BTU/hr-ft-°F) [W/mK]
$\dot{m}$	Mass flow rate (lb./s) [kg/s]
L	Total tube length (ft) [m]
N	Number
NTU	Number of heat transfer units
Nu	Nusselt number
Pr	Prandtl number
$\dot{q}$	Heat flux (BTU/hr-ft^2) [W/m^2]
$\dot{Q}$	Heat transfer rate (BTU/hr) [W]

R ..... Thermal resistance (ft^2-hr-°F/BTU) [m^2K/W]
Ra^* ..... Modified Rayleigh number
Re ..... Reynolds number
t ..... Tube wall thickness
T ..... Temperature (°F) [°C]
U ..... Overall heat transfer coefficient (BTU/ft^2-hr-°F) [W/m^2K]
U ..... Experimental uncertainty
w ..... Independent uncertainty variable
x ..... Position along the tube
Function dependent variable

Greek Symbols

β ..... Volumetric coefficient of thermal expansion (1/°F) [$1/K$]
∂ ..... Partial derivative
Δ ..... Difference
ε ..... Heat exchanger effectiveness
ν ..... Kinematic viscosity (ft$^2/s$) [m$^2/s$]
Ω ..... Electrical Resistance (Ohms)
π ..... Pi
ρ ..... Density (lb/ft^3) [kg/m^3]

Subscripts

abs ..... Absolute Temperature (K)
ave ..... Average/Mean
bot ..... Bottom
cond ..... Conduction
conv ..... Convection
corr ..... Correlation
D ..... Diameter (in.) [mm]
f ..... Circulating fluid
exp ..... Experimental
film ..... Film
i ..... Inner
in ..... Inlet
lm ..... Log-mean
max ..... Maximum
MFT .... Mean fluid temperature
meas .... Measured
mid ..... Middle
n ..... Indexing variable
o ..... Outer
out ..... Outlet
p ..... Pipe
s ..... Surface
top ..... Top
tot ..... Total
sw ..... Surface water

CHAPTER 1

INTRODUCTION

1.1 Current Challenges in Space Conditioning

In this day and age, it is obvious that we wish to maintain a comfortable indoor environment. There are, however, other factors besides comfort that must be considered when looking at space conditioning systems. System performance, life cycle cost, and space requirements are just a few of the important aspects a designer will consider when selecting a heating or air-conditioning system. Another aspect of space conditioning system design that carries significant importance is environmental impact, which is directly related to system efficiency. Building owners, operators, and designers are increasing their awareness of building energy use and how it is affecting the environment around them. This is partially driven by rising energy costs, but also due to the fact that they generally desire to be good stewards of the energy their systems are using. Other programs and initiatives such as Energy Star, or Leadership in Energy and Environmental Design (LEED) have helped push "green" building and energy efficient design to the forefront of the building sciences.

In 2010, residential and commercial buildings used 41.1% of primary energy consumption in the United States. This was greater than all of industrial energy use (30.8%) or transportation energy use (28.1%) (DOE 2010). From those statistics, it should be fairly obvious that the energy consumed to maintain a comfortable indoor environment is significant. Even small changes in system efficiency and energy use will result in significant cost and environmental impacts.

1.2 Surface Water Cooling and Surface Water Heat Pump Systems

As a result of the "green" building movement, system designers are continuously looking for ways to make their designs more energy efficient, and thereby more environmentally friendly. One technology that is gaining acceptance in the built environment community is the use of surface water cooling or surface water heat pump systems. Surface water cooling or surface water heat pump systems are similar to geothermal heat pump systems in that they can use the earth's naturally occurring heat (or lack thereof) to meet heating or cooling loads. What makes these systems so attractive is that they can achieve very high levels of energy efficiency. In this study, 'geothermal energy' is defined as low enthalpy geothermal energy.

Surface water cooling (SWC) systems are systems that take cold water from a surface water body, i.e. ocean, lake, pond, or river, and dissipate the building's cooling load to the surface water. Surface water heat pump (SWHP) systems can dissipate heat from the building cooling load to surface water, but they can also extract heat from the surface water to satisfy a building heating load.

SWC and SWHP systems can be broken down into two main categories: open-loop systems and closed-loop systems. This section will describe the basic operation of each system type.

1.2.1 Open-loop Systems

Open-loop Surface Water Cooling Systems

Open-loop SWC systems take cold water from surface water bodies and use that water to meet a cooling load which can be seen in Figure 1.1. Here, we can see that cold water is taken from a surface water body and is piped into a wet sump pit. From there it is taken and pumped through an isolation heat exchanger who's purpose is to isolate the potentially contaminated open-loop from the closed circulation loop.

At the isolation heat exchanger, the cold water taken from the surface water body exchanges heat with the closed loop circulation system that directly meets the cooling load. Once the surface water passes through the isolation heat exchanger, it is then returned at a warmer temperature back to the surface water body.

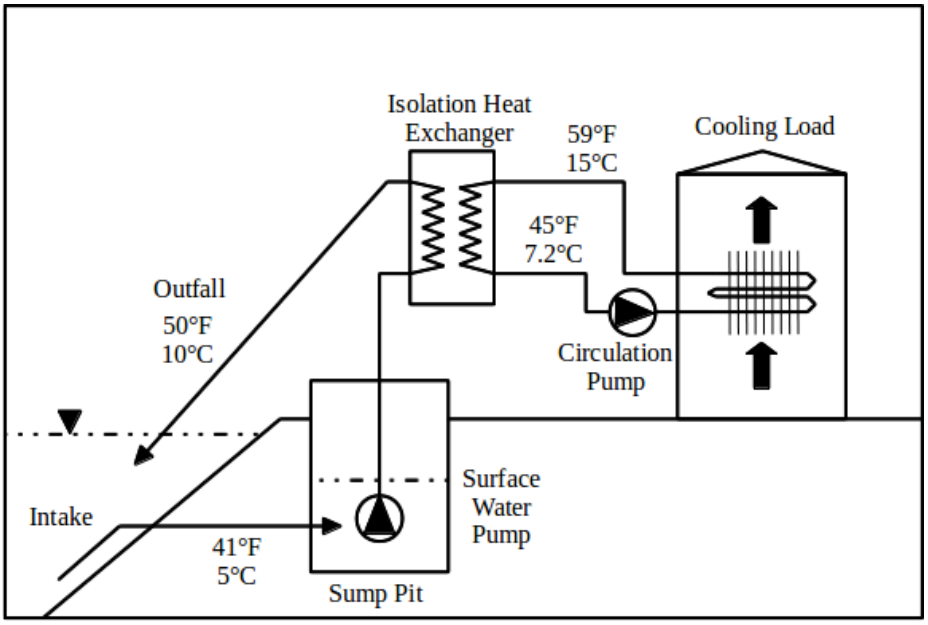

Figure 1.1: Open-loop direct surface water cooling system

The most prominent advantage of an open-loop SWC system is that no mechanical cooling equipment is required. This allows these systems to operate at exceptionally high values of system COP; system COP values above 25 have been reported (Peer 2012) for very large (20,000 ton (70.3 MW)) systems. The primary energy consumers are the circulation pumps and optimal system design depends heavily on intake piping and pumping design.

Open-loop SWC systems are, however, limited by the fact that they require cold surface water that is naturally occurring. Typical locations where this technology may be feasible are near the shores of deep lakes or oceans. An ideal location would be a deep lake or ocean with a steep shoreline bathymetry. This would allow for the placement of an intake pipeline that is as short as possible. Since the intake pipeline

is anticipated to be 50-85% of the total system cost (Ciani (1978) and Leraand & Van Ryzin (1995)), shorter intake pipelines will result in lower overall initial cost.

Another system limitation is the requirement that the system entering water temperature be sufficiently cold so that the load may be met. In order to meet the dehumidification requirements of a building cooling load, Ciani (1978) states that system entering water temperature should be 50°F (10°C) or lower. Kavanaugh & Pezent (1990) state that surface water can be used for direct cooling with surface water temperatures up to 55°F (12.8°C). Some sensible cooling can be accomplished with the use of warmer system entering water, but satisfying the latent dehumidification load may require other means.

Open-loop Surface Water Heat Pump Systems

Open-loop SWHP systems can meet a cooling load, however they also have the advantage that they can meet a heating load if designed properly and equipped with a reversible heat pump. An example of an open-loop SWHP system operating in cooling mode can be seen in Figure 1.2. Similar to the SWC system, the open-loop SWHP system takes water from a body of surface water and passes it through an isolation heat exchanger. This water then exchanges heat with a closed circulation loop which will then exchange heat with either the evaporator or condenser of a reversible heat pump. The heat pump then cools or heats another closed circulation loop that will then directly meet the heating or cooling load. Because the heat pump can operate in heating or cooling mode, the water returning to the surface water body can be warmer or cooler that it was originally.

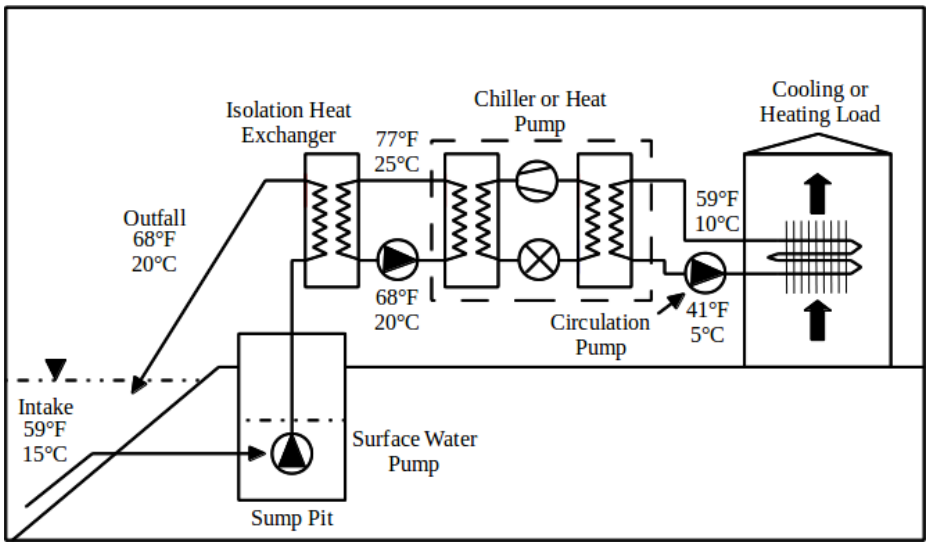

Figure 1.2: Open-loop surface water heat pump system

The primary advantage of an open-loop SWHP system is that meeting the cooling or heating load is less dependent on the conditions of the surface water. If the system entering water temperature is greater than what is required to meet the latent or sensible cooling load, the heat pump can make up the difference and allow the load to be met. Open-loop heat pump systems also do not have to overcome surface water heat exchanger thermal resistance. This can allow for system COP to be better than closed-loop systems.

The first disadvantage of an open-loop SWHP when compared to a open-loop SWC system is the initial cost of the heat pump. For very large systems, this cost will be significant, however, because the system is less dependent on entering system water conditions, the cost of the intake pipeline may be reduced thus offsetting the overall project cost. Another obvious disadvantage of this system type is the additional energy that must be consumed by the heat pump and additional circulation pump.

There are currently no studies that compare the life cycle costs of open-loop SWC or SWHP systems relative to more conventional cooling systems, such as a system with a chiller coupled with an evaporative cooling tower to meet the cooling load and

a natural gas boiler to meet the heating load. More work in this topic area would be useful.

1.2.2 Closed-loop Systems

Closed-loop Surface Water Cooling Systems

Closed-loop SWC systems function in a manner very similar to the open-loop SWC system that is indicated in Figure 1.1. Water or an anti-freeze solution is circulated between an isolation heat exchanger and a surface water heat exchanger (SWHE) that is submerged in a nearby surface water body. At the isolation heat exchanger, the two closed circulation loops can exchange heat to meet the cooling load. The now warmer surface water loop is then recirculated back to the SWHE where it can reject heat to the source water body.

Closed-loop SWC systems are uncommon. In fact, this author is only conscious of one instance where a hybrid closed-loop surface water cooling/surface water heat pump system has been installed. Lockhart (2013) stated that he had installed a system on a 15,000 ft^2 (1,394 m^2) private residence near Victoria, Canada. This system could be operated in direct cooling mode during summer months or in surface water heat pump mode for heating in winter months. Lockhart (2013) stated that summer seawater temperatures along the Pacific coast near Victoria Canada are around 52°F (11°C) during the summer months. At those temperatures, a good deal of space cooling can be accomplished. The system discussed was coupled to an in-floor hydronic system, and therefore no latent or dehumidification load could be satisfied by the system.

Closed-loop Surface Water Heat Pump Systems

Closed-loop SWHP systems function very similar to open-loop SWHP systems, except that the isolation heat exchanger and open-loop intake system are replaced by a closed

circulation loop and surface water heat exchangers. Water or anti-freeze solution circulates between the SWHE and the heat pump. The heat pump can then either accept heat from, or reject heat to the surface water loop based on the mode of operation. The heat pump can be a water-air heat pump and directly heat or cool the building space air, or it can be a water-water heat pump as indicated in Figure 1.3, which shows a schematic of a closed-loop SWHP system. By using a water-water heat pump, a single heat pump unit could provide heating or cooling to multiple zones.

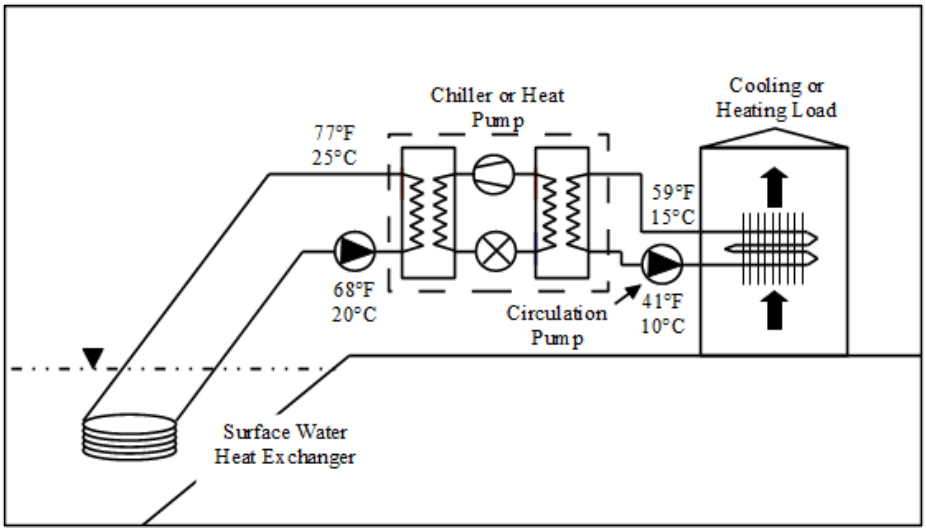

Figure 1.3: Closed-loop surface water heat pump system

An advantage of closed-loop SWHP systems is that they can operate in bodies of source water where the source water quality may be low. Open-loop system often require screening to prevent fish or other debris from being entrained into the intake, however, since the closed loop system doesn't directly circulate the source water, there are no screening requirements. They can also be operated in locations where the elevation difference, and thus, static head between the source water and the heat pump system is significant. Open-loop surface water pumps must be at or below source water body level in order to satisfy the net positive suction head requirements of the pump. If pump's required net positive suction head exceeds intake pipeline's

available net positive suction head, cavitation will occur at the pump inlet. Closed-loop systems do not require the pump be near the elevation of the source water body. Thus, greater elevation differences between heat pump system and source water level are possible.

Another important advantage of closed-loop SWHP systems when compared to open-loop SWHP systems is that they can operate with surface water loop temperatures at or below the freezing point of pure water. When the system is operated in heating mode, the system is extracting heat from the source water body. To do this, the heat pump must lower the surface water loop temperature below the temperature of the source water body. Often during winter months, surface water temperatures can approach freezing conditions (Kavanaugh & Rafferty (1997) and Selvakumar (2013)), especially in northern latitudes, which may cause loop temperatures to drop below the freezing point of pure water. In these applications, an anti-freeze solution is used as the heat transfer fluid in the surface water loop in anticipation of this.

1.3 Surface Water Heat Exchanger Overview

There are numerous surface water heat exchanger designs that have been developed over the years. Spiral-helical, plate, capillary, slinky, and embedded type heat exchangers is a short list surface water heat exchanger types. This study will focus primarily on spiral-helical heat exchangers with a brief description of plate heat exchangers.

1.3.1 Spiral-helical Heat Exchanger

Spiral-helical heat exchangers are a common heat exchanger type used for closed-loop SWHP systems. This is because they are typically constructed from HDPE pipeing which is an inherently inexpensive construction material. A picture of a spiral-helical SWHE can be seen in Figure 1.4. A central hub along with horizontal and vertical

tube-tube spacers can also be seen in Figure 1.4. The central hub is a jig that was built for the purpose of building spiral-helical SWHEs (Hansen 2011).

Figure 1.4: Photo of spiral-helical heat exchanger.*Reprinted, by permission, from Hansen (2011)*

Spiral-helical heat exchangers are constructed from straight HDPE tubing which then is formed into a coil. HDPE tubing lengths range typically from 300-500 ft. (91-152 m) in length. One way to form a spiral-helical coil is to begin by positioning horizontal tube spacers around a central hub. The straight tube is then taken and wrapped around the hub beginning at the center, and then wrapped outward in a spiral fashion until tubing is placed between all horizontal tube spacers. A row of vertical tube-tube spacers is then placed on top of the first horizontal "spiral" layer. The tubing is then taken upward one level in a "helical" fashion. The tubing is then wrapped back toward the center of the coil until the horizontal tube-tube spacers are full again and another "spiral" layer is completed. This is process is then repeated until the coil is constructed. Figure 1.5 shows a schematic of the spiral-helical SWHE. The section view of Figure 1.5 shows the consecutive tube numbers based on when they were placed in the coil. Also shown are the SWHE inside and outside diameters.

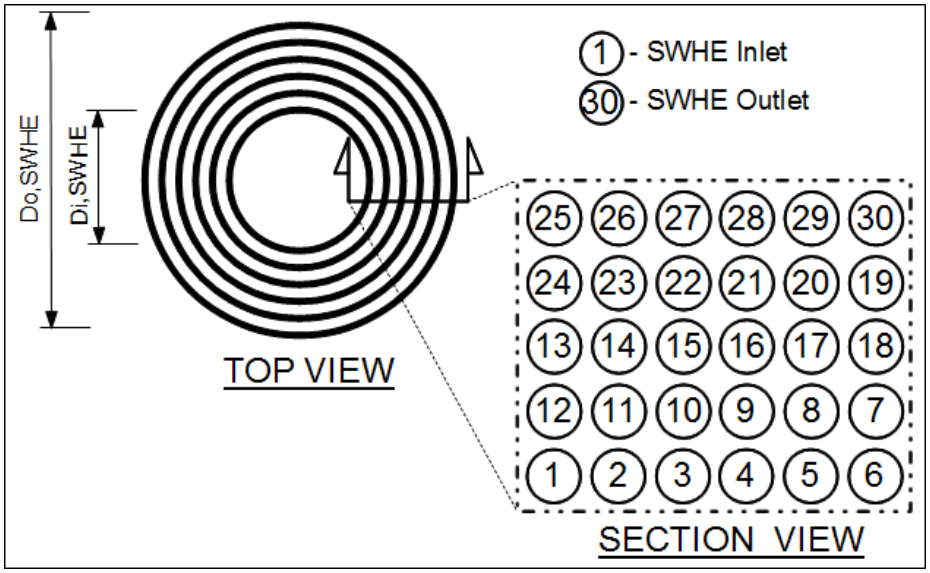

Figure 1.5: Schematic of spiral-helical heat exchanger

1.3.2 Plate Heat Exchanger

Plate type heat exchanges are also a very popular surface water heat exchanger type. Plate heat exchangers are typically constructed from stainless steel and they are placed vertically in the source water body. A 4 ft. x 5 ft. (1.2 m x 1.5 m), 4-pass, stainless steel plate heat exchanger can be seen in Figure 1.6. Also visible in Figure 1.6 are the small indents made through out the plate. These small indents are places where the two sides of the plate have been welded together. This helps maintain turbulent flow on the inside of the plate.

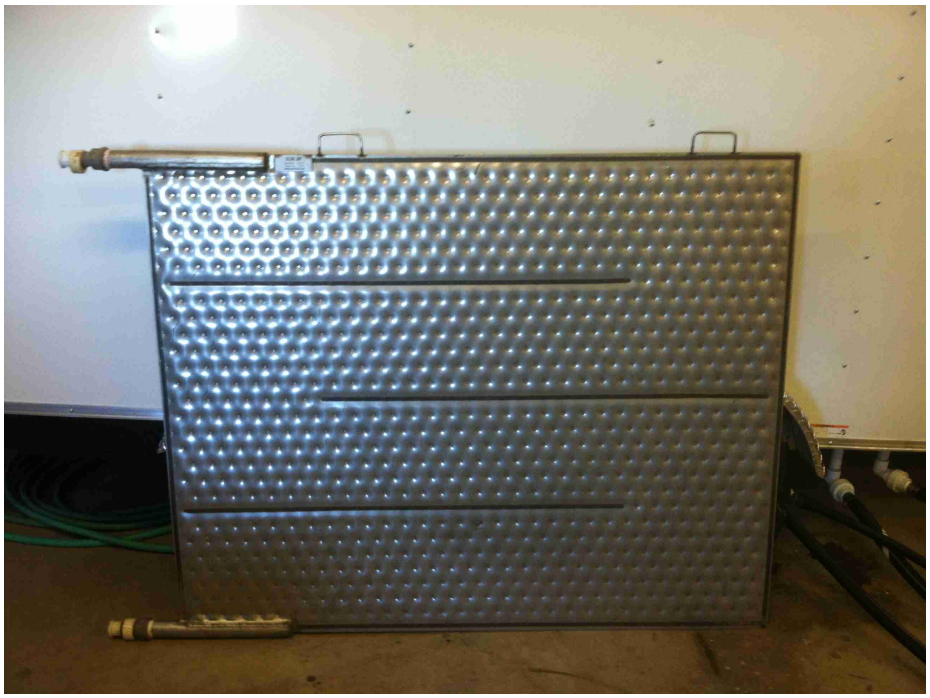

Figure 1.6: Stainless steel plate heat exchanger

Plate heat exchangers are often times the more popular heat exchanger type for larger commercial applications. The intensive labor involved with the construction and placement of spiral-helical, slinky, or other non-rigid type heat exchangers makes plate heat exchangers more attractive to SWHP system installers. This is because they can be arranged together relatively quickly into an array, attached to a frame, and lowered into position via crane. These frames also can keep the plate heat exchanger array elevated above the sediment at the bottom of the water source. Several plate heat exchanger arrays can be seen in Figure 1.7. A plate heat exchanger array can also be seen lifted into place via crane in Figure 1.8.

Figure 1.7: Plate heat exchanger arrays for home in Big Sky, MT. *Reprinted, by permission, from Terry Proffer*

Figure 1.8: Plate heat exchanger array being lifted into place with a crane. *Reprinted, by permission, from Terry Proffer*

1.4 Literature Review

1.4.1 Open-loop Systems

A journal article entitled: "Open-loop Surface Water Cooling and Surface Water Heat Pump Systems – A Review" was co-authored by the current author and published in the February 2013 issue of HVAC&R Research (Mitchell & Spitler 2013). In addition to what was covered in section 1.2, a few other notable points are:

Sumner (1948) described the first known open-loop surface water heat pump system used for space conditioning. This system used the River Wensum in the UK as the source water body. During the winter of 1945-46 it is said to have obtained a COP of 3.45 and provide a heating capacity of 800 MBTUh. It is unknown if the COP value is a system wide COP or a heat pump COP.

Since then, a variety of surface water cooling and surface water heat pump systems have been designed and constructed. In the year 2000, Cornell University began using direct surface water cooling to provide cooling for their entire campus (Peer & Joyce 2002). This system is capable of pumping 32,000 gpm (7,268 m^3/hr) from 250 ft. (76 m) beneath Lake Cayuga to provide up to 20,000 tons (70.3 MW) of peak cooling capacity. In 2010, the system COP was stated to be 25.8 (Peer 2012).

In the early 2000s, the City of Toronto in Ontario Canada completed work on a very large hybrid SWHP system (Heffernan 2001). The systems draws water from Lake Ontario at a temperature of 41°F (5°C). The water is then filtered and treated to be used as the city's potable water and sent to a heat exchange facility. There, the treated lake water exchanges heat with the closed loop chilled water distribution system. The direct surface water cooling portion of the system alone is capable of producing 40,000 tons (141 MW) cooling capacity. Bottoming chillers can then reduce the plant supply water temperature to 38°F (3.3°C) to give the system an additional 16,500 tons (58 MW) of cooling capacity (Eliadis 2003).

Additional information pertaining to pipeline, surface water pump, and heat exchanger design and material selection can be found treated in greater detail in Mitchell & Spitler (2013).

1.4.2 Closed-loop Systems

Prior to this work, there has been some information presented regarding the performance and design of closed-loop surface water heat pump systems, however, most of the information published was written in Swedish which limits its accessibility. Other information published in English by other authors is generally limited to handbook style design diagrams and is lacking in information which would be required for detailed calculations. A few of these works are summarized here.

Backlund (1982) described a system where 11 pieces of 164 ft. (50 m) long straight HDPE pipe with an outside diameter of 1.6 in. (40 mm) and a wall thickness 0.1 in. (2.5 mm) were connected together in parallel. The system was designed to extract heat from the lake bed to provide for space heating. This was done by capping the ends of a smaller diameter (OD 1.2 in. (28 mm)) tube, and then placing it inside of the larger tube. Because the inner tube is filled with air, it was buoyant therefore floated to the top of the inner surface of the larger pipe. The heat transfer fluid was then circulated in the interstitial space between the tubes with the intent of enhancing heat transfer from the pond bottom. The design was based on a heat extraction rate of 31-52 BTU/hr-ft (30-50 W/m). Some anecdotal information was given regarding the placement of the tubes. The author stated that placing the tubes on the bottom creates less interference opportunities for fish, boats, currents, ice, etc. No system performance information is given.

Svensson & Sörman (1982) performed heat extraction experiments in a 32 in. (80 cm) deep pool using 1-1/2 in. (40 mm) HDPE tubing. The project's objective was to determine the heat transfer rate from the surrounding water and lake bottom material

as a function of circulating fluid temperature. The experiments were performed in 32-39°F (0-4°C) stagnant water with varying mixtures of sand and organic-rich sediments to mimic natural lake bottom materials. Various degrees of pipe embedment into the base materials were also tested. An extensive theoretical discussion is given and the experimental results are presented as a series plots and charts for each different condition. Ice fouling of heat exchanger tubing is also discussed.

Svensson & Sörman (1983) performed a series of laboratory experiments on tubes placed in running water for heat uptake. An experiment was designed so that the angle between the tube axis and flow direction could be varied. Surface water flow velocity and temperature were also varied. The results were presented in a series of design graphs indicating the heat exchanger performance. The authors also presented experimentally derived outside Nusselt number correlations. The authors concluded that tube-tube spacing can be fairly narrow given that the surface water flow velocity is greater than 10 ft/min (5 cm/min). At slower flow velocities, tube-tube spacing should be expanded to 10-20 in. (25-51 cm).

A great amount of work relating to surface water heat pump systems can be found in Billfalk (1982), which is a compilation of conference papers presented in 1982. Here, a good deal of Swedish research from the period regarding surface water heat pump systems is compiled and summarized.

Kavanaugh (1991) presents some information regarding the design of surface water heat pump systems. The author discusses open and closed-loop systems. Seasonal lake behavior is briefly discussed as well as various coil designs. Also presented are several design diagrams that give required coil length in ft/ton as a function of the temperature drop across the coil. The author does not specify whether the design heat transfer rate indicated in the plots is the coil heat transfer rate or whether it is the space heat transfer rate.

Kavanaugh & Rafferty (1997) present what is likely the most comprehensive re-

source for surface water heat pump system design prior to the publication of Hansen (2011). Here, the authors briefly discuss seasonal lake temperature behavior. Several coil designs are presented and design graphs are presented which show required coil length in ft/ton as a function of approach temperature. Approach temperature is defined as the coil exiting fluid temperature minus the lake temperature. It is not stated whether the indicated heat transfer rate is a coil heat transfer rate or a space heat transfer rate. This approach also assumes that SWHP coils will perform equally at equal approach temperatures, regardless of lake temperature.

Hansen (2011) presents a comprehensive review of SWHP systems, surface water heat exchangers, and presents the most current information regarding these systems to date. The author performed testing on SWHP systems with a specific focus on determining performance of various types of SWHEs. The author provided a review of inside and outside convection correlations for SWHEs. From which, he recommended the correlation developed by Rogers & Mayhew (1964) for determining inside convection resistance. He also determined that there were no external convection correlations which were suitable for modeling of spiral-helical SWHE. In order to develop a suitable correlation, the author updated the experiment developed by Austin (1998) for SWHE testing. Several different varieties of surface water heat exchangers were tested. Specific to this work, the author (Hansen 2011) performed 528 heat rejection tests on spiral-helical SWHEs. From these tests, he developed an external convection correlation specific to spiral-helical SWHEs which is shown in Equation 1.1.

$$\mathrm{Nu}_{D,o} = 0.016\,\mathrm{Ra}_{D,o}^{*\,0.264}\left(\frac{\Delta y}{D_o}\right)^{0.078}\left(\frac{\Delta x}{D_o}\right)^{0.223} \tag{1.1}$$

From this, he developed several design diagram for sizing SWHE under heat rejection conditions. Design diagrams for different surface water heat exchager designs were also developed and presented. All work was performed under space cooling, or heat rejection conditions.

1.5 Scope of Study

The work conducted by Hansen (2011) was taken as a starting point for this work because both projects were funded under the same ASHRAE research grant, RP-1385. Because of the continuous nature of the research, this study aims to bridge some of the remaining information gaps for surface water heat pump systems.

In this study, experimental testing was performed on spiral-helical surface water heat exchangers. Several spiral-helical heat exchanger geometries were tested under heat rejection conditions. These tests were used to augment the Hansen (2011) data set for heat rejection conditions. From there a space heating, or heat extraction, experiment was then constructed with the intent of determining spiral-helical SWHE performance under heat extraction conditions.

From these experiments, the convection correlation shown in Equation 1.1 was updated based on the additional data collected. Additional correlation were also developed for heat extraction and recommendations are given. This information was then implemented in a simulation to develop design tools that can be used for handbook style heat exchanger sizing.

CHAPTER 2

EXPERIMENTAL FACILITY, APPARATUS, AND METHOD

2.1 Heat Rejection Experiments

2.1.1 Facility

Experiments on the SWHEs under heat rejection conditions were performed at the Oklahoma State University test pond. The test pond can be seen in Figure 2.1. The test pond is a three acre pond with a maximum depth of 14 ft. (4.3 m). It was constructed around the year 2000 (Liu et al. 2003). Also constructed around the year 2000 was the "Smart Bridge" which was used to test the effectiveness of a surface water heat pump system at bridge deck de-icing. This bridge deck is approximately 25 ft. (7.6 m) wide, 75 ft. (22.9 m) long, and extends roughly 50 ft. (15.2 m) out into the pond when the pond is full. This bridge deck can be seen in Figure 2.2. The pond was selected as the best location for conducting experiments on SWHEs because semi-actual operating conditions could be achieved. Semi-actual operating conditions are defined as conditions which are consistent with what would occur in an actual installation. The conditions include exposure to environmental conditions, such as: wind, rain, sun, underwater currents, etc.

(a) View of test pond looking to the South-east

(b) View of test pond looking to the South

Figure 2.1: Test pond

(a) View of bridge deck looking to the South-east

(b) Close view of bridge deck

Figure 2.2: Bridge deck at test pond

2.1.2 Apparatus

A mobile testing trailer previously utilized by Austin (1998) for ground thermal conductivity testing was retrofitted for SWHE testing by Hansen (2011) and was parked on the bridge deck. The mechanical and data recording equipment such as circulation pumps, flow meter, electric water heaters, valves, purge tank, purge pumps, and data loggers were all located inside the trailer situated on the bridge deck.

Figure 2.3a shows a schematic of the equipment and piping inside of the in-situ testing trailer used for the heat rejection tests. A photo of the equipment can be seen in Figure 2.3b. Once the heaters and the SWHE were purged of air, the 3-way valves

were oriented so that the fluid circulated in a closed loop. The circulating fluid would then cascade across three electrical resistance heaters arranged in series and dissipate the heat via the SWHE.

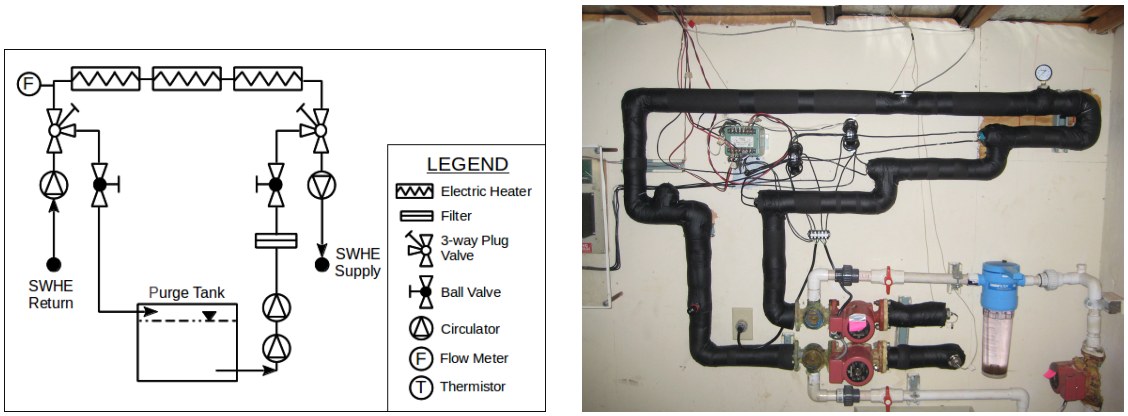

(a) Schematic of heat rejection equipment in trailer.

(b) Equipment inside heat rejection trailer. *Reprinted, by permission, from Hansen (2011)*

Figure 2.3: Heat rejection trailer equipment

The SWHE was placed on a support frame and then placed in the pond. The support frame was supported from the water surface by buoys. This method of supporting the SWHE from the water surface allowed the depth of the SWHE to be controlled accurately. It also allowed the SWHE depth relative to the water surface to remain at a fixed distance. On hot summer days in Oklahoma, the test pond depth could drop one-half to one inch (12-25 mm) each day due to evaporation. Supporting the SWHE from the water surface using buoys allowed the SWHE to remain a fixed distance from the water surface at all times. The SWHE was also anchored in place in the pond to prevent wind or underwater currents from causing the SWHE to move in the pond. A schematic of the SWHE in the pond can be seen in Figure 2.4.

Figure 2.5a and shows a spiral-helical coil on land prepared for testing while Figure 2.5b shows the coil in place in the pond during a test. Also visible in Figure 2.5b, are three vertical tubes which were placed on the coil support frame 120° apart from each other. The bottom of the tubes were placed at the bottom of the SWHE, and

from there were marked at the submersion depth. This provided a visual means by which the depth of the coil could be verified which would occur once the marks were even with the water surface.

The flow rate was measured by a calibrated turbine flow meter. In-pipe thermistors were placed at the inlet and outlet of the SWHE to measure entering and exiting fluid temperatures. An in-pipe thermistor can be seen in Figure 2.6. The pond temperature was also measured at the bottom, middle, and top of the coil at a distance of 4 ft. (1.2 m) away from the SWHE. The L-arm attached to the SWHE coil frame can be seen Figure 2.7 and is where the local thermistors were placed in order to measure the local pond water temperature. The pond temperature was averaged from the three temperature measurements to determine the lake temperature. This is shown in Equation 2.1.

$$T_{sw} = \frac{T_{top} + 2 \cdot T_{mid} + T_{bot}}{4} \tag{2.1}$$

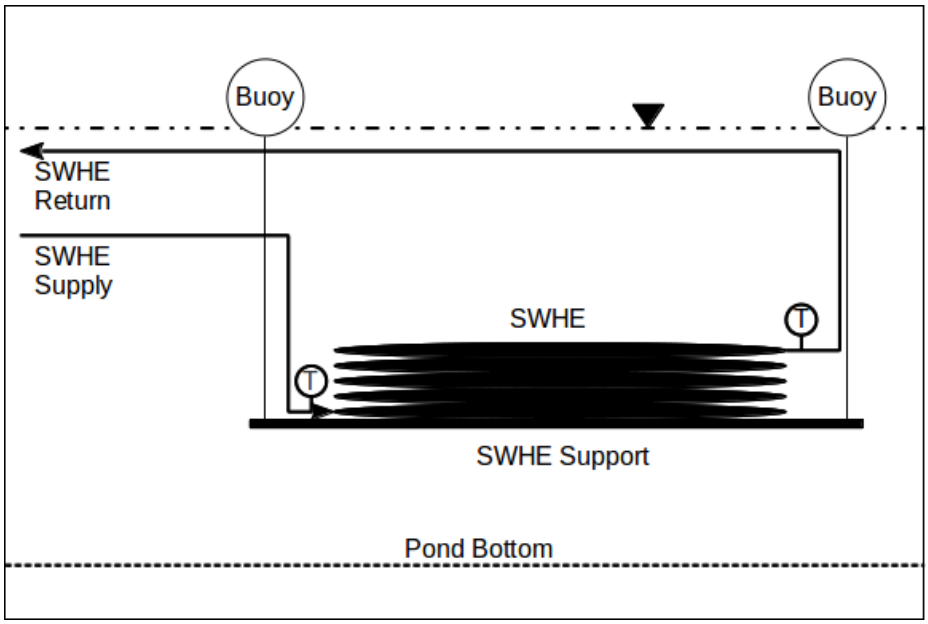

Figure 2.4: Schematic of heat rejection experiment in pond

(a) Spiral-helical surface water heat exchanger prepared for testing.

(b) Coil in test pond during test.

Figure 2.5: Surface water heat exchanger

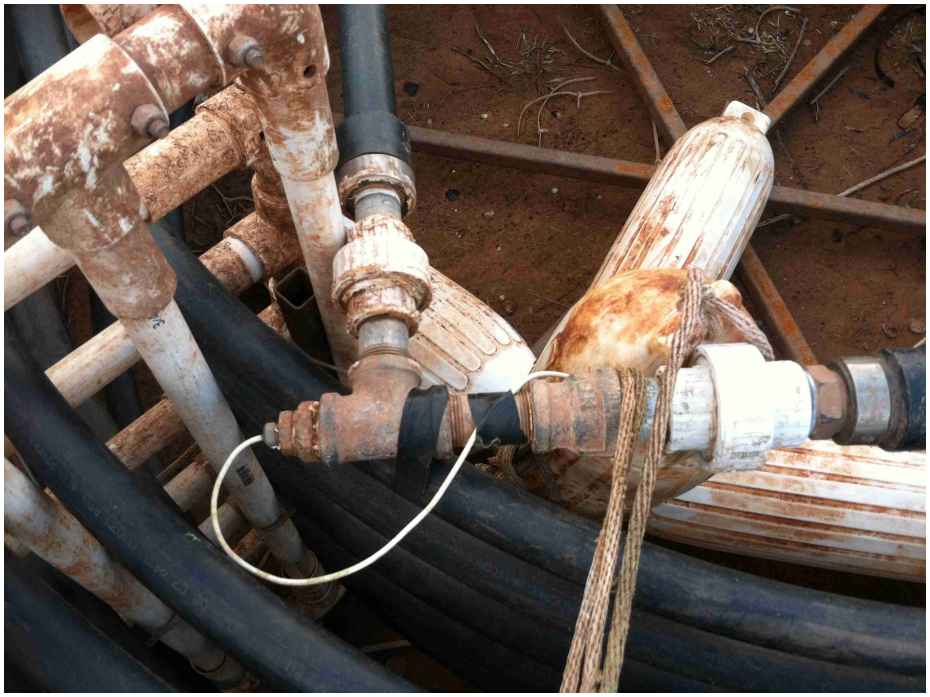

Figure 2.6: In-pipe thermistor used to measure the entering or exiting fluid temperature

Figure 2.7: L-arm at a distance of 4 ft. (1.2 m) away from coil used for measuring local pond temperature

Additionally, 14 other thermistors were also placed in the pond on two vertical pipes at a distance of approximately 30 ft. (9.1 m) and 100 ft. (30.5 m) away from the SWHE. Beginning at the pond bottom, the thermistors were spaced 18 in. (46 cm) apart vertically allowing for the measurement of the pond temperature profile at two separate locations. Actual thermistor water depth was determined by measuring the pond water level from a reference datum and applying a calibration determine the thermistor depth relative to the water surface. The flow meter and thermistors were all connected to a data logger recording data at 10 second intervals.

2.1.3 Methodology

To conduct each heat rejection experiment, a series of three tests were run on each coil configuration. Each test was composed of a series of eight incrementally increasing heat input set points up to 3.5 tons (12.5 kW). Once each heat rate was set, the

experiment was allowed to run until steady state operating conditions were achieved, which was determined by examining the SWHE entering and exiting fluid temperature. Once steady state conditions were achieved, the experiment was allowed to run for another five minutes to collect data. The average of the data taken during the five minutes of steady state operation was then taken as the steady state operation point. The set point was then changed and the process repeated until the maximum heat rejection rate of 3.5 tons (12.5 kW) was reached and data collected.

A total of 27 spiral helical SWHE configurations were tested at the test pond. The nominal tube size was varied from 3/4 in. (19 mm), 1 in. (25 mm), and 1-1/4 in. (32 mm) SDR-11 HDPE. The smallest horizontal and vertical center-center tube spacing was varied from 1.3 in. (33 mm), 1.6 in. (41 mm), and 1.9 in. (48 mm) for each respective tube size. The medium and large horizontal and vertical center-center tube spacing was set at 2.625 in. (67 mm) and 4.125 in. (105 mm), regardless of tube size. Tables 2.1, 2.2, and 2.3 show the dates when each test series for each coil configuration was completed. Tables 2.4, 2.5, and 2.6 show the geometrical measurements for each respective spiral-helical SWHE coil configuration.

The testing and work performed on the spiral-helical SWHE are a continuation of work initiated by Hansen (2011). The tests indicated in *blue italics* are tests that occurred after the publication of Hansen (2011).

Table 2.1: 3/4 in. (19 mm) SDR-11 HDPE spiral-helical SWHE test summary

	Test Dates		
Vert/Horiz Spacing	1.3 in. (33 mm)	2.625 in. (67 mm)	4.125 in. (105 mm)
1.3 in. (33 mm)	4/19–4/20/11	3/28–3/29-11 4/8–4/11/11	3/8/11
2.625 in. (67 mm)	4/21/11	3/26–3/27/11 4/13–4/14/11	3/2–3/5/11
4.125 in. (105 mm)	4/22–4/25/11	3/30–4/1/11	3/17–3/18/11

Table 2.2: 1 in. (25 mm) SDR-11 HDPE spiral-helical SWHE test summary

	Test Dates		
Vert/Horiz Spacing	1.6 in. (41 mm)	2.625 in. (67 mm)	4.125 in. (105 mm)
1.6 in. (41 mm)	10/4–10/5/11	9/15/11	*11/17–11/18/11*
2.625 in. (67 mm)	*10/6–10/7/11*	9/7–9/8/11	*11/28–11/29/11*
4.125 in. (105 mm)	*10/12–10/13/11*	9/13/11	6/17–6/20/11

Table 2.3: 1-1/4 in. (32 mm) SDR-11 HDPE spiral-helical SWHE test summary

	Test Dates		
Vert/Horiz Spacing	1.9 in. (48 mm)	2.625 in. (67 mm)	4.125 in. (105 mm)
1.9 in. (48 mm)	*10/20–10/24/11*	6/20–6/22/11	9/20–9/21/11
2.625 in. (67 mm)	*10/26–10/31/11*	6/15–6/16/11	9/22/11
4.125 in. (105 mm)	*11/14–11/15/11*	*12/1–12/2/11*	9/26/11

Table 2.4: Geometry of 3/4 in. (19 mm) spiral-helical surface water heat exchangers

	Coil Heights		
Vert/Horiz Spacing	1.3 in. (33 mm)	2.626 in. (67 mm)	4.125 in. (105 mm)
1.3 in. (33 mm)	8.5 in. (21.6 cm)	7 in. (17.8 cm)	7 in. (17.8 cm)
2.625 in. (67 mm)	14.2 in. (36 cm)	14.2 in. (36 cm)	11.6 in. (29.5 cm)
4.125 in. (105 mm)	21.7 in. (55.1 cm)	21.7 in. (55.1 cm)	17.5 in. (44.5 cm)
Coil OD	5.5 ft. (1.7 m)		
Coil ID	4 ft. (1.2 m)		

Table 2.5: Geometry of 1 in. (25 mm) spiral-helical surface water heat exchangers

	Coil Heights		
Vert/Horiz Spacing	1.6 in. (41 mm)	2.626 in. (67 mm)	4.125 in. (105 mm)
1.6 in. (41 mm)	10 in. (25.4 cm)	8 in. (20.3 cm)	11 in. (28 cm)
2.625 in. (67 mm)	15 in. (38.1 cm)	12 in. (30.5 cm)	14 in. (35.6 cm)
4.125 in. (105 mm)	22 in. (55.6 cm)	17 in. (43.2 cm)	17 in. (43.2 cm)
Coil OD	6.5 ft. (2 m)		
Coil ID	4 ft. (1.2 m)		

Table 2.6: Geometry of 1-1/4 in. (32 mm) spiral-helical surface water heat exchangers

	Coil Heights		
Vert/Horiz Spacing	1.9 in. (48 mm)	2.626 in. (67 mm)	4.125 in. (105 mm)
1.9 in. (48 mm)	11 in. (28.9 cm)	10 in. (25.4 cm)	10 in. (25.4 cm)
2.625 in. (67 mm)	17 in. (43.2 cm)	14 in. (35.6 cm)	14 in. (35.6 cm)
4.125 in. (105 mm)	22 in. (55.9 cm)	18 in. (45.7 cm)	18 in. (45.7 cm)
Coil OD	8 ft. (2.4 m)		
Coil ID	4 ft. (1.2 m)		

2.2 Heat Extraction Experiments

2.2.1 Facility

Heat extraction tests performed on the spiral-helical SWHE were conducted at two separate locations. Testing began at the test pond which can be seen in Figure 2.1. However, because 2011 was one of the warmest years on record, the tests were moved indoors to a research facility with a more controlled environment. An exterior and interior view of the lab facility can be seen in Figures 2.8a and 2.8b, respectively. By extracting heat from the SWHE, we were expecting the SWHE surface temperature to drop below the freezing point of the pond water, thereby causing coil icing conditions. In order to create these conditions without sufficiently cold weather, the

experiment was moved to a location where the ambient temperature could be more readily controlled.

(a) Outside view of laboratory facility where indoor experiments were performed

(b) Inside view of laboratory facility where indoor experiments were performed

Figure 2.8: Test facility where indoor testing took place

2.2.2 Apparatus

To conduct experiments on spiral-helical SWHE under heat extraction conditions, a new trailer was purchased and the heat extraction experiment was constructed inside. This new trailer can be seen in Figure 2.9.

The heat extraction experiment consisted of two reversible heat pumps connected in parallel with a total nominal capacity of 4 tons (14.1 kW). One heat pump was a water-water heat pump with a nominal capacity of 3 tons (10.6 kW) while the remaining heat pump was a water-air heat pump with a nominal capacity of 1 ton (3.5 kW). Also part of the heat extraction experiment were circulation pumps, calibrated turbine flow meters, and multiple valves. In-pipe thermistors, as seen in Figure 2.6 were placed at the inlet and outlet of the condenser and evaporator sides of the heat pumps, as well as at the SWHE inlet and outlet. Data loggers were placed inside of the trailer to record the data. A photo of the inside of the heat pump trailer can be seen in Figure 2.10. A schematic of the heat extraction equipment located inside of the trailer can be seen in Figure 2.11.

Figure 2.9: Trailer purchased for heat extraction experiment

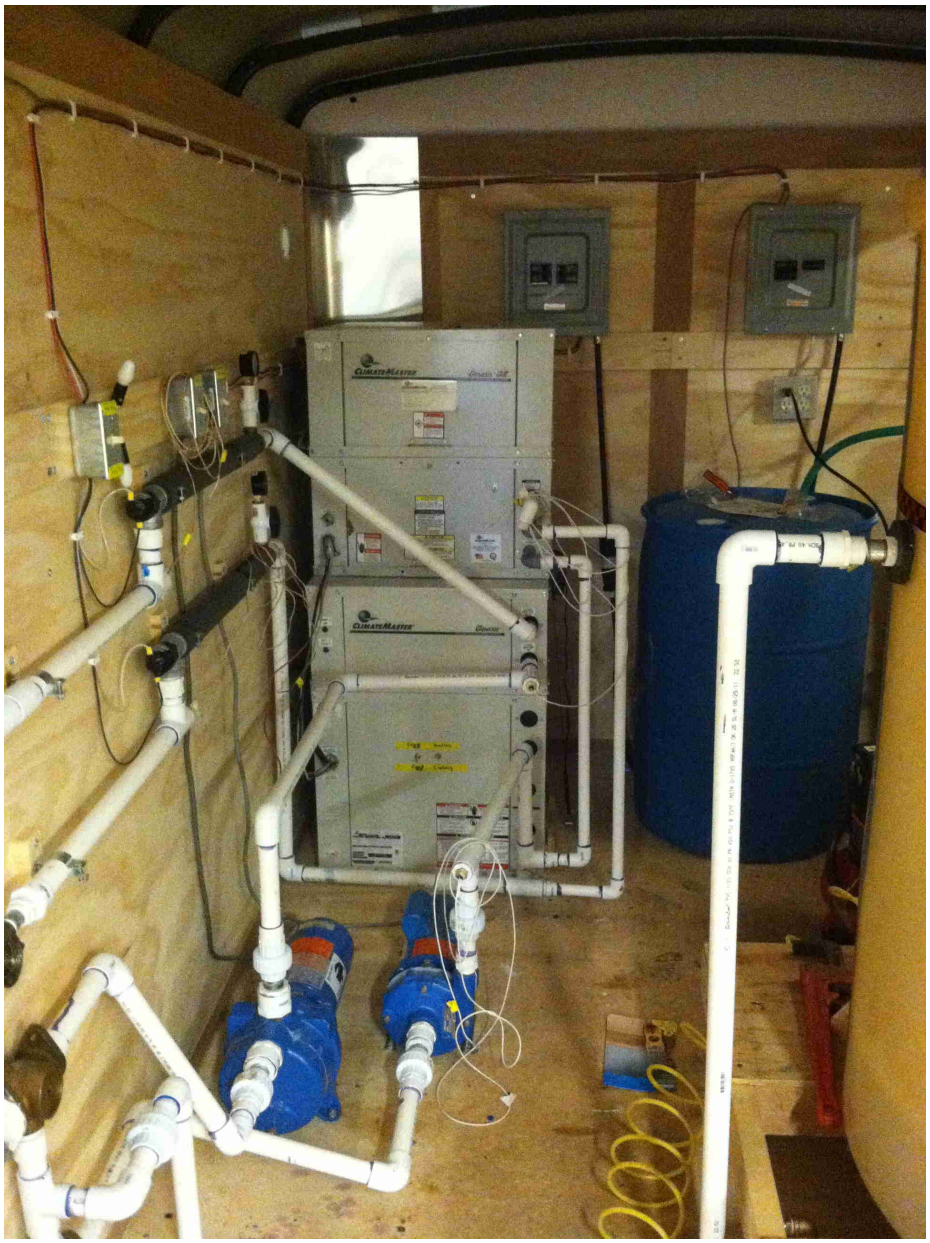

Figure 2.10: Heat extraction experiment constructed inside new trailer

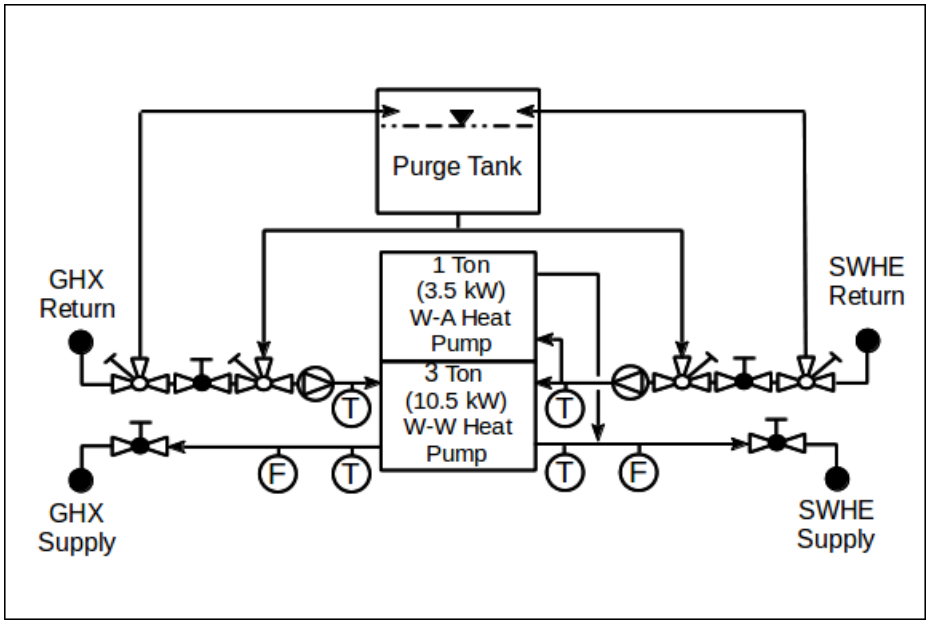

Figure 2.11: Schematic of heat extraction equipment in trailer

As stated earlier, due to weather limitations, heat extraction tests were run at two separate locations, the test pond and the indoor laboratory facility. Because we were extracting heat from the SWHE, we expected ice to form on the coil. To quantify this ice formation, a new coil testing platform was constructed. The intent of this platform was to quantify the amount of ice formed on the SWHE by using load cells to directly measure the coil buoyancy and thus infer the amount of ice formed.

In order to counteract the upward buoyancy force of the ice, a weighted frame was constructed which would be sufficiently heavy so that it would counteract the buoyancy of the ice. This frame was also used to facilitate positioning of the coil in the water by allowing us to remove the coil from the pond with minimal effort. The weighted support frame's outside dimensions were 9.5 ft. x 9.5 ft. (2.9 x 2.9 m) and weighed approximately 400 lb (181 kg). The weighted support frame can be seen in Figure 2.12.

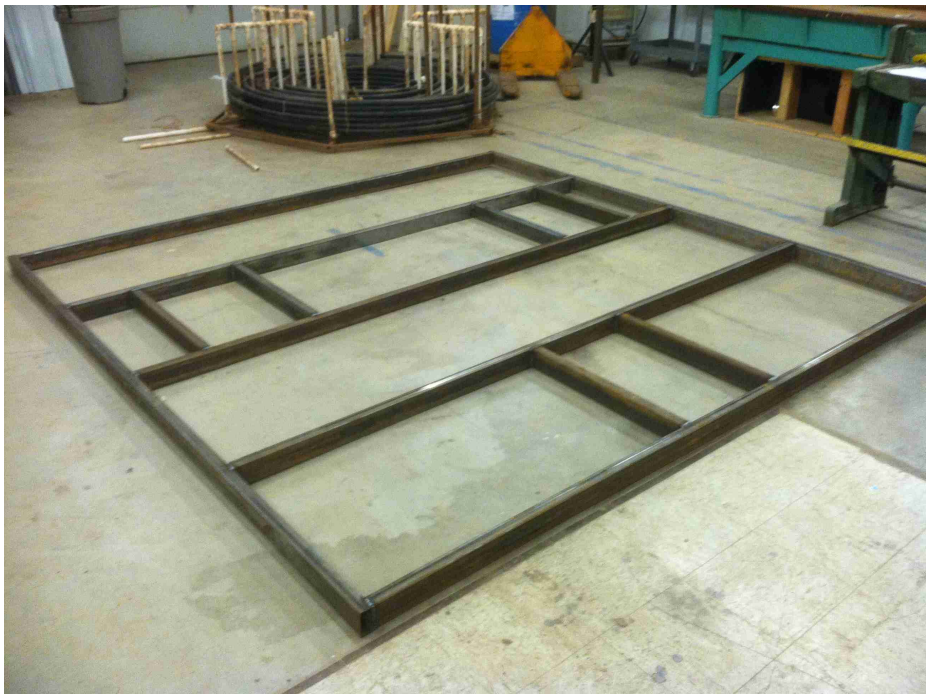

Figure 2.12: Weighted support frame

Three submersible load cells were connected between the weighted load cell frame and the SWHE support frame as can be seen in Figure 2.13. Each load cell was capable of measuring 500 lb (227 kg) in tension or compression. They were then connected together in parallel through as signal conditioning unit that would aggregate the total signal from the three load cells into one analog output signal which could be read by the data logger.

Figure 2.13: Submersible load cell used to measure buoyancy force

To support the weighted load cell frame, a support platform was constructed off site in segments and then brought to the test pond and assembled. The support platform can be seen in Figure 2.14. The platform's intended purpose was to support the load cell frame from the water surface. It would allow for the load cell frame to be positioned in the pond, and then the SWHE lowered via four 500 lb (227 kg) capacity winches to the intended depth. The support platform's inside opening dimensions were 10 ft. x 10 ft. (3 x 3 m); outside dimensions were 14 ft. x 14 ft. (4.3 x 4.3 m). The platform was supported by 10, 2 ft. (61 cm) wide by 4 ft. (122 cm) long by 1 ft. (30.5 cm) deep HDPE coated Styrofoam dock floats. The 10 dock floats had a combined buoyancy capacity of approximately 2000 lb (907 kg) floating 6 in. (15 cm) above the water. The final testing platform can be see in Figure 2.15. A schematic representation of the support platform can be seen in Figure 2.16.

While performing experiments in the pond with this apparatus, the thermistors measuring pond temperature were placed on the cables supporting the load cell frame.

They were placed at a distance of approximately 4 ft. (1.2 m) away from the SWHE. Surface water temperature was determined as shown in Equation 2.1.

(a) First segment of ice-on-coil platform.

(b) Second segment of ice-on-coil platform.

(c) Third segment of ice-on-coil platform.

(d) Final ice-on-coil platform.

Figure 2.14: Construction of ice-on-coil platform

Figure 2.15: Heat extraction experiment support platform and load cell frame

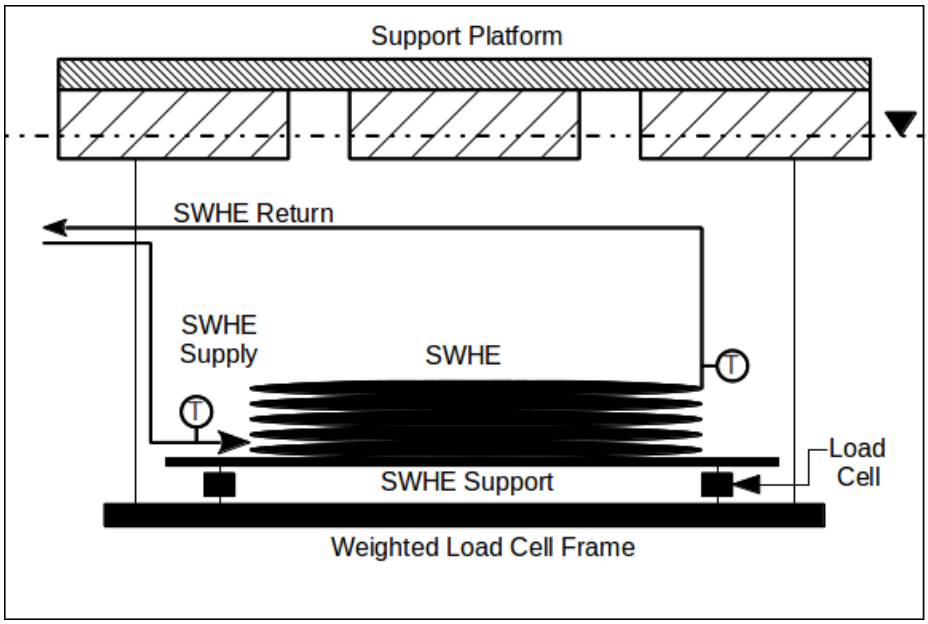

Figure 2.16: Schematic of heat extraction equipment in pond

Because heat was being extracted from the SWHE via the reversible heat pumps, the heat extracted by the 3 ton (10.6 kW) water-water heat pump was dissipated

via another SWHE in a configuration identical to the one shown in Figure 2.4. This additional SWHE was submerged in the test pond at a distance of roughly 100 ft away from the SWHE being tested. The additional SWHE was connected to the water-water heat pump via the ports labeled GHX in Figure 2.11.

As the weather and the test pond warmed, it became impossible with the current experiment to extract sufficient heat so as to cause ice to form on the SWHE. To allow continued heat extraction testing with the possibility of SWHE ice formation, the experiment was then moved to the indoor test facility.

To run tests indoors, a 4 ft. (1.2 m) deep by 15 ft. (4.6 m) diameter above ground pool was purchased and setup in the laboratory facility. The pool can be seen in Figure 2.17. The pool was constructed on top of 1/2 in. (12.7 mm) of extruded polystyrene foam (i.e. blue board) which has an R-Value of approximately 2.5 hr-ft^2-°F/BTU (0.44 m^2-°C/W). This was placed under the pool to reduce the amount of heat gain/loss to the pool while running experiments. The perimeter of the pool was also insulated with R-13 (2.3 m^2-°C/W)fiber-glass batt insulation. The pool can be seen half insulated in Figure 2.18. Heat extracted from the pool via the SWHE was then rejected via the heat pumps to the lab space for the water-air heat pump, and to two vertical borehole ground heat exchangers whose connections were inside the lab space for the water-water heat pump. The connections to these ground heat exchangers can be seen in Figure 2.19.

Figure 2.17: Pool used for testing spiral-helical SWHE in laboratory facility

Figure 2.18: Experimental setup used for indoor heat exchanger tests

Figure 2.19: Ground heat exchanger connections where the water-water heat pump rejected/extracted excess heat energy

Once the heat extraction experiment had been moved indoors, it was discovered that the submersible load cells had been damaged during the transport of the load cell frame from the pond to the laboratory facility. Due to this, new tension only load cells were purchased. These load cells have a capacity of 500 lb (227 kg) and can be seen in Figure 2.20. These load cells were less expensive than the original submersible load cells and ultimately would have been a better choice, due to the fragility of the submersible load cells. The SWHE and weighted SWHE support were then suspended from a support frame spanning the width of the pool. This support frame can be seen in Figure 2.21. The tension only load cells were then used to measure the weight of the SWHE, along with the support frame, during the experiments. From this, the ice mass can be calculated. A schematic of the indoor pool, load cell frame, and support structure can be seen in Figure 2.22.

Pool water temperature measurements were taken in the pool at a distance of 4

ft. (1.2 m) away from the SWHE. Pool temperature was determined by averaging the temperature across the SWHE, as is shown in Equation 2.1.

Figure 2.20: Tension only load cell

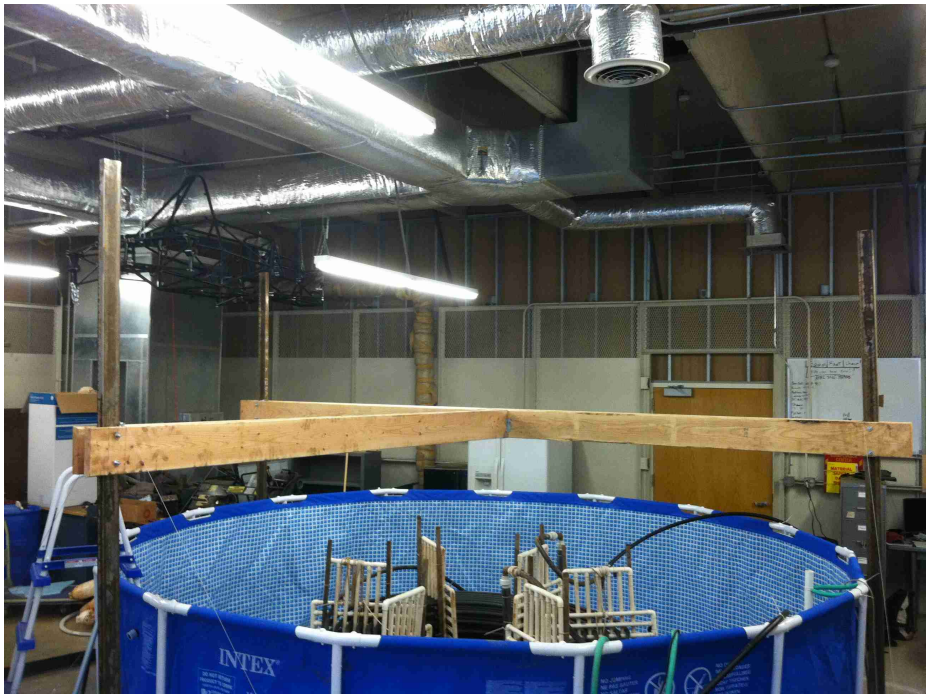

Figure 2.21: Support frame used to support the weighted load cell frame

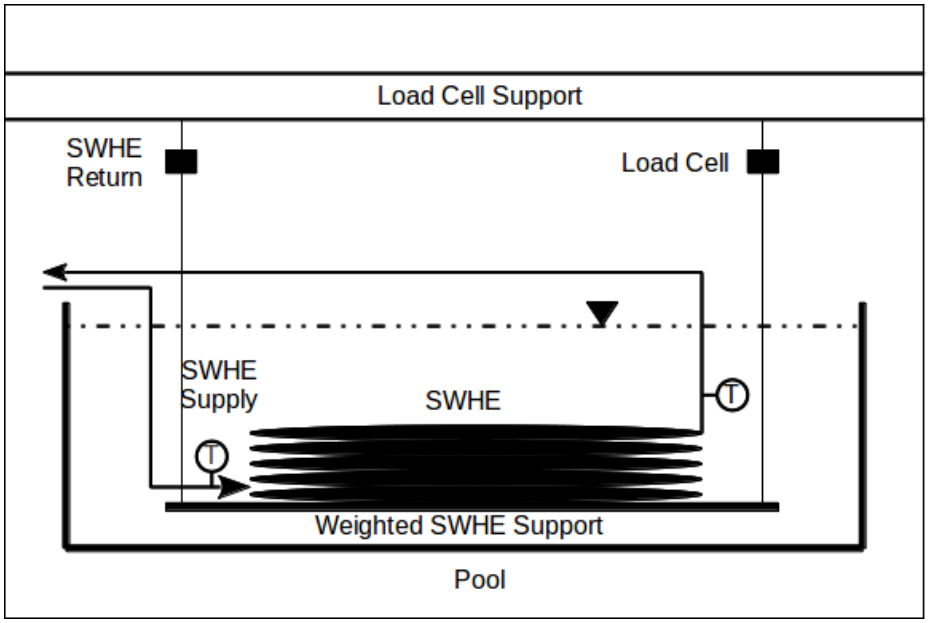

Figure 2.22: Schematic of heat extraction equipment in pool

2.2.3 Methodology

Because the heat pumps we used for heat extraction were not variable speed machines, we were not able to vary heat transfer rates as was the case for the heat rejection tests. For these tests, the heat pumps were turned on and run for extended periods of time.

As was the case with heat the rejection tests, coil entering and exiting fluid temperatures were measured as was circulating fluid flow rate through a calibrated turbine flow meter. The heat pump entering and exiting fluid temperatures were also measured; however, the temperatures were not directly used to determine heat exchanger performance.

Total coil frame weight was also measured, which is the combined weight of the coil support frame and the coil. From this, the buoyancy force generated from the ice formation could then be estimated by subtracting the current weight from the weight at the beginning of the test.

2.3 Instrumentation

2.3.1 Temperature Measurement

Two types of temperature sensors were used to measure temperature. The first temperature sensor was an in-pipe thermistor which was used to measure the circulating fluid temperature at the SWHE inlet and outlet. A photo of the in-pipe thermistor can be seen in Figure 2.23. The thermistors were purchased from Omega Engineering and have a model number of: ON-410-PP.

Figure 2.23: In-pipe thermistor used to measure circulating fluid inlet and outlet temperature

The second type of temperature sensor is a thermistor which which was soldered to 22 ga. (0.644 mm) instrumentation wire. These thermistors were used to measure the surface water temperatures in the pond and pool during experiments. A photo of one of these thermistors can be seen in Figure 2.24. The thermistors were purchased from Jameco Electronics and have a model number of: 207037.

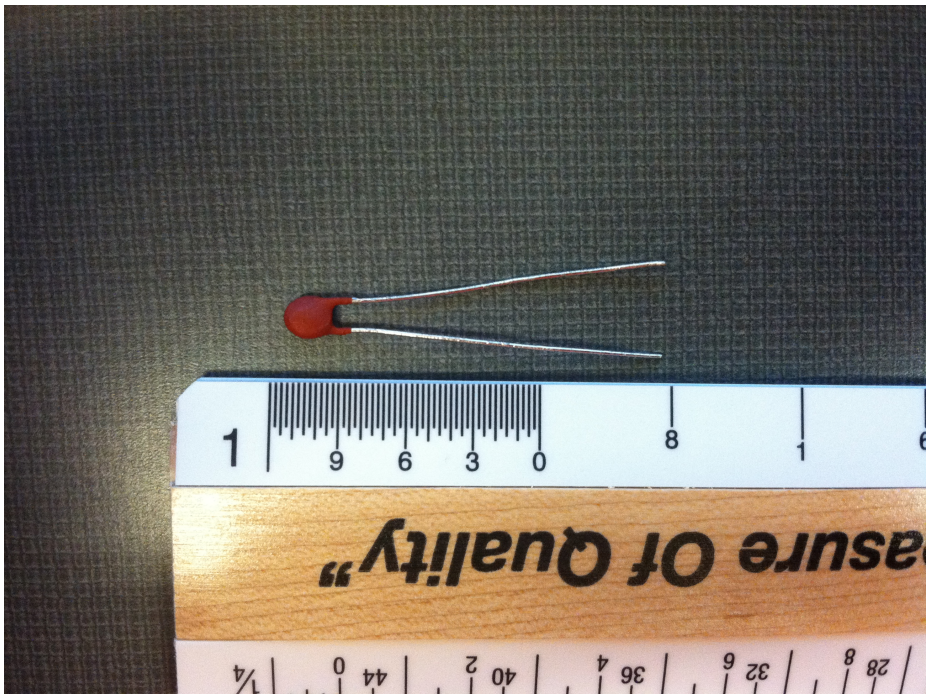

Figure 2.24: Thermistor for surface water temperature measurement

After the smaller thermistor was soldered to the 22 ga. (0.644 mm) instrumentation wire, it was coated in marine epoxy up to the tip to prevent the lead wires from touching. This epoxy also seals the soldered connections preventing surface water from causing a short in the electrical circuit. A photo of an epoxied themistor can be see in Figure 2.25.

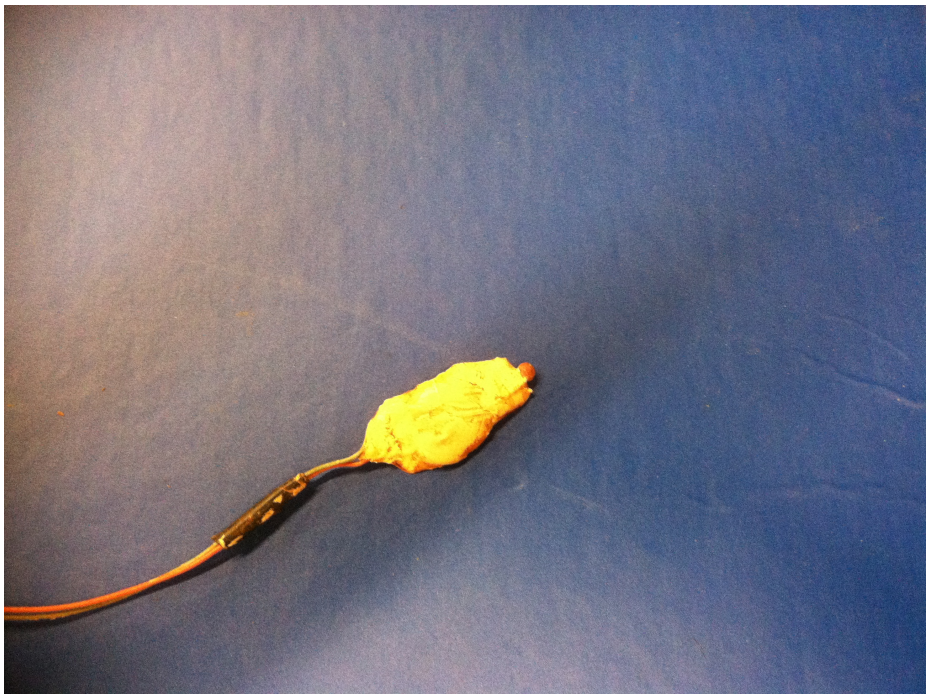

Figure 2.25: Themistor coated in epoxy up to the tip for surface water temperature measurement

2.3.2 Temperature Measurement Calibration

The thermistors shown in Figure 2.23 were also soldered to 22 ga. (0.644 mm) instrumentation wire. This was done so instrumentation wires could be run from the SHWE, which was submerged in the pond, to the data logger which was situated in the trailer several hundred feet away. Because of the instrumentation wire being added to the circuit, as well as the inherent uncertainty in the thermistor resistance, the thermistors needed to be calibrated with the leads attached so the temperatures could be accurately determined. Because thermistor resistance varies with temperature, the resistance was what was necessary to record in order to determine the temperature measurement.

To perform the calibration, the thermistors were placed in a calibration water bath, as is shown in Figure 2.26. This water bath was set at a given set point,

then allowed to run to a steady state temperature. Once the bath temperature was constant, the resistance was measured every 5 seconds for 5 minutes. The average value of these measurements was then taken as the thermistor resistance at that given temperature. Bath temperature was determined from a glass spirit filled thermometer which was calibrated to 0.09°F (0.05°C). This thermometer is also visible in Figure 2.26. The thermometer was manufactured by ERTCO.

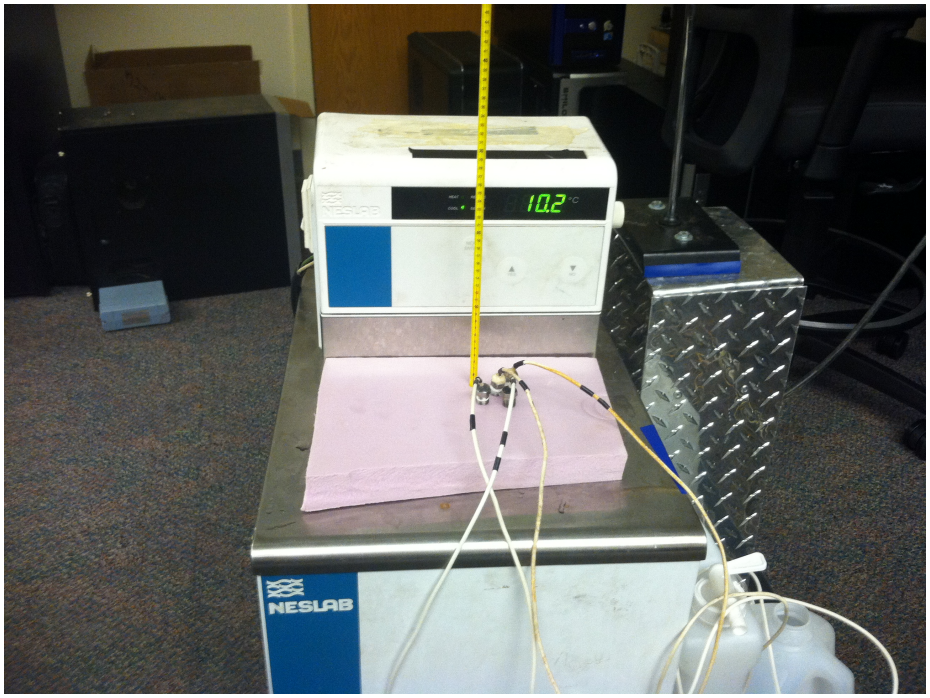

Figure 2.26: Calibration bath used to calibrate thermistors

To record the resistance readings, a Fluke Hydra Series II data logger was used to measure the resistance of the thermistor. The data logger's operation manual states that its resistance measurment accuracy is within 0.0125%. Data logger accuracy when sampling analog signals in the 0-30 VDC range is 0.041%.

Figure 2.27: Fluke data logger used to measure and record flow and temperature measurements

As an example calibration, the values in Table 2.7 were taken from a calibration performed on one of the thermistors used in the experiment. From this data, Equation 2.2 (Steinhart & Hart 1968) was used to correlate the data.

$$\frac{1}{T_{abs}} = A + B \cdot ln(\Omega) + C \cdot ln(\Omega)^2 + D \cdot ln(\Omega)^3 \tag{2.2}$$

Once the data had been correlated, the measured and correlated temperatures were compared to determine the accuracy of the temperature correlation. The correlation coefficients for the data set shown in Table 2.7 can be seen in Table 2.8.

From Table 2.9, we can see that calibration yielded a good fit to the measured resistance and temperature data. The largest absolute error for this data set is 0.11°F (0.06°C) which occurred at a temperature measurement near 86°F (30°C). The rest of the measured values for this particular data set are shown to have absolute temperature errors of around half of the absolute error that occurred at 86°F (30°C).

Table 2.7: Reference temperature and resistance data from thermistor calibration

Ref. Temp.	Resistance
°F (°C)	Ohms Ω
40.82 (4.90)	5590.54
49.91 (9.95)	4410.50
59.00 (15.00)	3492.99
68.00 (20.00)	2788.47
76.91 (24.95)	2245.31
85.91 (29.95)	1815.22
94.91 (34.95)	1484.24
104.00 (40.00)	1213.29
113.09 (45.05)	998.45
122.09 (50.05)	825.90

Table 2.8: Correlation coefficients for data in Table 2.7

A	B	C	D
$1.22030 \cdot 10^{-3}$	$3.25326 \cdot 10^{-4}$	$-1.08026 \cdot 10^{-5}$	$5.80588 \cdot 10^{-7}$

This result from the previous thermistor cailbration example is typical for all thermistors calibrated. To be conservative, and to simplify the temperature uncertainty analysis, the measured temperature uncertainty for all thermistors was taken to be 0.18°F (0.1°C). This simplifies the book keeping for the uncertainty analysis and applies a conservative estimate to the error that can be expected from the temperature measurements.

2.3.3 Flow Measurement

Two separate flow meters were used to measure the circulating fluid flow rate. The first flow meter was manufactured by Omega Engineering with a model number of FTB4605. This flow meter has capability to measure flow from 0.5-20 gpm (1.9-75.7 L/min) with a stated accuracy of ±1.5%. The flow meter is a pulse output flow meter, and therefore it requires a signal conditioner to convert the pulse output to an analog

Table 2.9: Measured and correlated temperature for a thermistor calibration

T_{meas}	T_{corr}	$\lvert T_{meas} - T_{corr} \rvert$
°F (°C)	°F (°C)	°F (°C)
40.82 (4.90)	40.86 (4.92)	0.04 (0.02)
49.91 (9.95)	49.86 (9.92)	0.05 (0.03)
59.00 (15.00)	58.95 (14.97)	0.05 (0.03)
68.00 (20.00)	68.00 (20.00)	0.00 (0.00)
76.91 (24.95)	76.96 (24.98)	0.05 (0.03)
85.91 (29.95)	86.02 (30.01)	0.11 (0.06)
94.91 (34.95)	94.87 (34.92)	0.04 (0.03)
104.00 (40.00)	103.95 (39.97)	0.05 (0.03)
113.09 (45.05)	113.02 (45.01)	0.07 (0.04)
122.09 (50.05)	122.14 (50.08)	0.05 (0.03)

signal for the data logger to record. The signal conditioner was also purchased from Omega Engineering with a model number of DFP701. The Omega flow meter was used for all pond heat rejection tests.

The second flow meter was purchased from Gem Sensors. Its model number is 230216 and is stated by the manufacture to have an accuracy of $\pm$ 7%. The flow meter has a flow range from 0.5-12 gpm (1.9-45.4 L/min) and outputs an analog signal. A photo of this flow meter during a heat extraction test can be seen in Figure 2.28.

Figure 2.28: Gem flow meter during heat extraction test

2.3.4 Flow Measurement Calibration

To calibrate the flow meters, three 5 gal. (18.9 L) buckets, a stopwatch, and scale calibrated to 0.11 lb (0.05 kg) were used. To determine the flow rate, the flow through the flow meter was set to run at steady state conditions. Fluid was then sampled from the flow stream using the buckets and the total time the fluid was sampled was recorded. The mass of the fluid was determined by subtracting the initial weight of each bucket, and the total fluid mass for a specific flow rate was then determined. Once the fluid was sample from the flow stream, it was returned to the purge tank feeding the pump and flow meter.

This information was then used to calculate the volumetric flow rate for that particular fluid flow set point. The data logger was also used to record the analog signal at 5 sec. intervals. The average analog voltage during the flow measurement was then taken as the flow meter output for that set point. Because the fluid is

essentially flowing in a closed loop and no heat is being added, the fluid temperature was sampled once during the calibration process. This temperature was necessary to determine the density of the circulating fluid.

Table 2.10 shows data taken from a calibration of the Gem flow meter. The maximum absolute percent error for the Gem flow meter is 1.46% with an error standard deviation of 0.084 gpm (0.32 L/min). The Omega flow meter was calibrated in the same manner and shows a maximum absolute percent error of 0.6% with an error standard deviation of 0.015 gpm (0.06 L/min). Because two times the standard deviation represents the 95% confidence interval, two times the standard deviation is what flow measurement uncertainty was taken as.

Table 2.10: Measured and correlated flow rates for Gem flow meter

FM Output	$\dot{V}_{meas}$	$\dot{V}_{corr}$	$\lvert\dot{V}_{meas} - \dot{V}_{corr}\rvert$	% Error
VDC	gpm (L/min)	gpm (L/min)	gpm (L/min)	
0.02	0.000 (0.0)	0.091 (0.34)	0.091 (0.34)	-
2.91	5.903 (22.35)	5.935 (22.47)	0.032 (0.12)	0.55
2.93	6.049 (22.90)	5.965 (22.58)	0.085 (0.32)	-1.40
3.50	7.227 (27.36)	7.125 (26.97)	0.102 (0.39)	-1.41
3.53	7.221 (27.33)	7.188 (27.21)	0.033 (0.12)	-0.45
4.33	8.852 (33.51)	8.799 (33.31)	0.053 (0.20)	-0.59
4.33	8.831 (33.43)	8.801 (33.32)	0.030 (0.11)	-0.34
5.31	10.77 (40.77)	10.79 (40.84)	0.021 (0.08)	0.19
5.38	10.77 (40.77)	10.93 (41.37)	0.157 (0.59)	1.46

2.3.5 Other Instrumentation

Instrumentation used in these experiments apart from the temperature sensors, flow meters, and data loggers, are the load cells which were purchased through Interface Inc. The first set of load cells were submersible and had a total capacity of 500 lb (2,224 N) in tension or compression. The submersible load cells had a model number of 2420BTH-500. A photo of one of these load cells can be seen in Figure 2.13.

The second set of load cells were also purchased from Interface. These load cells were tension only load cells with a tensile capacity of 500 lb (2,224 N). A photo of one of these load cells can be seen in Figure 2.20.

All load cell outputs were processed through a signal conditioning unit (model SGA). This signal conditioner aggregated the output signals from the three load cells and amplified the output to an 0-10 VDC analog signal. Load cells came pre-calibrated from Interface.

CHAPTER 3

EXPERIMENTAL RESULTS AND UNCERTAINTY

3.1 Data Analysis

The heat rejection and heat extraction data were analyzed by treating the water on the outside of the heat exchanger as having an infinite capacity. Then, the ε–NTU method was used to determine the heat exchanger's overall heat transfer coefficient. From this, the outside convection heat transfer coefficient could then be backed out given that the values for the remaining thermal resistance components can be accurately estimated or otherwise determined.

SWHE heat transfer rate was calculated by Equation 3.1 from the circulating fluid mass flow rate along with entering and exiting fluid temperatures. The maximum possible heat transfer rate is given by Equation 3.2. Surface water temperature is measured as described in Sections 2.1.2 and 2.2.2; the value was calculated as a weighted average of the three measurements as given in Equation 2.1. Circulating fluid mass flow rate is calculated from Equation 3.3 from the volumetric flow rate measured by the flow meter and the circulating fluid density.

$$\dot{Q}_{SWHE} = \dot{m}_f \, c_{p,f} \, (T_{f,in} - T_{f,out}) \tag{3.1}$$

$$\dot{Q}_{max} = \dot{m}_f \, c_{p,f} \, (T_{f,in} - T_{sw}) \tag{3.2}$$

$$\dot{m} = \dot{V} \cdot \rho_f \tag{3.3}$$

Heat exchanger effectiveness is calculated with Equation 3.4. Then, the heat exchanger overall heat transfer coefficient UA_s is determined with Equations 3.5 and 3.6. Equation 3.5 is used in heat exchanger analysis for situations when one side of the heat exchanger is considered to have an infinite capacity. For our case, the surface water temperature is not expected to change temperature due to the heat rejected or extracted by the SWHE. This is because we expect the mass, and thus, thermal capacitance of the surface water to be very large when compared to the heating or cooling load. Because we don't expect the surface water temperature to be notably affected by the SWHE, Equation 3.5 is valid.

$$\varepsilon = \frac{\dot{Q}_{SWHE}}{\dot{Q}_{max}} \tag{3.4}$$

$$\text{NTU} = -\ln(1-\varepsilon) \tag{3.5}$$

$$UA_s = \text{NTU}\,\dot{m}_f\,c_{p,f} \tag{3.6}$$

From the heat exchanger overall heat transfer coefficient, the total thermal resistance of the heat exchanger can be determined by Equation 3.7. At this point, the outside convective resistance can be determined, given that the inside convective resistance and pipe wall conductive resistance values can be calculated independently.

$$(UA_s)^{-1} = R_{tot} = R_{conv,i} + R_{cond} + R_{conv,o} \tag{3.7}$$

To calculate the inside thermal resistance, the inside Nusselt number as correlation developed by Rogers & Mayhew (1964) is used. This correlation for Nusselt number (Equation 3.8) given by Rogers & Mayhew (1964) is a heat transfer correlation for helically coiled tubes under isothermal exterior tube surface conditions. Included in the correlation is the ratio of pipe inside diameter to coil diameter which helps quantify

the increase in heat transfer due to the secondary flows that occur in helically coiled pipes. Rogers & Mayhew (1964), Seban & McLaughlin (1963), as well as others, have noted that secondary flows induced in helical pipes due to the centrifugal forces associated with the flow and curvature cause increases in heat transfer rate. Because of these secondary flows, a straight pipe approximation is insufficient and the Rogers & Mayhew (1964) correlation was selected as the best approximation for inside Nusselt number. The mean coil diameter is calculated by averaging the SWHE inside and outside diameters as is indicated in Equation 3.9. Coil inside and outside diameters can been seen in Figure 1.5.

$$\mathrm{Nu}_{D,i} = 0.023\, Re_{D_{i,p}}^{0.85}\, Pr^{0.4} \left(\frac{D_{i,p}}{D_{ave,SWHE}}\right)^{0.1} \tag{3.8}$$

$$D_{ave,SWHE} = \frac{D_{i,SWHE} + D_{o,SWHE}}{2} \tag{3.9}$$

Coil inside convection coefficient and inside convective thermal resistance are calculated directly from Equations 3.10 and 3.11.

$$h_{conv,i} = \frac{Nu_{D,i}\, k_f}{D_{p,i}} \tag{3.10}$$

$$R_{conv,i} = (h_{conv,i}\, A_{s,p,i})^{-1} \tag{3.11}$$

Properties for the circulating fluid are evaluated at the mean fluid temperature by using Equation 3.12. This equation was derived from Equation 3.13 which uses the ε–NTU method to define the mean fluid temperature as a function of distance along the tube (x) (Equation 3.14).

$$T_{MFT} = T_{sw} + \frac{\dot{m}\, c_{p,f}}{UA_s} \cdot \left[T_{f,in} \left(1 - exp \left[\frac{-UA_s}{\dot{m}\, c_{p,f}} \right] \right) + T_{sw} \left(-1 + \exp \left[\frac{-UA_s}{\dot{m}\, c_{p,f}} \right] \right) \right] \quad (3.12)$$

$$\dot{m}\, c_{p,f} (T_{f,in} - T(x)) = \varepsilon(x)\, \dot{m}\, c_{p,f}\, (T_{f,in} - T_{sw}) \quad (3.13)$$

$$\varepsilon(x) = 1 - exp \left[\frac{-UA_s\, x}{\dot{m}\, c_{p,f}\, L} \right] \quad (3.14)$$

Solving Equation 3.13 for $T(x)$ and applying the average value theorum of calculus by integrating from 0 to L and dividing the integrated result by L gives us Equation 3.12 which is the mean circulating fluid temperature. This approach assumes that the heat exchanger UA_s value is a linear function of tube length only.

Equation 3.15 is used to define the pipe wall thermal resistance (Cengel & Ghajar 2011). HDPE thermal conductivity is calculated from Equation 3.16 which defines the thermal conductivity of the HDPE tube as a function of mean SWHE pipe temperature and HDPE density (Rauwendaal 1986).

$$R_{p,cond} = \frac{ln \left(\frac{D_{p,o}}{D_{p,i}} \right)}{2\, \pi\, k_p\, L_p} \quad (3.15)$$

$$k_p = 0.17 + 5\, (\rho_p - 0.9) - 0.001\, T_{p,ave} \quad (3.16)$$

Equation 3.16 has units of W/mK with the mean pipe temperature in units of °C and units for HDPE density of gr/cc. HDPE density was taken as 0.955 gr/cc (Polypipe 2013). No work has been performed to date to correlate the thermal conductivity of thermally enhanced HDPE for different temperatures. Due to this, a constant value of 0.4 BTU/hr-ft-°F (0.7 W/mK (Gonthier 2012)) was used as the value for thermal conductivity of thermally enhanced HDPE.

Mean SWHE pipe temperature is taken as the average of the inside and outside SWHE pipe temperature (Equation 3.17). Inside and outside pipe surface temperatures are defined in Equations 3.18 and 3.19.

$$T_{p,ave} = \frac{T_{s,p,i} + T_{s,p,o}}{2} \tag{3.17}$$

$$T_{s,p,i} = T_{MFT} - R_{conv,i} \cdot \dot{Q}_{SWHE} \tag{3.18}$$

$$T_{s,p,o} = T_{s,p,i} - R_{cond} \cdot \dot{Q}_{SWHE} \tag{3.19}$$

Now that the inside convective resistance and pipe wall conductive resistances are known, the outside convective resistance, outside convection coefficient, and outside Nusselt number can be calculated directly from Equations 3.20, 3.21, and 3.22.

$$R_{conv,o} = R_{tot} - R_{conv,i} - R_{cond} \tag{3.20}$$

$$h_{conv,o} = (R_{conv,o}\, A_{s,p,o})^{-1} \tag{3.21}$$

$$\mathrm{Nu}_{D,o} = \frac{h_{conv,o}\, D_{p,o}}{k_w} \tag{3.22}$$

By implementing this methodology, the experimental data can be analyzed and outside Nusselt number determined. This will allow the data to be correlated against the modified Rayleigh number (Churchill & Chu 1975) which is given in Equation 3.23.

$$\mathrm{Ra}^{*}_{D,o} = \frac{g\, \beta_w\, \dot{q}\, D^4_{p,o}}{k_p\, \nu_w\, \alpha_w} \tag{3.23}$$

Properties for the outside Nusselt and modified Rayleigh numbers are evaluated at the outside film temperature (Equation 3.24) which is taken as the average between

the SWHE pipe outside surface temperature and the far field pond temperature at the SWHE submersion depth.

$$T_{film,o} = \frac{T_{s,p,o} + T_{sw}}{2} \tag{3.24}$$

The implementation of this method requires an iterative solution due to the fact that initial assumptions necessarily must be made in order to perform the calculations. The iterative process is run until the system of equations converges using 5.5E-4°F (0.001°C) as the convergence criteria for mean fluid temperature. Convergence is reached typically after 4-5 iterations.

3.2 Heat Rejection Results

3.2.1 Hansen's Pond Data Set

As stated in Chapters 1 and 2, and indicated in Tables 2.1, 2.2, and 2.3, this work is a continuation of work initiated by Hansen (2011). The data collected by Hansen (2011) can be see in Figure 3.1 where the experimental Nusselt number is plotted against modified Rayleigh number.

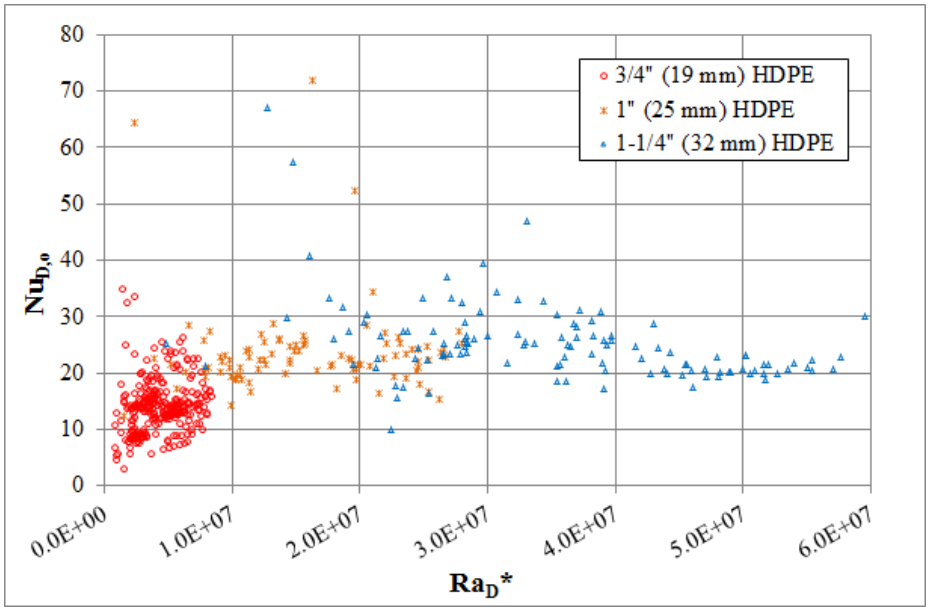

Figure 3.1: Nusselt vs. modified Rayleigh number plot of heat rejection data collected by Hansen (2011)

In total, 528 data points were collected on 19 spiral-helical SWHE coil configurations by Hansen (2011). Data collection began on March 2, 2011 and continued through September 2011.

3.2.2 Updated Pond Data Set

After the completion of the work performed by Hansen (2011), an additional 191 data points were collected on eight additional spiral-helical SWHE coil configurations. These additional results, along with the results collected by Hansen (2011) can be seen in Figure 3.2. These additional tests were collected at the test pond from October 6 through December 2, 2011.

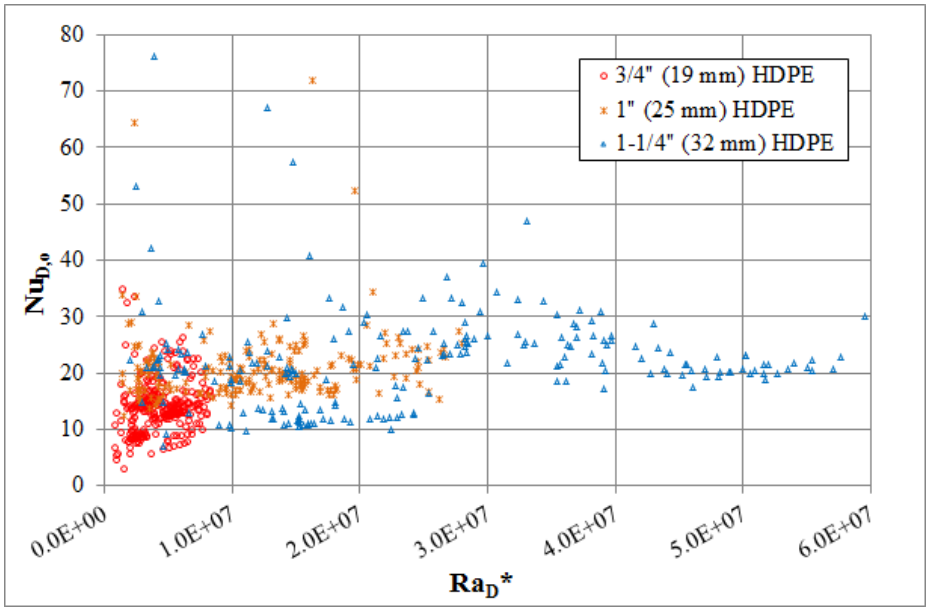

Figure 3.2: Nusselt vs. modified Rayleigh number plot of all heat rejection data collected in the test pond

Another summary of the expeimental data can be seen in Table 3.1 where the average percentage of total thermal resistance for each thermal resistance component is show. Here, we can see that the outside convection resistance makes up on average around 28% of the total SWHE thermal resistance. The relatively much larger thermal resistance percentage of the SWHE pipe appears to be the area where a small improvement in pipe thermal performance would make the greatest impact.

Table 3.1: Average thermal resistance for each thermal resistance component as a percentage of total thermal resistance for pond heat rejection data

Tube Size	Material	$R_{conv,i}$	R_{cond}	$R_{conv,o}$	# Points
3/4 in. (19 mm)	PE 3408	3.3%	63.4%	33.3%	288
1 in. (25 mm)	PE 3408	2.3%	73.3%	24.4%	199
1-1/4 in. (32 mm)	PE 3408	2.5%	71.9%	25.6%	200

3.2.3 Pool Data

As described in Section 2.2, once the weather would not permit heat extraction testing in the test pond, the experiment was moved indoors to the laboratory facility. While there, some additional tests under heat rejection conditions were also performed.

Tests under heat rejection conditions were performed on 3/4 in. (19 mm) dia. thermally enhanced HDPE with two separate tube-tube spacings. The first was the 2.625 in. H x 2.625 in. V (67 mm x 67 mm) configuration, and the second was the 2.625 in. H x 1.3 in. V (67 mm x 33 mm) configuration. 1-1/4 in. (32 mm) dia. thermally enhanced HDPE was also tested with 4.125 in. H x 2.625 in. V (105 mm x 67 mm) tube-tube spacings. Nusselt vs. modified Rayleigh number plots for these three tests can be seen in Figures 3.3, 3.4, and 3.5.

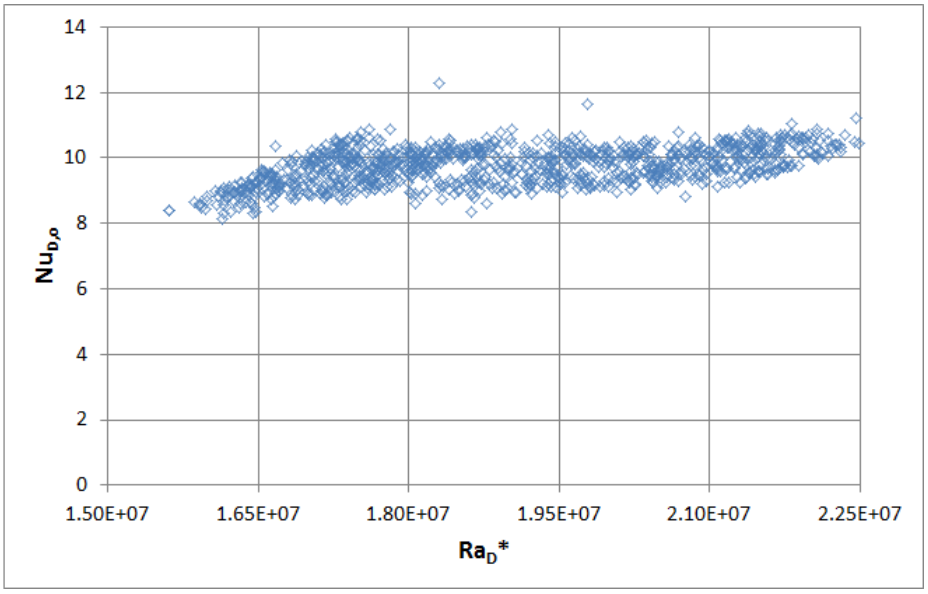

Figure 3.3: Heat rejection data taken in pool for 3/4 in. (19 mm) dia. thermally enhanced HDPE for 2.625 in. H x 1.3 in. V (67 mm x 33 mm) tube-tube spacing

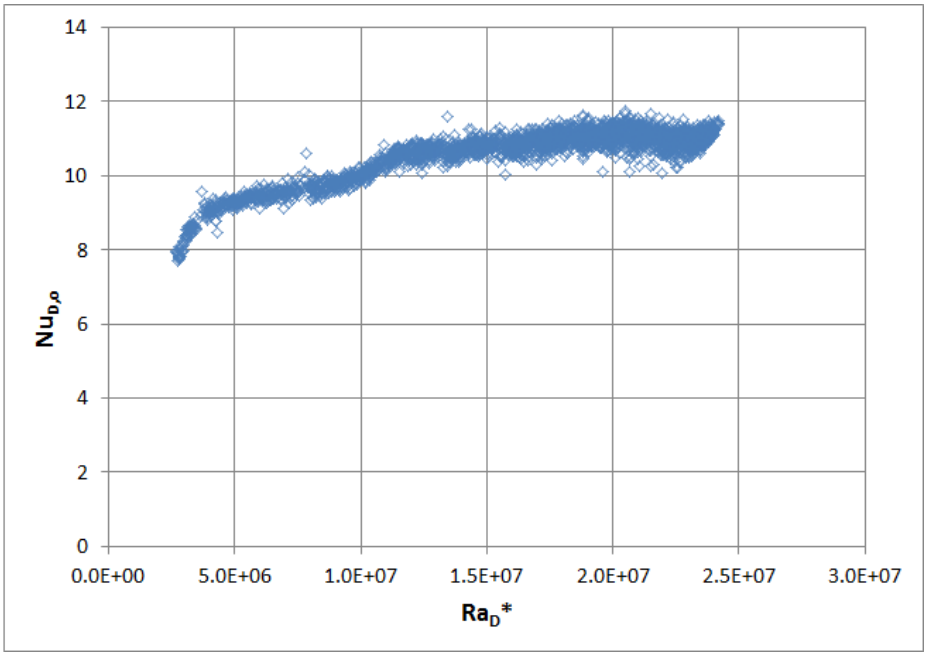

Figure 3.4: Heat rejection data taken in pool for 3/4 in. (19 mm) dia. thermally enhanced HDPE for 2.625 in. H x 2.625 in. V (67 mm x 67 mm) tube-tube spacing

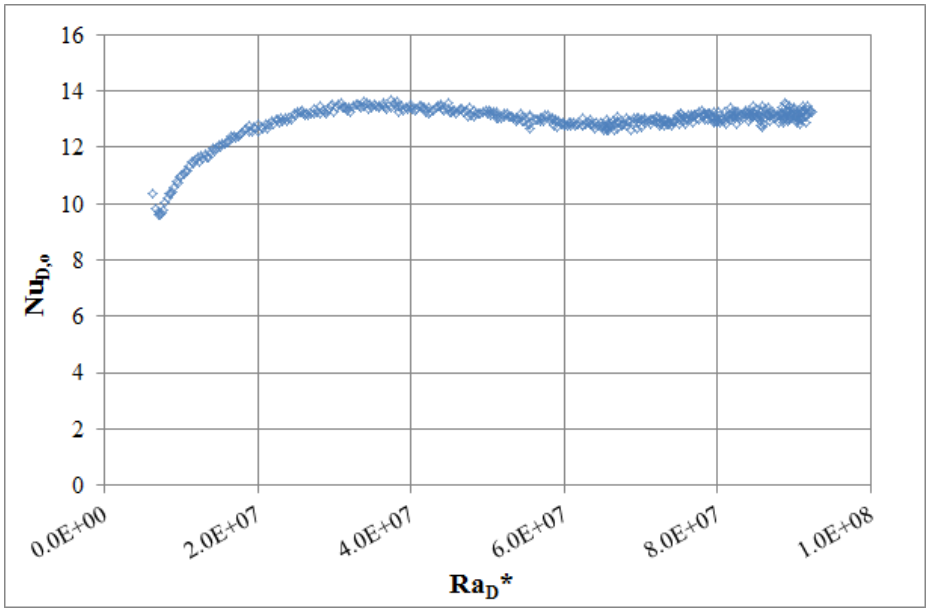

Figure 3.5: Heat rejection data taken in pool for 1-1/4 in. (32 mm) dia. thermally enhanced HDPE for 4.125 in. H x 2.625 in. V (105 mm x 67 mm) tube-tube spacing

Figure 3.5 shows the Nusselt number begin dropping after about $Ra_D^* = 3.5 \cdot 10^7$.

At about $Ra_D^* = 6.0 \cdot 10^7$ we can see separation in the Nusselt numbers. The reason for this dip is not fully understood.

Table 3.2 shows the thermal resistance components for each SWHE tube size as a percentage of total thermal resistance. Here, we see that the pipe conduction resistance tends to make up nearly half of the total thermal resistance with the outside convective resistance making up nearly the other half. This shift when compared to the data in Table 3.1 is theorized to be due to the constrained nature of the pool combined with the fact that the data was taken on thermally enhanced HDPE.

Table 3.2: Average thermal resistance for each thermal resistance component as a percentage of total thermal resistance for pool heat rejection data

Tube Size	Material	$R_{conv,i}$	R_{cond}	$R_{conv,o}$	# Points
3/4 in. (19 mm)	TEHDPE	4.1%	48.1%	47.8%	3562
1-1/4 in. (32 mm)	TEHDPE	5.4%	50.5%	44.1%	1420

3.3 Heat Extraction Results

3.3.1 Pond Data

Due to the nature of the testing apparatus, it was not possible to directly vary heat extraction rate. A series of tests were run at steady state conditions for six hours up to two days at a time. Data were collected at varying intervals of one minute up to five minutes. This can be seen below in Figure 3.6 where 24 hours of experimental run time is shown.

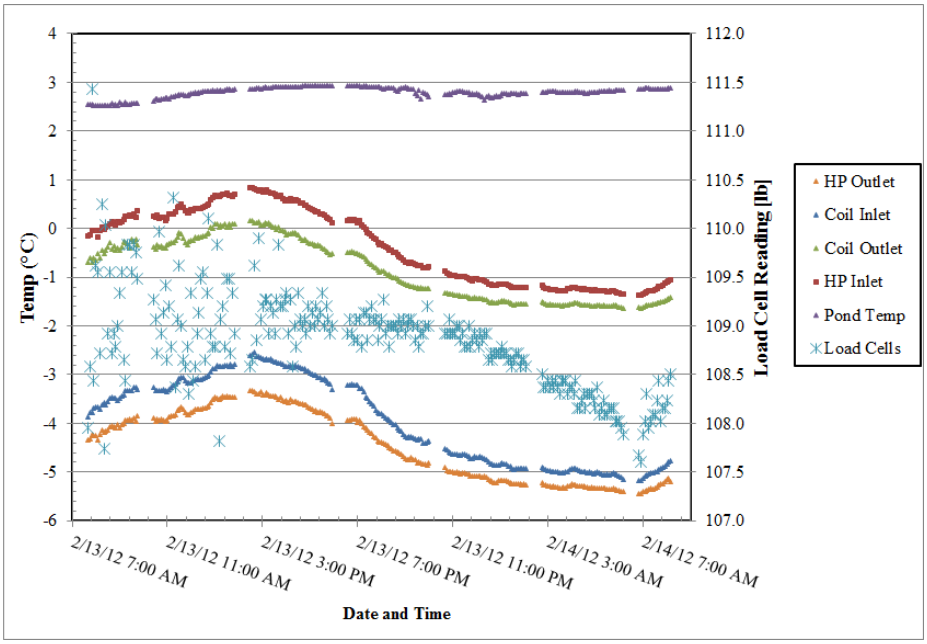

Figure 3.6: Data from heat extraction experiment during test in the test pond on February 13, 2012

Also visible in Figure 3.6 are breaks in the data where gaps can be seen. The water-water heat pump used for the heat extraction tests had a safety feature built in which caused the heat pump to shutdown after four hours of continuous run time. During this time, the heat pump performed diagnostics on itself to verify all safety switches were functioning properly. After a five minute diagnostic period, the heat pump would begin operation again. Due to the disruptions in the run time, the data for up to 40 minute after the beginning of the shut down were cut from the data set. This was done to eliminate the transient affects that were introduced into the system because of the heat pump shutdown. New microchips that control the heat pump run time were ordered, but not installed until the experiment had been moved to the indoor test facility.

The signal output directly from the load cells can also be seen in Figure 3.6. A decrease in load cell output indicates an increase in buoyancy force, potentially signifying ice formation. On this occasion, the load cells recorded approximately 1.5

lb. (6.7 N) decrease in load cell reading which may be attributed to ice formation on the coil. Consequently, this was the only recorded potential ice formation that occurred while running experiments in the pond. The summer and winter of 2011-2012 were among the warmest on record. Due to that, it is uncertain if any ice was formed on the coil while running experiments in the pond. Photos of the test data corresponding to Figure 3.6 can be seen in Figures 3.7 and 3.8.

Figure 3.7: Heat extraction platform during heat extraction test in the test pond on February 13, 2012

Figure 3.8: Heat extraction experiment during test in the test pond on February 13, 2012

All heat extraction data collected in the test pond can be seen in Figure 3.9. In order to collect the pond data, a series of tests were performed from January 19, 2012 to March 9, 2012. All data collected in the pond under heat extraction conditions was taken on thermally enhanced 3/4 in. (19 mm) dia. SDR-11 HDPE pipe. The coil length was 500 ft (152.4 m) and the tubes were arranged on horizontal and vertical tube-tube spacing of 2.625 in. H x 2.625 in. V (67 mm x 67 mm).

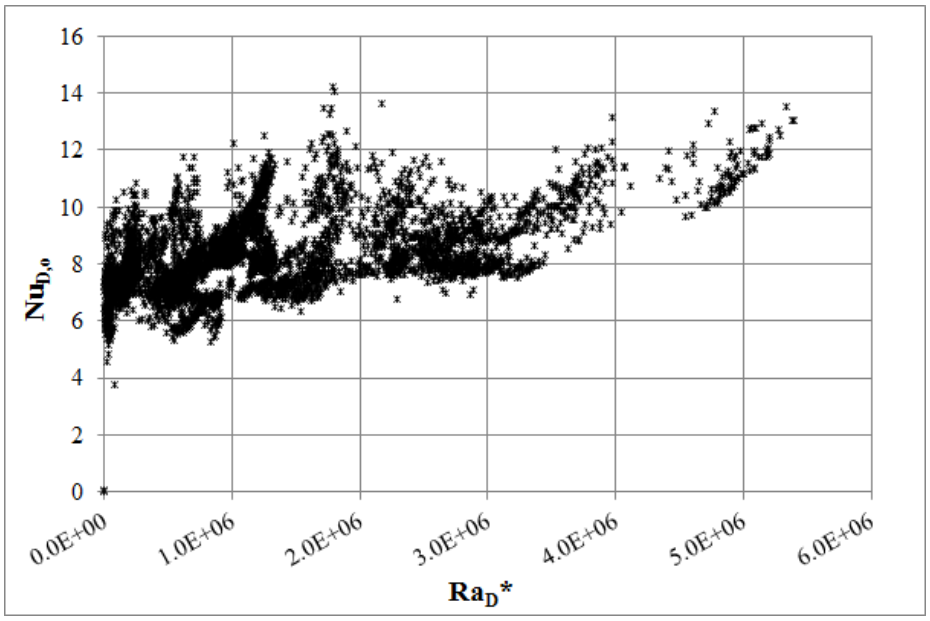

Figure 3.9: Nusselt vs. modified Rayleigh number plot of heat extraction data collected in the test pond

Table 3.3 shows the thermal resistance of each resistance component as a percentage of the total thermal resistance. Because the pond heat extraction data was taken on thermally enhanced pipe, the pipe conduction resistance represents a smaller portion of the total thermal resistance. When comparing with the same data for the 3/4 in. (19 mm) pipe in Table 3.1, the more conductive pipe causes the outside convective resistance to go from 33% up to 54%.

Table 3.3: Average thermal resistance for each thermal resistance component as a percentage of total thermal resistance for pond heat extraction data

Tube Size	Material	$R_{conv,i}$	R_{cond}	$R_{conv,o}$	# Points
3/4 in. (19 mm)	TEHDPE	6.1%	39.5%	54.4%	5350

3.3.2 Pool Data

Once the experiment was moved indoors, heat extraction data was collected in the pool. Figures 3.10, 3.11, and 3.12 show the heat extraction test data for three different

coil configurations. All tests were run on thermally enhanced HDPE pipe with a coil length of 500 ft (152.4 m). Periods where coil icing occurred were filtered from the data sets for external convection calculation purposes. Points labeled a), b), c) and d) in Figure 3.10 will be described in the subsequent paragraphs and illustrated with Figure 3.13.

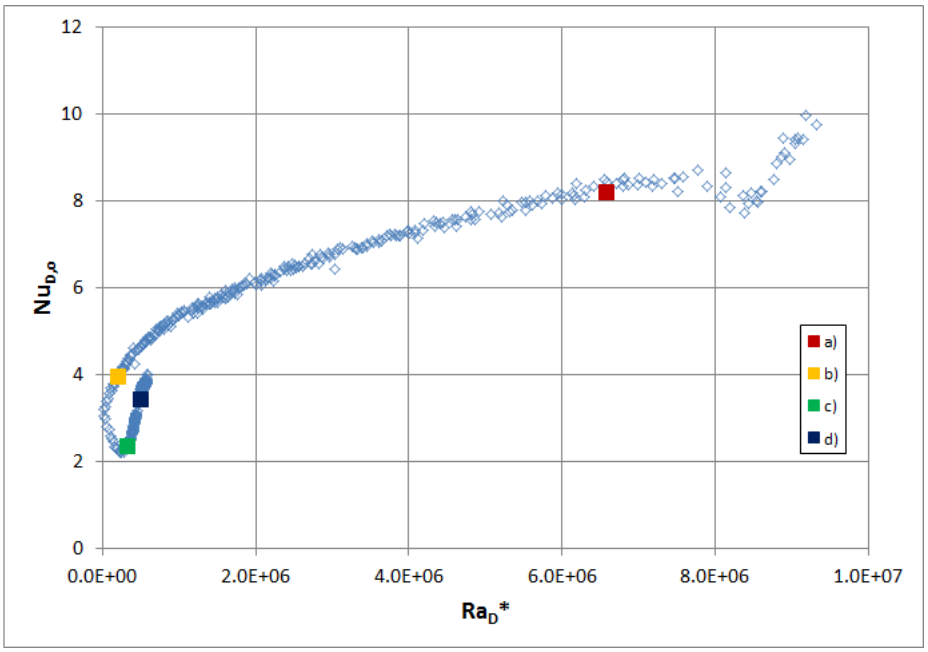

Figure 3.10: Heat extraction data taken in pool for 3/4 in. (19 mm) dia. thermally enhanced HDPE for 2.625 in. H x 1.3 in. V (67 mm x 33 mm) tube-tube spacing

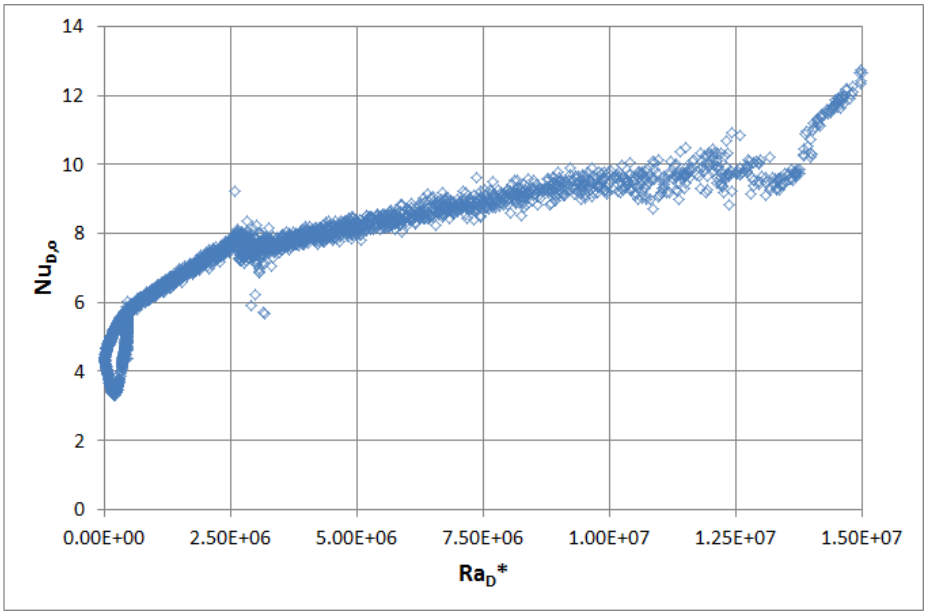

Figure 3.11: Heat extraction data taken in pool for 3/4 in. (19 mm) dia. thermally enhanced HDPE for 2.625 in. H x 2.625 in. V (67 mm x 67 mm) tube-tube spacing

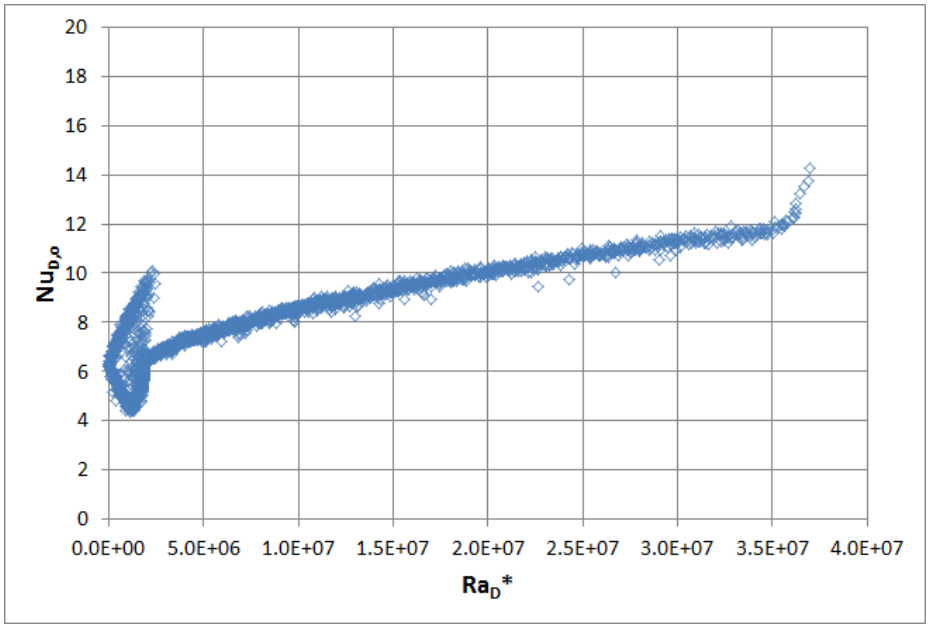

Figure 3.12: Heat extraction data taken in pool for 1-1/4 in. (32 mm) dia. thermally enhanced HDPE for 4.125 in. H x 2.625 in. V (105 mm x 67 mm) tube-tube spacing

From Figures 3.10, 3.11, and 3.12, we see several trends in the data that are worth noting:

The first is the trend shown near the right side of each plot where the slope of the data is much steeper than the majority of the data. This region represents the data taken during the initial startup period of the test. As the tests began, we can follow the data generated by following from the right side of each chart towards the lower left corner of each chart. This irregular data indicated at the right of each chart shows the initial period where the system is starting up and initial system transients are settling.

The second trend that should be highlighted is the irregular data shown near the left side of the charts. The reason for this is identified as the region where the density difference between the SWHE cold water plume and the surface water reverses. This occurs due to the maximum density of water which occurs at a temperature of 39.2°F (4°C) for pure water. In this region, the cold water plume that would be falling from the coil, changes direction and begins flowing upward. To illustrate this, if the SWHE cold water plume had a temperature of 40°F (4.4°C) and the surface water had a temperature of 45°F (7.2°C), the cold water plume would be more dense than the surface water and would naturally fall downward. The same could be said if the SWHE cold water plume were 38°F (3.3°C) with a 45°F (7.2°C) surface water temperature. However, if the SWHE plume were at a temperature of 33°F (0.6°C) and the surface water temperature were at 39°F (3.9°C), the SWHE cold water plume would flow upward.

This is illustrated in Figure 3.13 where the water density in kg/m^3 is plotted as a function of temperature in °C. Here, the previous point is illustrated to show the change in direction of the SWHE buoyancy plume. At point a) in Figures 3.10 and 3.13, the SWHE plume density taken at the outside film temperature (Equation 3.24) is greater than the pool water density taken at the pool temperature. This density imbalance is the driving force for natural convection. At point a) we can see that the density difference between plume and pool is significant, which corresponds to a

higher Nusselt number in Figure 3.10.

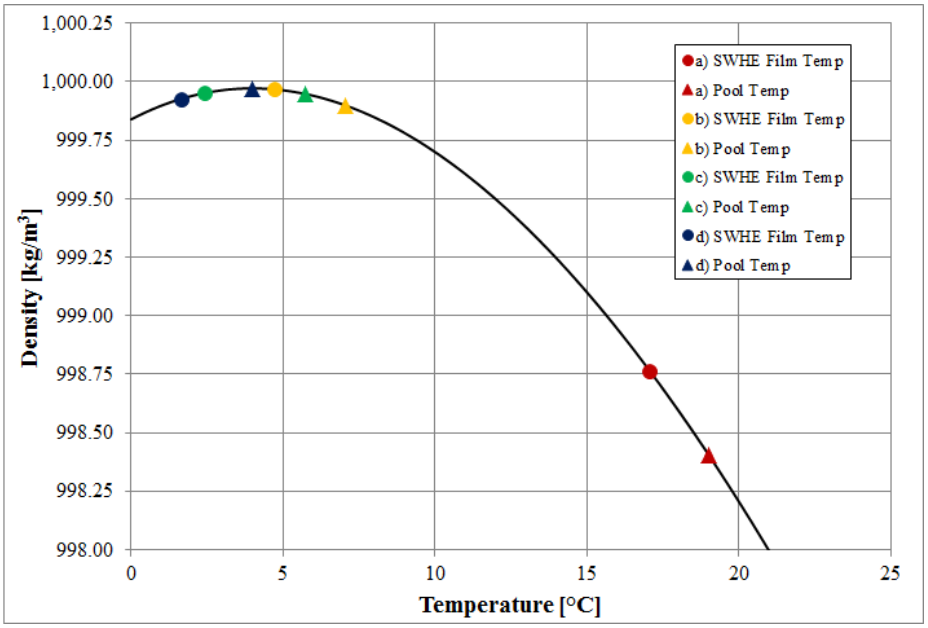

Figure 3.13: Points illustrating the buoyancy plume direction change in Figure 3.10

As we move from point a) to b), the density difference between the two points is quite small, resulting in smaller Nusselt numbers in Figure 3.10. Point c) illustrates a balance point where the density of the plume and the pool water are nearly equal, resulting in Nusselt numbers which are at the lowest point in Figure 3.10. This is also the point where the flow direction is changing. Finally, as we move to point d), the plume density is now less than the pool water signifying an upwardly buoyant plume.

Due to the fact that the SWHE is quite long (500 ft (152.4 m)), different locations along the tube length are expected to make this flow direction transition at different points in time. Because circulating fluid enters the heat exchanger at the bottom and exits at the top, the plume would transition to upward flow near the bottom of the SWHE before the upper layers would transition to upward flow. Other scenarios are likely as well.

I hypothesize that due to these two competing flow directions associated with different locations along the tube passing through the maximum density point at

different times, we see the external convective resistance increases substantially. Once the majority of the SWHE has transitioned to the upward flow regime, the external convective resistance is shown to decrease again. The lowest Nusselt number could be considered a "balance" point where we have similar magnitudes of upward and downward flow.

There is also some apparent hysteresis in the data as it passes through the maximum density point. I hypothesize this is due to the fact that with a downward flow, the coldest water settles at the bottom of the pool with little recirculation occurring. However, for the upward flow regime we will see that the coldest water will rise to the pool surface. As that water warms, it will then settle to the bottom of the pool and a recirculation zone will form. As a result of the physics associated with the various flow patterns, we expect to see hysteresis in the data near the maximum density point.

Table 3.4 shows the percentages of total thermal resistance each thermal resistance component makes up for this particular set of experimental data. The external convective resistance is greater, when compared to the percentages of total thermal resistance components for the pond heat rejection data from Table 3.3. Again, this is theorized to be due to the constrained nature of the pool.

Table 3.4: Average thermal resistance for each thermal resistance component as a percentage of total thermal resistance for pool heat extraction data

Tube Size	Material	$R_{conv,i}$	R_{cond}	$R_{conv,o}$	# Points
3/4 in. (19 mm)	TEHDPE	5.8%	32.2%	62.0%	4725
1-1/4 in. (32 mm)	TEHDPE	6.1%	35.1%	58.8%	3149

3.3.3 Coil Icing

The main purpose of moving the experiment to the indoor facility was to collect information regarding SWHE performance under heat extraction and coil icing conditions. Because there was only one test where ice was potentially formed on the coil while running in the pond, the data considered in this section will be taken from the heat extraction tests in the pool.

Shown in Figure 3.14 is a SWHE during a heat extraction test under fully iced conditions. The SWHE had the 2.625 in. H x 1.3 in. V (67 mm x 33 mm) tube-tube configurations on 3/4 in. (19 mm) SDR-11 thermally enhanced HDPE piping. In this figure, we can see that the lead pipes bringing circulating fluid to/from the SWHE are iced with frost. Looking closely we can see the ice layers that had formed on the SWHE.

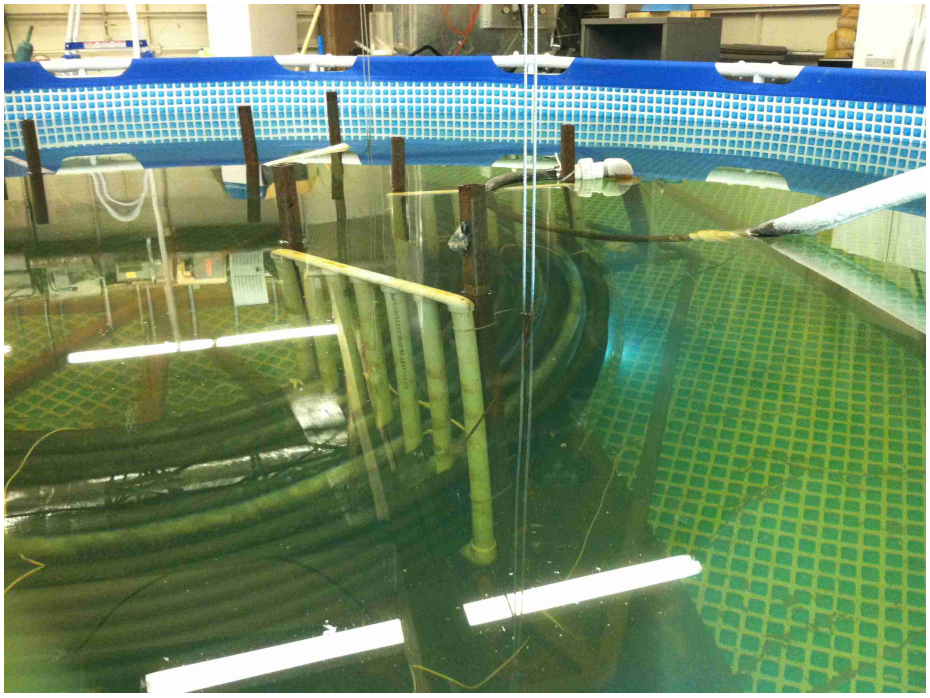

Figure 3.14: 3/4 in. dia. (19 mm) 2.625 in. H x 1.3 in. V (67 mm x 33 mm) SWHE that is fully iced

Figure 3.15 below shows some of the data collected from the coil shown above in

Figure 3.14 during the heat extraction test. Entering and exiting circulating fluid temperatures are shown, as well as the pool water temperature averaged across the depth of the heat exchanger. Also shown is the buoyancy force created from the ice formation on the SWHE. The buoyancy force peaks near 62 lb. (276 N). From the plot, we see that the coil temperatures begin to drop sharply as a direct result of the additional thermal resistance due to the ice formation.

The step in SHWE entering and exiting temperature after the SWHE is fully iced is the point where the large three ton (10.6 kW) heat pump was turned off while leaving the smaller one ton (3.5 kW) heat pump on. At this point, the coil was fully iced and buoyancy force was not increasing. Due to the limitations of the current system, the large heat pump was switched off to allow for coil deicing.

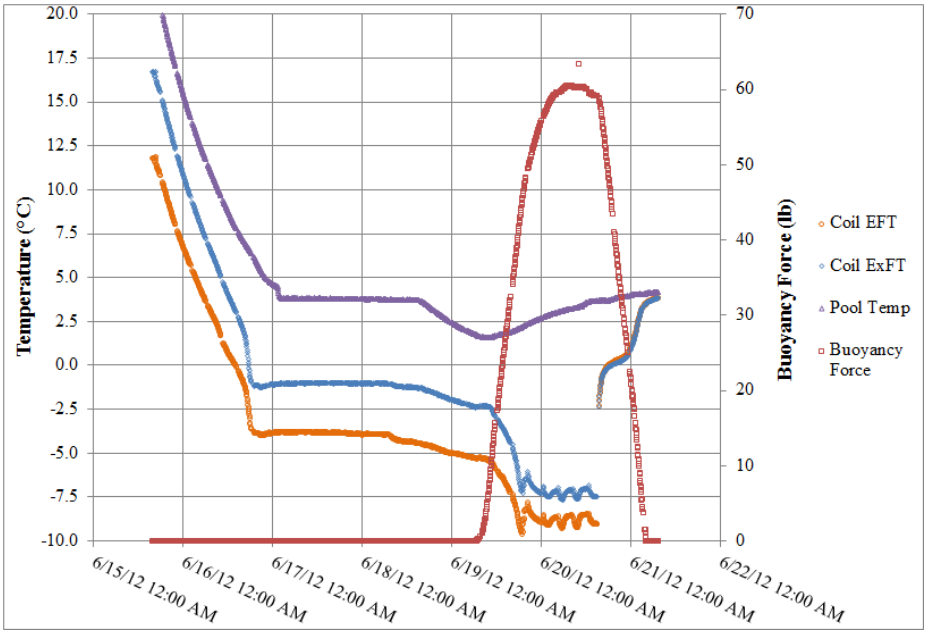

Figure 3.15: Coil temperature and buoyancy force plot from test in pool on 3/4 in. dia. (19 mm) 2.625 in. H x 1.3 in. V (67 mm x 33 mm) SDR-11 thermally enhanced HDPE

We can also see the pool temperatures begin to rise at the onset of ice formation. This occurs due to the decreased heat extraction rate which occurs after ice begins

forming on the tubes. This increase in pool temperature is the natural result of the decreased heat transfer rate combined with heat gain through the pool boundaries.

In Figure 3.16, we can see the coil heat transfer rate in conjunction with the buoyancy force. If we examine the graph relatively close, we can see that heat transfer continues at relatively the same level after the onset of ice formation when compared to the period of time immediately previous the onset of ice formation. The slope of the buoyancy force is also relatively constant.

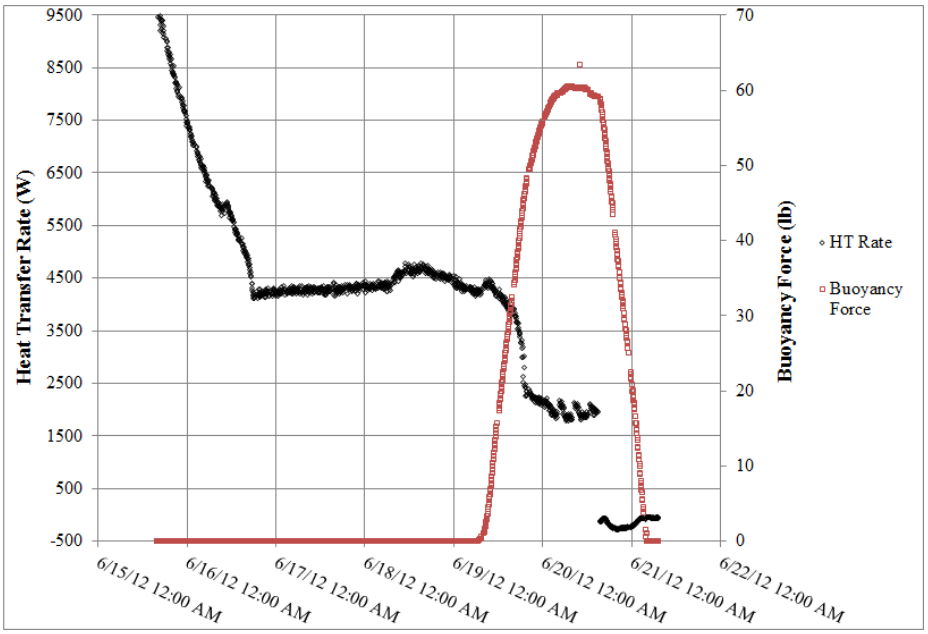

Figure 3.16: Coil heat transfer rate and buoyancy force plot from test in pool on 3/4 in. dia. (19 mm) 2.625 in. H x 1.3 in. V (67 mm x 33 mm) SDR-11 thermally enhanced HDPE

However, if we continue to examine Figure 3.16, we can see that the heat transfer rate drops suddenly and sharply, and immediately afterwards the slope of the buoyancy force also changes to a slope that is less steep. This is indicating the point where the tube-tube gap has bridged completely shut from the ice growth on the SWHE tubing. At this point, the heat transfer rate drops substantially and remains quite low for the remainder of the test.

We see from this experiment that extended run times on SWHEs under peak heating conditions could cause system capacity to be degraded to the point where the system is no longer able to provide sufficient heating. It could also potentially damage or destroy the SWHE. This could occur if the upward force created by the ice causes the SWHE to be buoyed up. This could damage pipes carrying the circulating fluid, or damage the SWHE. Heat pumps are typically equipped to protect against freezing. Unless alterations are made to the unit, the heat pump itself would not be expected to be damaged if these conditions occur.

The two heat pumps with a combined nominal nameplate capacity of four tons (14.1 kW) caused this heat exchanger to fully ice after approximately 36 hours of full load run time. More buoyancy force could have been generated had the tubes been configured on the largest horizontal and vertical tube-to-tube spacing. This would have allowed more room for ice to be formed on the tubes before tube-tube ice bridging occurs.

It is recommended that the tubes be kept spaced far apart if the system is intended to be used for heating purposes if icing conditions are expected to occur. This can be encountered anytime when the heat pump exiting fluid temperature is below the freezing point of water. As was noted in Figure 3.16, heat transfer rate degrades only slightly after the onset of coil icing, however, the coil heat transfer decreases sharply once tube-tube icing occurs. Keeping the tube separated by sufficient distance would allow for ice growth under peak loading conditions, but would also keep lake water in contact with the most surface area so that ice could melt quickly once load is reduced. If the heat exchanger is allowed to freeze in to a solid block of ice, melting will occur at a much slower rate.

3.4 Pool Data vs. Pond Data Comparison

Figures 3.17 through 3.19 show $Nu_{D,o}$ vs. Ra_D^* plots of the pond and pool data for heat rejection and extraction cases for three separate coil configurations. In all cases, the experimental Nusselt number as calculated from from data collected in the pond is higher than the Nusselt number as calculated from pool data.

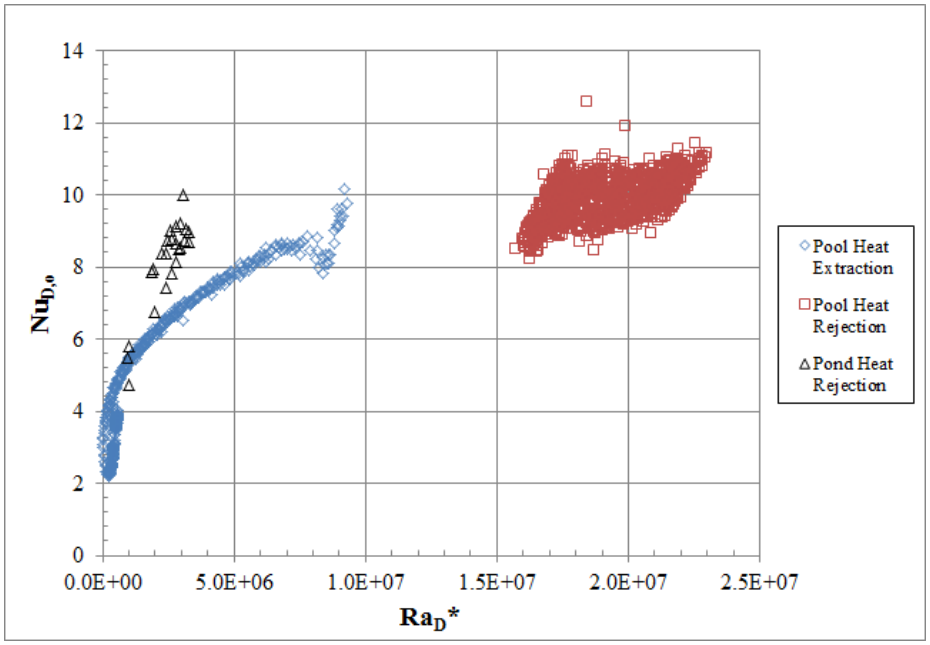

Figure 3.17: $Nu_{D,o}$ vs. Ra_D^* plot of pond and pool heat extraction and rejection data for the 3/4 in. (19 mm) dia. HDPE pipe with 2.625 in. H x 1.3 in. V (67 mm x 33 mm) tube-tube spacing

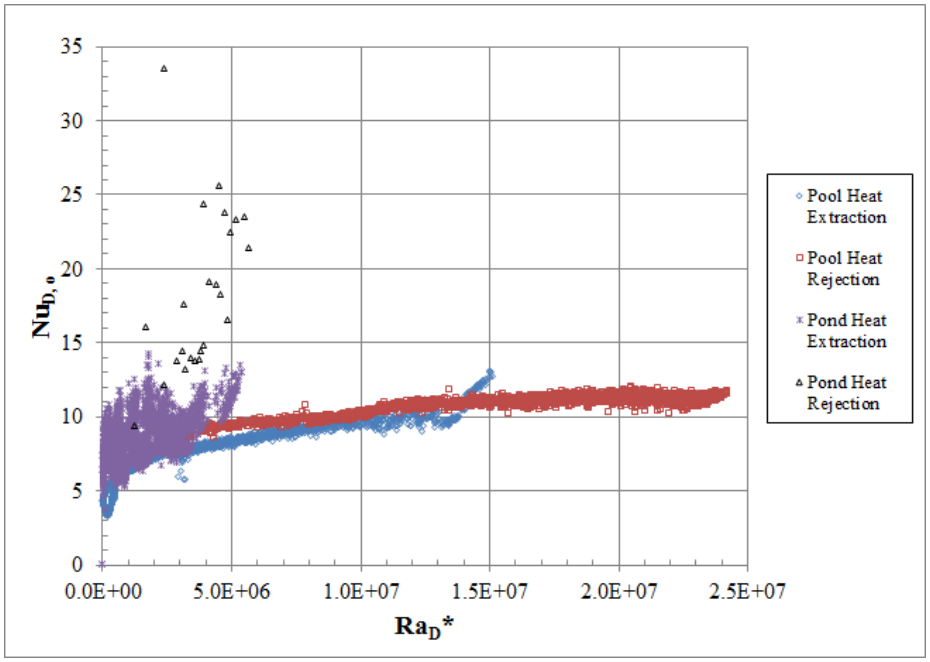

Figure 3.18: $\mathrm{Nu}_{D,o}$ vs. Ra_D^* plot of pond and pool heat extraction and rejection data for the 3/4 in. (19 mm) dia. HDPE pipe with 2.625 in. H x 2.625 in. V (67 mm x 67 mm) tube-tube spacing

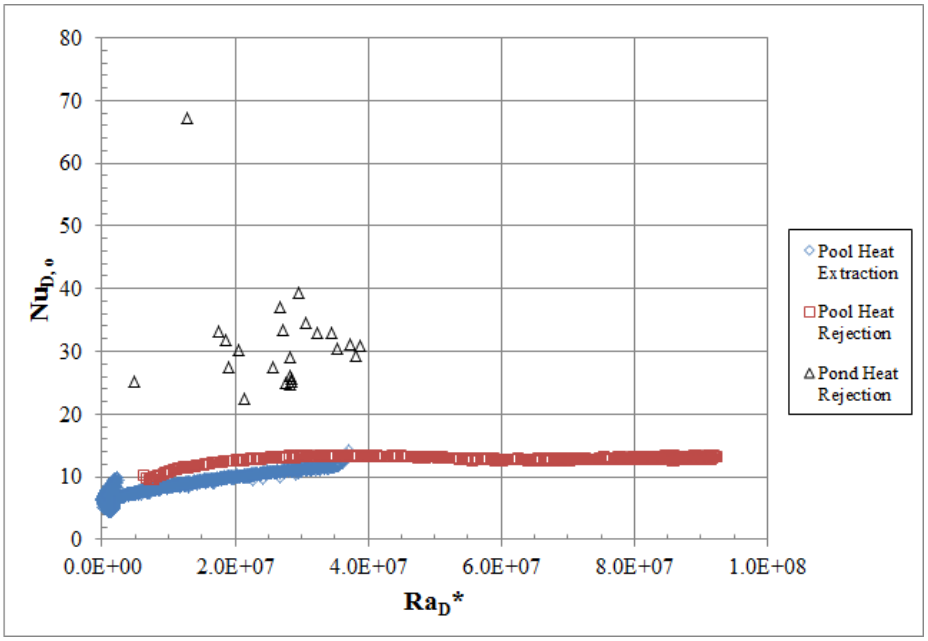

Figure 3.19: $\mathrm{Nu}_{D,o}$ vs. Ra_D^* plot of pond and pool heat extraction and rejection data for the 1-1/4 in. (32 mm) dia. HDPE pipe with 4.125 in. H x 2.625 in. V (105 mm x 67 mm) tube-tube spacing

This suggests that there is something about the laboratory experimental apparatus that does not represent realistic operating conditions. In this context, *realistic operating conditions* is defined as conditions under which we would expect actual SHWEs to operate. This would include being in a surface water body that is much deeper than the indoor test pool.

The pool is 15 ft (4.5 m) in diameter and is operating at water depth of 42 in. (1.1 m). Two of the coil configurations tested in the pool used 2.625 in. (67 mm) vertical tube-tube spacing. From Table 2.4 we can see that the nominal coil height is 14 in. (0.35 m) for these particular coil configurations. The coil was situated directly in the center of the pool in the lateral directions and was suspended approximately in the middle of the water column. Under these operating conditions, the coil is approximately 14 in. (0.35 m) above the pool bottom and 14 in. (0.35 m) below the water surface.

It is worth noting that all heat extraction data, along with the pool heat rejection data, were all collected with thermally enhanced HDPE. This thermally enhanced HDPE pipe has a thermal conductivity that is 75% higher (Gonthier 2012) than standard PE3408 HDPE. In order to assess the potential differences introduced in outside Nusselt numbers due to the variations in pipe thermal conductivity, a simulation was set up to simulate heat exchanger performance, while fixing certain critical parameters. The critical parameters which were fixed during the simulation are: SWHE (pipe) length, pipe diameters, SWHE diameters, SHWE configuration, circulating fluid flow rate, surface water temperature, heat pump load, and heat pump COP. The thermal conductivities for standard HDPE pipe, thermally enhanced HDPE, and copper were tested.

The details of this simulation will be discussed in detail in Section 5.1, but briefly explained here. The simulation uses the outside SWHE convection correlations developed in Chapter 4 to determine SWHE outside convection thermal resistance. Other calculations are similar to what was described in Section 3.1. The simulation is given a fixed inlet temperature, and from there it iteratively determines the required SWHE tube length to meet a fixed heat transfer rate. In order to fix the tube length, a range of inlet temperatures were given to the simulation and the results below were interpolated between data points to determine the desired information at the 'fixed' tube length. Table 3.5 shows the thermal resistances and overall heat transfer coefficient from the simulation and Table 3.6 shows the temperatures calculated from the simulation.

From Table 3.5, we see that changing the pipe wall thermal conductivity has little to no affect on the inside thermal resistance. This is expected since flow rate and pipe inside diameter are fixed. The minor variations can be attributed to the changing fluid properties due to mean fluid temperature variations. Pipe conduction resistance variations are attributed entirely to the different thermal conductivities of the pipe

Table 3.5: Fixed parameter simulation results: thermal resistances and overall heat transfer coefficient

Tube Material	$R_{conv,i}$	$R_{p,cond}$	$R_{conv,o}$	UA_s
	K/W	K/W	K/W	W/K
STD	$1.26 \cdot 10^{-4}$	$1.63 \cdot 10^{-3}$	$5.52 \cdot 10^{-4}$	434
TEHDPE	$1.30 \cdot 10^{-4}$	$9.73 \cdot 10^{-4}$	$5.52 \cdot 10^{-4}$	605
Cu	$1.38 \cdot 10^{-4}$	$1.71 \cdot 10^{-6}$	$5.54 \cdot 10^{-4}$	1447

Table 3.6: Fixed parameter simulation results: temperatures

Tube Material	$T_{f,in}$	T_{MFT}	$T_{f,out}$	$T_{p,s,i}$	$T_{p,s,o}$	$T_{film,o}$	Lake Temp
	°C	°C	°C	°C	°C	°C	°C
STD	34.3	31.3	28.7	30.7	23.6	22.3	21.1
TEHDPE	31.5	28.4	25.9	27.8	23.6	22.3	21.1
Cu	27.8	24.2	22.2	23.6	23.6	22.3	21.1

materials. This is because diameters and pipe length were all fixed.

Initially, outside convective resistance was expected to increase with increasing pipe thermal conductivity because all the temperatures, including pipe outside surface temperature, were expected to move closer to the surface water temperature. This would have resulted in a smaller temperature difference between the pipe outside surface and the lake temperatures, which would have resulted in a smaller outside film temperature and thus lower outside convection coefficient. However, this did not turn out to be the case. Table 3.6 shows the variations in entering, exiting, and mean fluid temperatures, as well as pipe surface temperatures. As expected, all temperatures did move closer to the surface water temperature, however, in this example, the outside film temperature did not change and therefore the driving potential for the outside convection remained constant.

This result was not expected initially; however, if we perform a surface heat bal-

ance on the exterior surface of the SWHE and perform some analysis of the fundamental equations, we will see that the results are plausible. Equation 3.25 shows a surface heat balance for the SWHE exterior surface where the pipe conduction heat transfer is balanced by the outside convective heat transfer.

$$\dot{Q}_{SWHE,p,cond} = \frac{T_{p,s,o} - T_{sw}}{R_{conv,o}} \tag{3.25}$$

Examining Equation 3.25, we will see that even by fixing heat transfer rate and surface water temperature, the pipe outside surface temperature and outside convective resistances are not known. However, we know that outside convective resistance is a function of Nusselt number, Nusselt number is a function of Rayleigh number, and Rayleigh number is a function of driving potential which is expressed as a temperature difference or a heat flux. This is shown in Equations 3.26, 3.27, and 3.28.

$$R_{conv,o} = f(Nu_{D,o}) \tag{3.26}$$

$$Nu_{D,o} = f(Ra \text{ or } Ra^*) \tag{3.27}$$

$$Ra \text{ or } Ra^* = f(T_{p,s,o} - T_{sw} \text{ or } \dot{q}) \tag{3.28}$$

Through careful examination we can see that driving potential, which is expressed as a temperature difference or a heat flux, is inversely proportional to outside convective resistance. Therefore, as driving potential increases outside convective resistance decreases. The reverse is also true. In our situation, because all other parameters, such as SWHE configuration, pipe diameter, surface water temperature, and heat transfer rate are all held constant, the driving potential and outside convective resistance must be the same if Equation 3.25 is to 'balance'.

Therefore, we do not expect the outside convection coefficients to be affected by tube thermal conductivity. Thus, the variations shown above in Figures 3.17, 3.18, and 3.19 cannot be attributed to pipe material changes.

Another possible theory to explain the differences in outside Nusselt numbers shown above in Figures 3.17, 3.18, and 3.19 is the differences in free stream distances around the SWHE between the pond and the pool. Hansen (2011) conducted a "Lake Bottom Proximity" test where the affects of testing the SWHE suspended in the water column as is shown in Figure 2.4, when compared to testing on the pond bottom were tested. For this test, the SWHE was allowed to reject heat under steady-state conditions while being suspended by the buoys in the pond. Once steady-state conditions were achieved, the SWHE was then lowered to the pond bottom and allowed to run again until steady state conditions were achieved.

From this experiment, Hansen (2011) showed that the affects of the SWHE being on the pond bottom showed an increase in outside convection coefficient of around 8%. He did, however, state that this result was within experimental uncertainty and that "no definitive conclusion could be drawn from the test." This test was in heat rejection mode, therefore, the buoyant plume would be expected to flow upwards from the coil. Since the upper side of the coil was not subjected to a "proximity test", nor was the coil constrained laterally, no conclusions can be drawn from his experiment.

I hypothesize that due to the fact that the depth of the pool is much less than the depth of the pond, the buoyant plume is constrained in either mode of operation. This may be the cause for the increased convective resistance in the pool when compared to experiments in the pond. We can also point out that in the pond the wind, sun, and precipitation will cause three dimensional mixing which will definitely not be uniform throughout the pond. There also may conceivably be affects from various varieties of aquatic vegetation and wildlife.

3.5 Experimental Uncertainty

3.5.1 Measurement Uncertainty

Uncertainty in the inner and outer HDPE pipe diameters was determined by sampling 1 ft. (0.3 m) sections from each end of each coil tested. The inside and outside pipe diameters were then measured using telescoping gauges and a micrometer calibrated to 0.0001 in. (0.00254 mm), with the exception of the 1 in. pipe inside diameter; a telescoping gauge with the measurement range required to measure this inside diameter could not be located at the time the measurements were performed. The outside and inside diameter of each end of the 1 ft. (0.3 m) sections were measured at four different angles: 0-180°, 90-270°, 45-235°, and 135-315°. The four measurements were necessary to account for potential eccentricity in the pipe and to determine the average pipe diameter as is shown in Equation 3.29.

$$D_{sec} = \frac{D_{sec,1} + D_{sec,2} + D_{sec,3} + D_{sec,4}}{4} \tag{3.29}$$

To determine the uncertainty in the pipe diameters, all of the average section diameters (Equation 3.29) for a give pipe size were taken and the standard deviation was determined as is shown in Equation 3.30 (Taylor 1997).

$$\sigma_D = \sqrt{\frac{1}{N_{D,sec} - 1} \sum (D_{sec} - \bar{D})^2} \tag{3.30}$$

For reference, Table 3.7 shows the HDPE pipe dimensions as specified in ASTM (2012). The average outside and inside pipe diameters as calculated from the standard can be seen in Table 3.8. Incidentally, the average diameters shown in Table 3.8 are the dimensions listed in the HDPE manufacturer dimensional specification sheets.

Table 3.9 shows the average inside and outside pipe diameters, as well as the absolute percent error when compared to the average diameters shown in Table 3.8. Because the average measured diameters for each pipe size are all less than 1% differ-

Table 3.7: Specified HDPE pipe dimensions from ASTM (2012)

Nominal Size	D_o	D_o Tolerance	Min. Wall Thickness	Wall Tolerance
		in. (mm)		
3/4 (19)	1.050 (26.27)	±0.004 (0.102)	0.095 (2.41)	+0.02 (0.51)
1 (25)	1.315 (33.40)	±0.004 (0.102)	0.120 (3.05)	+0.02 (0.51)
1-1/4 (32)	1.660 (42.16)	±0.004 (0.102)	0.151 (3.84)	+0.02 (0.51)

Table 3.8: Mean outside and inside pipe diameter for HDPE pipe from ASTM (2012)

Nominal Size	$D_{o,ave}$	$D_{i,ave}$
	in. (mm)	
3/4 (19)	1.050 (26.27)	0.844 (21.44)
1 (25)	1.315 (33.40)	1.059 (26.89)
1-1/4 (32)	1.660 (42.16)	1.342 (34.09)

ent from the mean diameter as determined by ASTM (2012), we can assume that the diameter measurements will all be normally distributed around the mean diameters indicated in Table 3.8.

Table 3.9: Mean measured inside and outside diameter and absolute percent error from ASTM (2012)

Nominal Size	$D_{o,ave}$	|% Error|	$D_{i,ave}$	|% Error|
		in. (mm)		
3/4 (19)	1.059 (26.92)	0.88	0.848 (21.54)	0.47
1 (25)	1.322 (33.58)	0.52	N/A	N/A
1-1/4 (32)	1.666 (42.32)	0.36	1.341 (34.06)	0.07

Table 3.10 shows the standard deviations of the measured pipe diameters. Because the two standard deviations will capture the 95% of the values that are normally distributed about the measured mean, two times the standard deviation indicated in Table 3.10 is taken as the pipe diameter uncertainty.

Temperature sensors were calibrated as described in Section 2.3.2. There, an

Table 3.10: Standard deviations of measured pipe diameters

Nominal Size	$\sigma_{D,o}$	$\sigma_{D,i}$
	in. (mm)	
3/4 (19)	0.0017 (0.043)	0.0024 (0.061)
1 (25)	0.0007 (0.017)	N/A
1-1/4 (32)	0.0028 (0.071)	0.0046 (0.117)

example was given for which the correlated maximum absolute error was shown to be 0.11°F (0.06°C), which corresponds to a maximum absolute percent error of 0.13%. As a conservative estimate, thermsitor uncertainty was taken to be 0.18°F (0.1°C).

Flow meters were calibrated as described in Section 2.3.4. The "Omega" flow meter was calibrated to a maximum absolute percent error within 0.6% and the "Gem" flow meter was calibrated a maximum absolute percent error within 1.46%. These values were taken as the calculated flow measurement uncertainty.

The uncertainty from each of the SWHE geometrical parameters are shown below in Table 3.11. SWHE inside and outside diameters were determined by using a tape measure. Uncertainty from the inside and outside SWHE diameter measurements were given based on the authors judgment of the measurement accuracy. SWHE length was not measured by the author. Coils were ordered from the manufacture to be 500 ft. (152.4 m) in length and the SWHE length uncertainty is another estimate from the author of the uncertainty in SWHE length.

Table 3.11: Experimental uncertainty for SWHE measured geometrical parameters

Parameter	Uncertainty
$w_{SWHE,D,o}$	± 1 in. (25 mm)
$w_{SWHE,D,i}$	± 1 in. (25 mm)
w_L	± 3.9 in. (0.1 m)

3.5.2 Uncertainty Analysis Methodology

The uncertainty analysis was performed in order to quantify the uncertainty associated with the measured data. This uncertainty analysis gives an indication of the potential errors associated with the measured data and how the measurement uncertainty affects the analysis. It was also important in order to make an educated decision regarding which data points will yield the best correlation for outside convective resistance. From Hansen (2011), an upper limit of 70% was used as the upper limit for outside Nusselt number uncertainty due to the large amount of scatter and uncertainty in the data. Hansen (2011) performed an uncertainty analysis as is outlined in Holman & Gajda (1984) and shown in Equation 3.31. Using this method, the uncertainty of the independent variables of a given parameter are summed together in quadrature to form the parameter's total uncertainty. This method assumes that all variables are independent from one another.

$$U_F = \sqrt{\left(\frac{\partial F}{\partial x_1} w_1\right)^2 + \left(\frac{\partial F}{\partial x_2} w_2\right)^2 + \cdots + \left(\frac{\partial F}{\partial x_n} w_n\right)^2} \tag{3.31}$$

After examining the uncertainty results from Hansen (2011), it was apparent that some steps could be taken to minimize the experimental uncertainty. This is because of the fact that some variables, which were treated as independent by Hansen (2011), were not truly independent. Also from Hansen (2011), the data was shown to have a high sensitivity to inside pipe diameter. In order to account for this, samples from HPDE pipes were taken and measured in order to estimate the uncertainty of the outside and inside diameters. This is in contrast to taking the uncertainty from ASTM (2012), as was done in Hansen (2011).

The uncertainty analysis performed for this work was performed, generally, as was performed in Hansen (2011) and outlined in Holman & Gajda (1984), however, a few critical adjustments were made. These adjustments affect the way the heat transfer rate uncertainty and pipe thermal resistance uncertainty were calculated.

Generally when calculating a heat exchanger's heat transfer rate (Equations 3.1 and 3.2) we are not primarily concerned with absolute temperature measurement. We are, however, primarily concerned about the overall temperature difference between the heat exchanger inlet and outlet. If there is expected uncertainty in both the inlet and outlet temperature measurement, the relative proximity of the temperature measurements to one another can greatly affect the heat transfer uncertainty.

To illustrate this point, if the uncertainty of inlet and outlet temperature measurements is ± 0.18°F (0.1°C), and the inlet and outlet temperatures were measured to be 66.2°F (19.0°C) and 68°F (20.0°C), respectively, then the heat transfer uncertainty would be expected to be quite high. Similarly, if the inlet and outlets were measured to be 50.0°F (10.0°C) and 86°F (30.0°C), respectively, then the heat transfer uncertainty would be expected to be quite low.

To account for uncertainty in the heat transfer, Equation 3.31 was modified to account for this sensitivity to temperature difference as is shown in Equation 3.32.

$$U_{\dot{Q},SWHE} = \sqrt{\left(\frac{w_{\dot{m}}}{\dot{m}}\right)^2 + \left(\frac{w_{cp}}{c_p}\right)^2 + \left(\frac{\sqrt{w_{T,f,in}^2 + w_{T,f,out}^2}}{T_{f,in} - T_{f,out}}\right)^2} \tag{3.32}$$

This formulation weights the uncertainty of the temperature difference, rather than simply the uncertainty of each temperature measurement independently. As the temperature difference becomes small, the weight of their uncertainty will have a larger effect than would occur if the temperature difference is quite large.

The only other instance where the uncertainty analysis deviates from what is shown in Equation 3.31 is when calculating the experimental uncertainty of the pipe conduction resistance (Equation 3.15). This is shown below in Equation 3.33 where the D_o/D_i is treated as one term.

$$U_{R,cond} = \sqrt{e_{D_o/D_i}^2 + e_{kp}^2 + e_L^2} \tag{3.33}$$

where:

$$e_{D_o/D_i} = \frac{\partial \dot{R}_{cond}}{\partial (D_o/D_i)} \cdot w_{D_o/D_i}$$

$$e_{k_p} = \frac{\partial \dot{R}_{cond}}{\partial k_p} \cdot w_{kp}$$

$$e_L = \frac{\partial \dot{R}_{cond}}{\partial L} \cdot w_L$$

The reason for this is because the outside and inside pipe diameters are expected to vary together. This could occur due to pipe pressure or temperature changes which could cause the pipe to expand or contract.

All SWHEs tested used HDPE tubing with the same diameter ratio, which is the ratio of pipe outside diameter to pipe wall thickness, as is shown in Equation 3.34. From this equation, it can be shown that the ratio of outside pipe diameter to inside pipe diameter is constant for all pipes with the same diameter ratio. This expression is shown in Equation 3.35

$$SDR = \frac{D_o}{t} \tag{3.34}$$

$$\frac{D_o}{D_i} = \left(1 - \frac{2}{SDR}\right)^{-1} \tag{3.35}$$

Due to the fact that the measured diameters are expected to be normally distributed about the average diameter as was shown previously, two times the standard deviation of the measured outside diameter to inside diameter can be used and the uncertainty for D_o/D_i, w_{D_o/D_i}. Also, because all pipe sizes are expected to have the same ratio of outside to inside diameter, the analysis can be simplified to only use one value of w_{D_o/D_i} for all pipe sizes. From the measured pipe diameters, the standard

deviation for all ratios of measured outside to inside pipe diameter was determined to be 0.0048 in. (0.123 mm).

The experimental uncertainty for each series of tests is broken down in the following sections by applying the previously described methods.

3.5.3 Pond Heat Rejection Data Uncertainty

In Figure 3.20 we can see a histogram of the experimental outside Nusselt number uncertainty from the data collected in the pond during the heat rejection experiments. Experimental uncertainty is lower when compare to the experimental uncertainty from Hansen (2011). This is attributed to tighter uncertainties on pipe diameters, as well as the improved methods for determining heat transfer rate uncertainty and pipe conduction resistance uncertainty as was explained in Section 3.5.2.

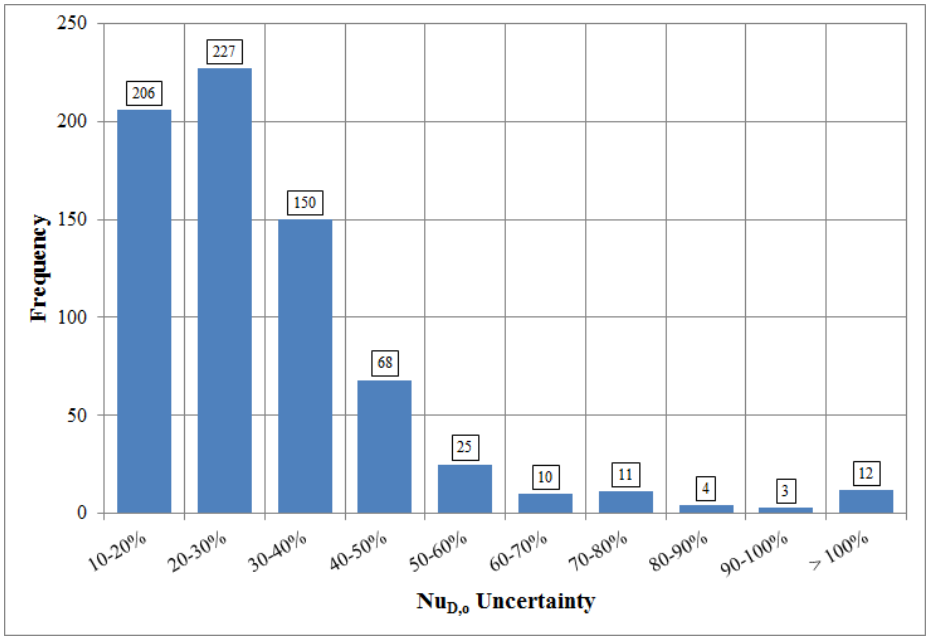

Figure 3.20: Pond heat rejection data outside Nusselt number uncertainty histogram

In Figure 3.21, we can see that the heat transfer uncertainty drops with increasing heat transfer rate. This occurs as expected due to the way heat transfer uncertainty is calculated.

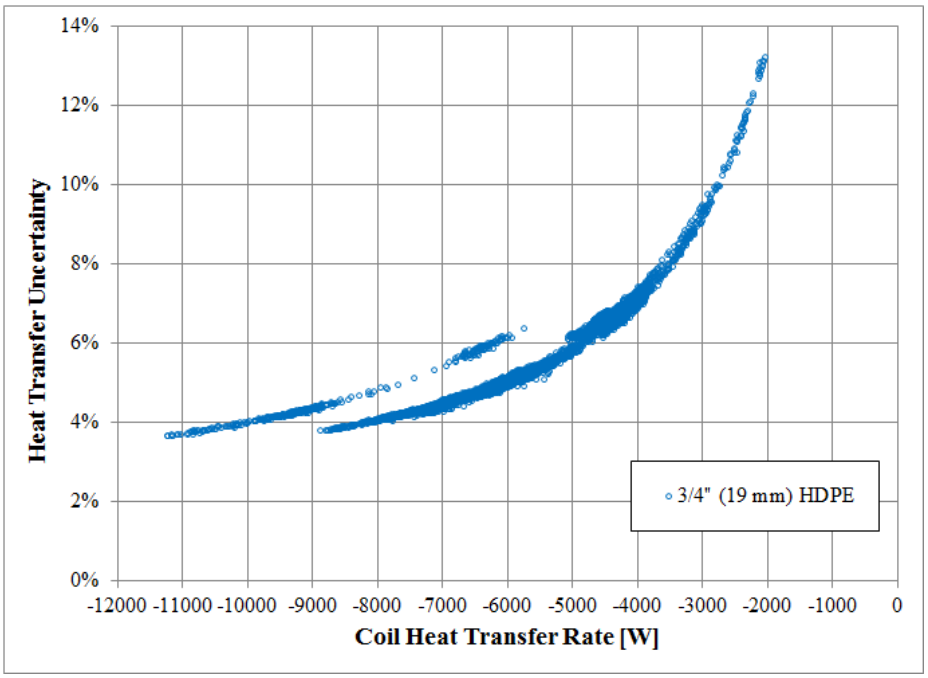

Figure 3.21: Pond heat rejection data heat transfer uncertainty vs. SWHE heat transfer rate

Another point that can be clearly seen in Figure 3.21 is the distinction between the discrete tube sizes. This is directly due to the increase in flow rate between the tube sizes. This effect is due to the smaller temperature difference across the SWHE which necessarily must occur if flow rate is increased and heat transfer rate is held constant.

Given that this data was collected outdoors in an open pond, the estimated heat transfer uncertainty appears to be reasonably good. This is primarily due to the fact that flow meters and temperature sensors were tightly calibrated. Great care was taken to preserve these calibrations, as this was one of the few parameters that could be controlled when experimenting in a highly variable environment.

In Figure 3.22, we can see the outside Nusselt number uncertainty plotted against the heat transfer rate. Here, we also see decreasing Nusselt number uncertainty with increasing heat transfer rate. Also visible to a small degree is the distinction between

different tube sizes. There is also a large degree of scatter visible in the plot. Even though flow and temperature sensors were tightly calibrated, and numerous other steps were taken to tighten the experimental uncertainty, we cannot get away from the fact that this data was collected in an uncontrolled environment. The scatter that is seen in the plot is largely due to the parameters which were out of our control. A few examples of these parameters are: wind, ambient temperature, underwater currents and eddies, aquatic wildlife, etc.

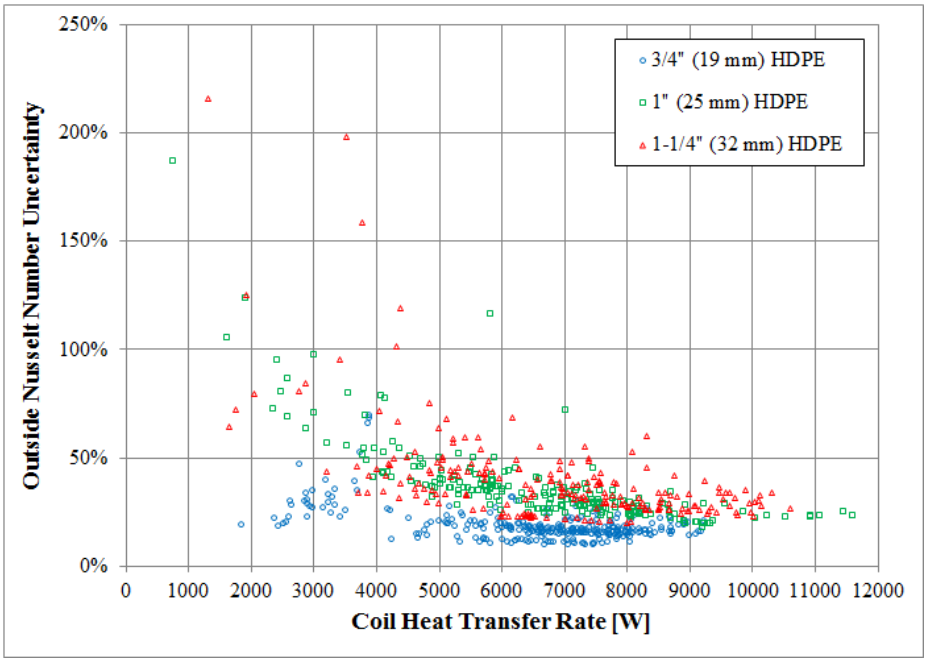

Figure 3.22: Outside Nusselt number uncertainty vs. coil heat transfer rate

3.5.4 Pond Heat Extraction Data Uncertainty

Figure 3.23 shows a histogram plot of the Nusselt number uncertainty for the pond heat extraction data. From this we can see that the pond heat extraction data has Nusselt number uncertainty values that are similar to the majority of the data taken in the pond during the heat rejection experiments. Again, this is an indication of the variability in the environment when testing in realistic operating conditions.

Heat transfer uncertainty is plotted against heat transfer rate in Figure 3.24. Here,

again we see that the heat transfer uncertainty is quite good at high heat transfer rates. Outside Nusselt number uncertainty is plotted against heat transfer rate can be seen in Figure 3.25. The scatter in the data is due to the highly uncontrolled nature of the environment in which the data was collected.

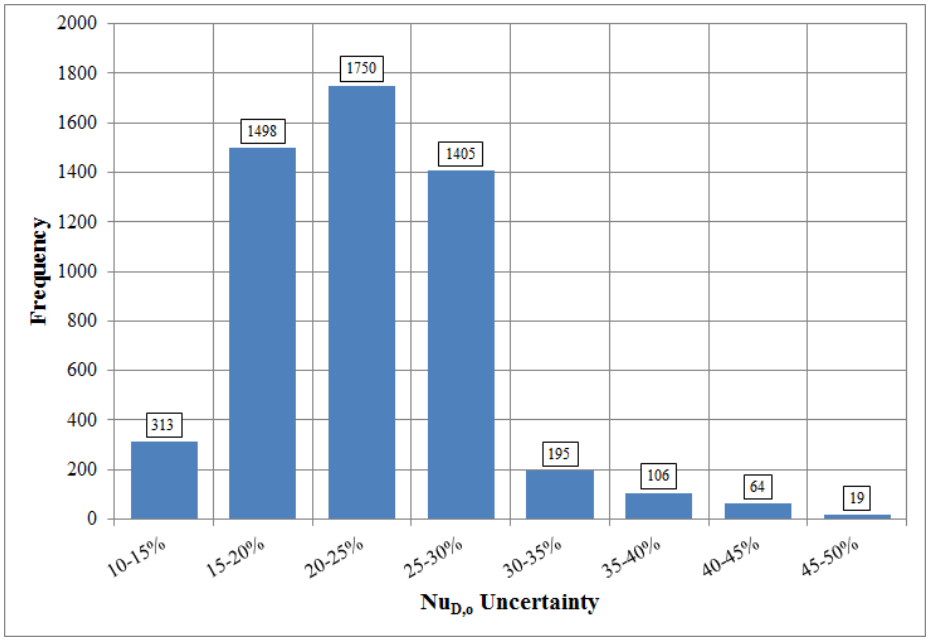

Figure 3.23: Pond heat extraction data Nusselt number uncertainty histogram

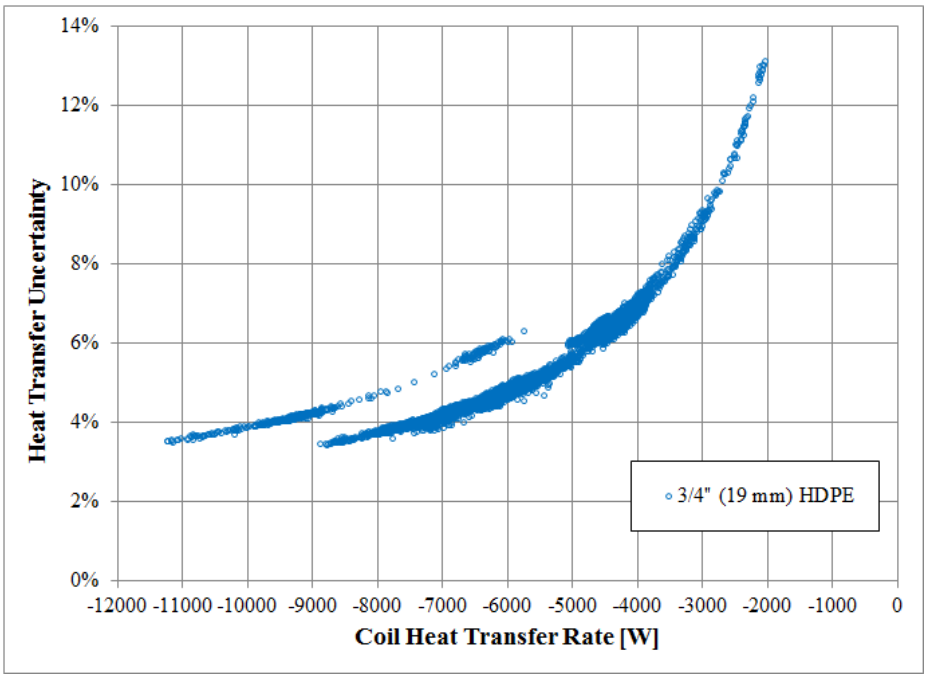

Figure 3.24: SWHE heat transfer uncertainty vs. SWHE heat transfer rate

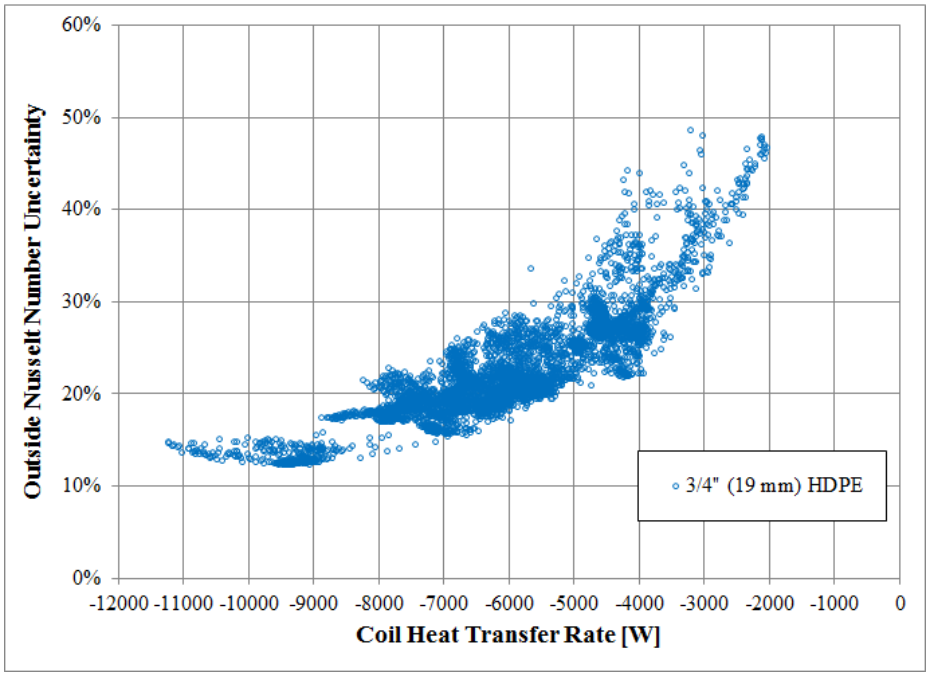

Figure 3.25: Pond heat extraction data outside Nusselt number uncertainty vs. coil heat transfer rate

3.5.5 Pool Heat Rejection Data Uncertainty

In Figure 3.26 we can see a histogram plot of the outside Nusselt number uncertainty for the pool heat rejection data. Nusselt number uncertainty is shown to be less than the uncertainty in the pond heat rejection data. This relates back to the fact that experiments performed in the pool had conditions which were more tightly controlled. In the pool, the pool water was not exposed to wind or other environmental conditions as occurred in the pond.

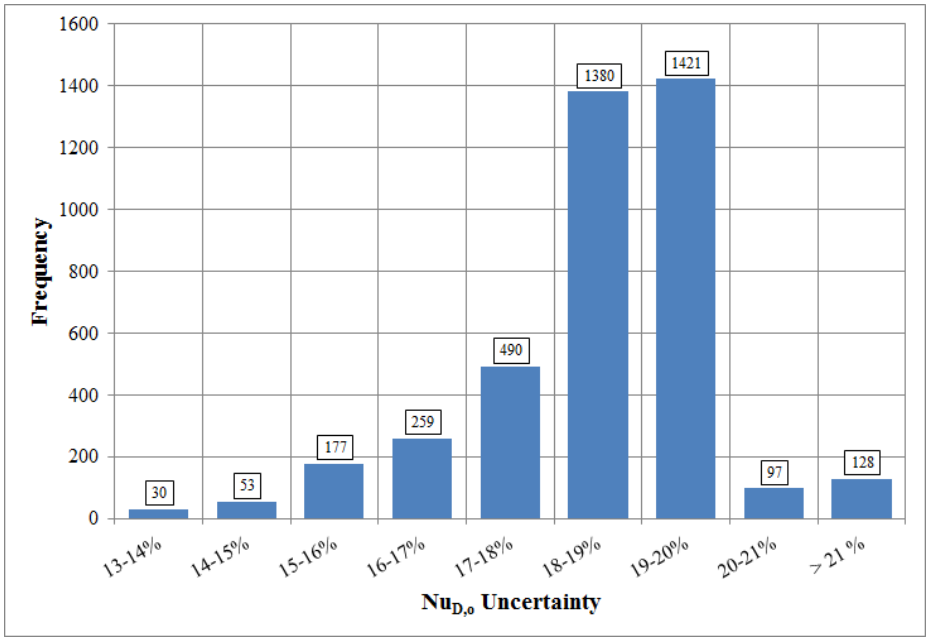

Figure 3.26: Pool heat rejection data Nusselt number uncertainty histogram

Figure 3.27, we can see the heat transfer uncertainty is quite low over the entire range of test data. The heat pumps used to perform heat rejection tests were not variable speed machines and any heat transfer variations seen are a direct result of machine performance varying over the course of the test. Here again the larger tube size is shown to have a higher heat transfer uncertainty, which is due to the changing flow rates between the two tube sizes.

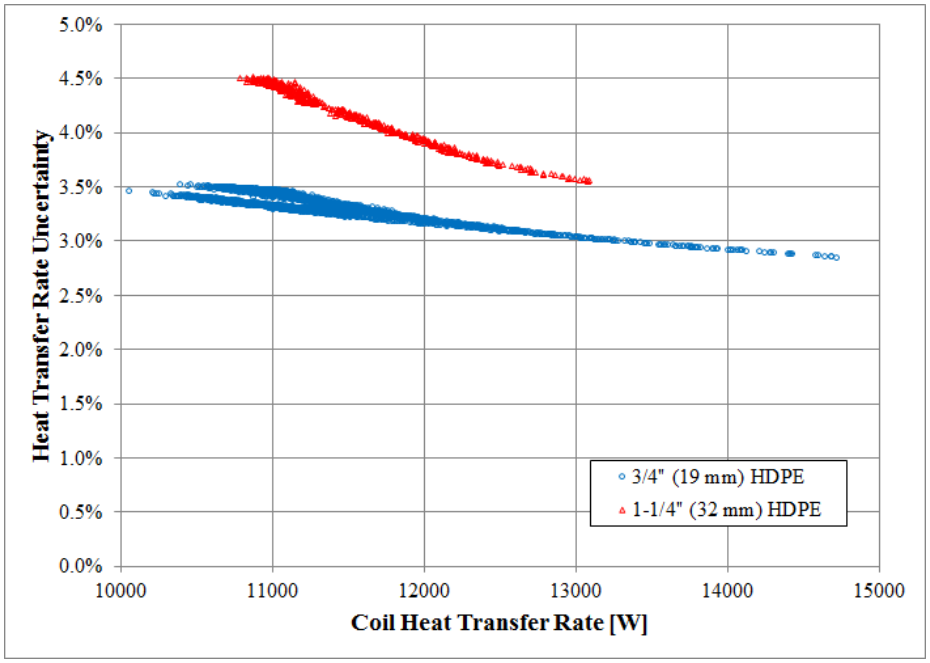

Figure 3.27: Pool heat rejection data heat transfer uncertainty vs. SWHE heat transfer rate

In Figure 3.28 we can see the outside Nusselt number uncertainty plotted against SWHE heat transfer rate. Some scatter is visible in the data, but the outside Nusselt number uncertainty is significantly less than the outside Nusselt number uncertainty of the pond heat rejection data.

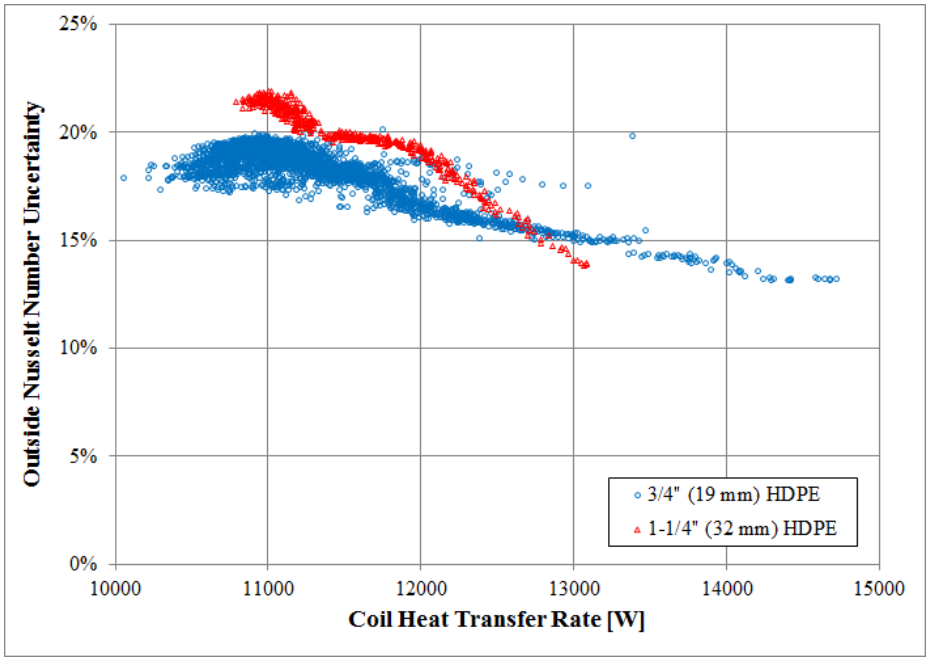

Figure 3.28: Pool heat rejection data outside Nusselt number uncertainty vs. SWHE heat transfer rate

3.5.6 Pool Heat Extraction Data Uncertainty

Figure 3.29 shows a histogram plot of the outside Nusselt number uncertainty for the pool heat extraction data. In Outside Nusselt number uncertainty is similar to the previous data sets. Figure 3.30, we see the heat transfer uncertainty plotted against the heat transfer rate. This again is similar to the results presented previously.

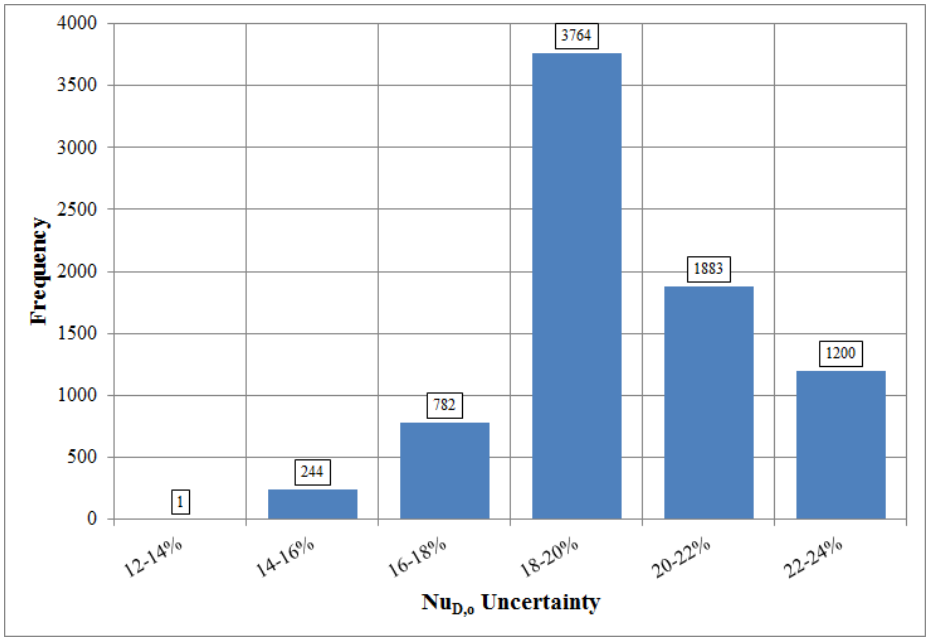

Figure 3.29: Pool heat extraction data Nusselt number uncertainty histogram

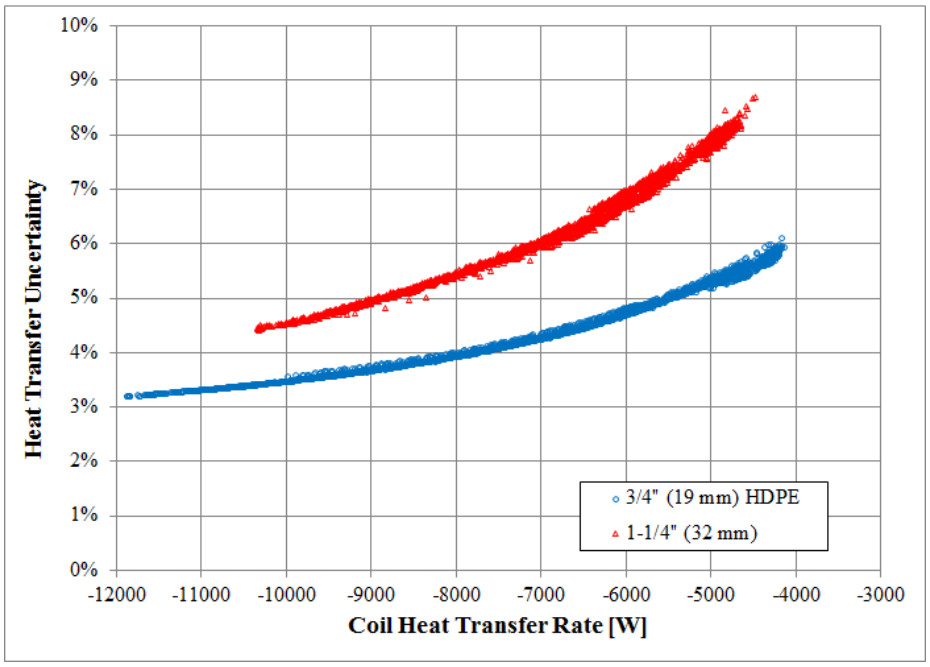

Figure 3.30: Heat transfer uncertainty vs. heat transfer rate for the pool heat extraction data

Figure 3.31 shows the outside Nusselt number uncertainty plotted against heat transfer rate. It is worth noting that for these tests, circulating fluid flow rate dropped

by about 18% for the 1-1/4 in. (32 mm) test, and about 27% for the 3/4 in. (19 mm) tests. This was due entirely to the viscosity of the circulating fluid increasing as the circulation fluid cooled. Additionally, the heat transfer rate dropped due entirely to the performance degradation of the heat pumps when operating at colder temperatures.

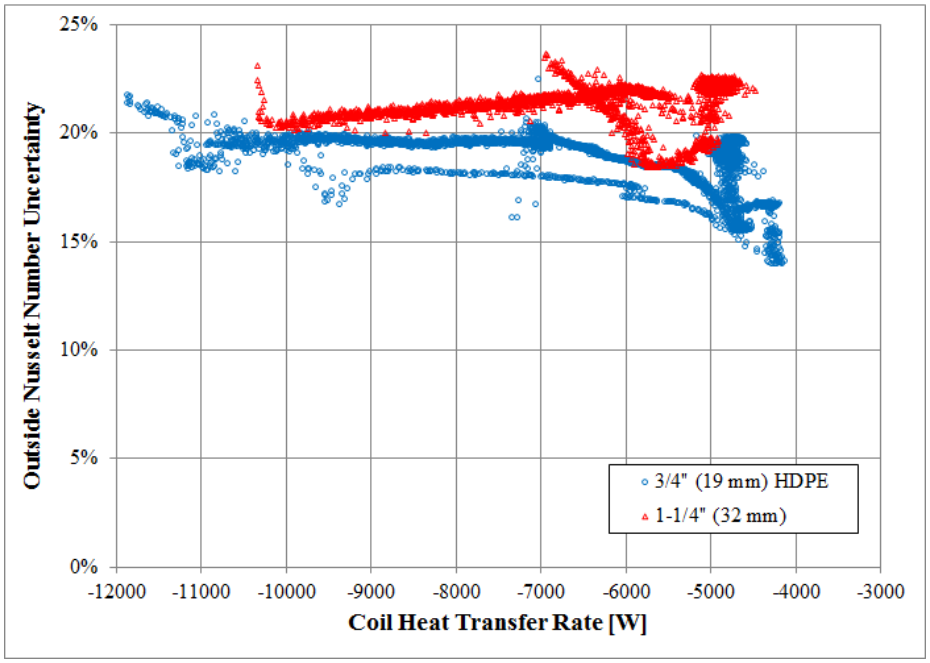

Figure 3.31: Outside Nusselt Number Uncertainty Plotted Against Coil Heat Transfer Rate for the Pool Heat extraction Data

CHAPTER 4

CONVECTION CORRELATION DEVELOPMENT AND VALIDATION

4.1 Correlation Optimization Methodology

To determine the convection correlations developed in this section, a correlation form was proposed, and the correlation parameters were determined through parameter estimation by using the Nelder & Mead (1965) simplex algorithm which is a direct search method used for finding the optimum value of the objective function. In our case, the objective function was the sum of the squared error of the outside Nusselt number. This method, however, is not fool proof and reasonable initial guesses and step sizes must be selected so that the solution converges on a global minimum, rather than a local minimum. Once a solution has been determined, the algorithm should then again be restarted using the optimized solution from the first iteration as the initial guess for the second iteration. This helps assure that the method has converged on the global solution.

In order to optimize the convection correlations developed in this chapter, the sum of the squared error for the outside Nusselt number was used as the optimization parameter to be minimized. To perform the optimization, the outside Nusselt number was defined primarily as a function of the modified Raleigh number. Other parameters such as the ratio of horizontal and vertical tube-tube spacing to outside pipe diameter ($\Delta x/D_o$ $\Delta y/D_o$) were also used to correlate SWHE performance. An example form of the correlation equation can be seen in Equation 1.1, which is the correlation form use by Hansen (2011).

To perform the optimization, the squared error was determined from Equation 4.1, which is the squared difference between the correlated Nusselt number and the experimental Nusselt number. Equation 4.2 can then be used to determine the sum of the squared error which was then minimized using the simplex method.

$$\mathrm{SQE} = (\mathrm{Nu}_{D,o,corr} - \mathrm{Nu}_{D,o,exp})^2 \tag{4.1}$$

$$\mathrm{SSQE} = \sum_{n=1}^{N_{tot}} \mathrm{SQE} \tag{4.2}$$

4.2 Convection Correlations

4.2.1 Convection Correlation Development Methodology

Correlation development and optimization began initially by optimizing separate outside convection correlations based solely on statistical measures for each data set. This means that there was a specific external convection correlation for each of the pond and pool heat extraction and heat rejection data sets which were optimized to find the minimum sum of the squared error value as shown in Section 4.1. However, once this was completed, it was observed in several heat transfer texts (Incropera et al. (2007), Cengel & Ghajar (2011)) that it is common for the Rayleigh number exponent to be set equal to 1/3 for free convection correlations.

It was also desirable, if feasible, that there be a simple scalar multiplier to switch from a correlation applicable in bodies of deep surface water where convective currents are likely to move freely, and bodies of surface water were convective currents are likely to be constrained. This is due to the discrepancy in Nusselt numbers observed between the pool and the pond data which was described in Section 3.4.

In an effort to test how well these qualifications could be met, a base data set was selected for heat extraction and heat rejection. Because the pond heat rejection

data contained 27 SWHE geometrical variations, it was selected as the base heat rejection data set. This is in comparison to the alternative data set for the pool heat rejection data which only contained three separate SWHE geometrical configurations. For the base heat extraction data set, the pool data were selected. The pool heat extraction data set contained three SWHE geometrical variations, whereas the pond heat extraction data set contained only one, and thus, constituted the alternative data set.

Each base data set was then taken; Rayleigh number exponents were fixed at 1/3; and the external convection correlation was optimized to best fit the data. Then, the convection correlation derived from the base case was taken and a multiplier was then optimized to proportionally scale the correlation up or down to best fit the alternative data set.

Upon examining the results and comparing the results with the results from the individually optimized convection correlations, it was determined that this approach was acceptable. This was because Nusselt number RMSE increased by 3.7% at most across all four data sets when compared to the individually optimized correlations. The average Nusselt number RMSE increase across the four data sets was 1.5%. For the heat transfer comparisons, heat transfer RMSE increased by 5.9% at most with an average increase of 2.4%. From this, it was decided that the increase in error when compared to the experimental data was acceptable due to the simplifications the method offered.

In the following sections, the convection correlations developed for each data set will be outlined and shown. The Nusselt number validation and heat transfer validation against the experimental data will also be shown.

4.2.2 Pond Heat Rejection Data Convection Correlation

From the pond heat rejection data the convection correlation initially given by Hansen (2011) in Equation 1.1 was updated based on the augmented data set with the additional eight heat SWHE configurations. Based on the testing, it was observed that a lower limit for Nusselt number existed which was not indicated in Equation 1.1. This is visible in Figure 3.2 where 5 is approximately the lowest Nusselt number recorded. To account for this lower limit, the form of the Nusselt number correlation was modified slightly to include a constant, as can be seen in Equation 4.3. Also included in the correlation is the scalar 'a' which will be used later to scale the correlation to best fit the alternative data set. Applying the optimization algorithm yielded Equation 4.4 as the final outside Nusselt number correlation for the pond heat rejection data set. The correlation's range of applicability can be seen Table 4.1.

$$\mathrm{Nu}_{D,o} = a \cdot \left(b + c \cdot \mathrm{Ra}_{D,o}^{*d} \cdot \left(\frac{\Delta y}{D_o} \right)^{e} \cdot \left(\frac{\Delta x}{D_o} \right)^{f} \right) \tag{4.3}$$

$$\mathrm{Nu}_{D,o} = 5 + 0.0317 \cdot \mathrm{Ra}_{D,o}^{*0.333} \cdot \left(\frac{\Delta y}{D_o} \right)^{0.344} \cdot \left(\frac{\Delta x}{D_o} \right)^{0.301} \tag{4.4}$$

Table 4.1: Range of applicability for each parameter in Equation 4.4

0	$\leq$	$Ra^*_{D,o}$	$\leq$	$6.0 \cdot 10^7$
1.3 in. (33 mm)	$\leq$	Δy	$\leq$	4.125 in. (105 mm)
1.3 in. (33 mm)	$\leq$	Δx	$\leq$	4.125 in. (105 mm)
1.05 in. (27 mm)	$\leq$	D_o	$\leq$	1.66 in. (42 mm)
0.85 in. (22 mm)	$\leq$	D_i	$\leq$	1.36 in. (36 mm)

L = 500 ft. (153 m)

Experimental vs. Correlated Nusselt Number Comparison

In order to validate Equation 4.4, the correlation was applied to the experimental data to check for consistency between the correlated results and the experimental

data. This was done by taking the experimental modified Rayleigh number and SWHE geometrical configuration and applying Equation 4.4 for each data point. The correlated and experimental Nusselt numbers can be seen in Figure 4.1. Also indicated in Figure 4.1, are the ±25% ±50% error bars, along with the unity line where correlated results vs. experimental data are equal.

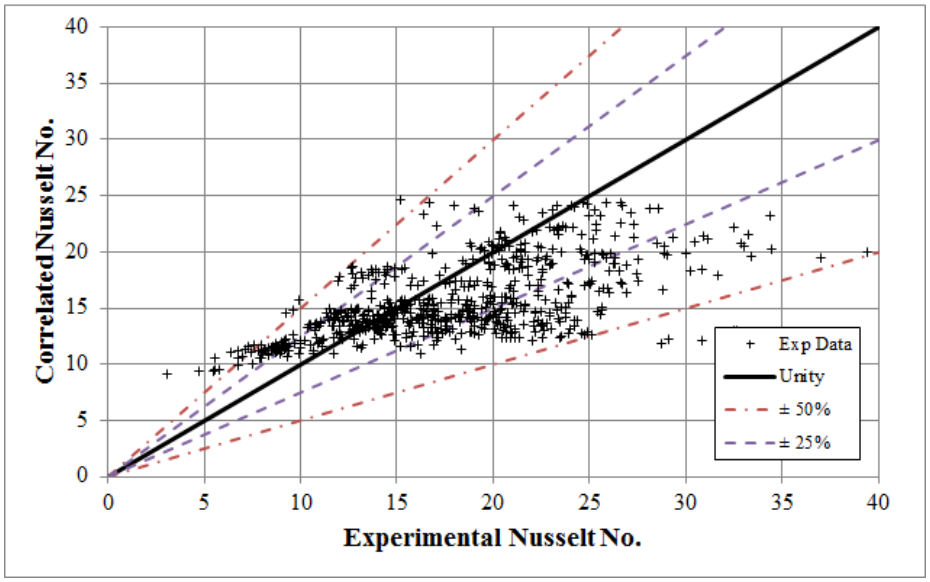

Figure 4.1: Pond heat rejection convection correlation simulated vs. experimental Nusselt number comparison

From Figure 4.1, we can see a significant amount of scatter in the data. To give a better indication of how well Equation 4.4 correlates to the experimental pond heat rejection data, a histogram plot of the percent error can be seen in Figure 4.2.

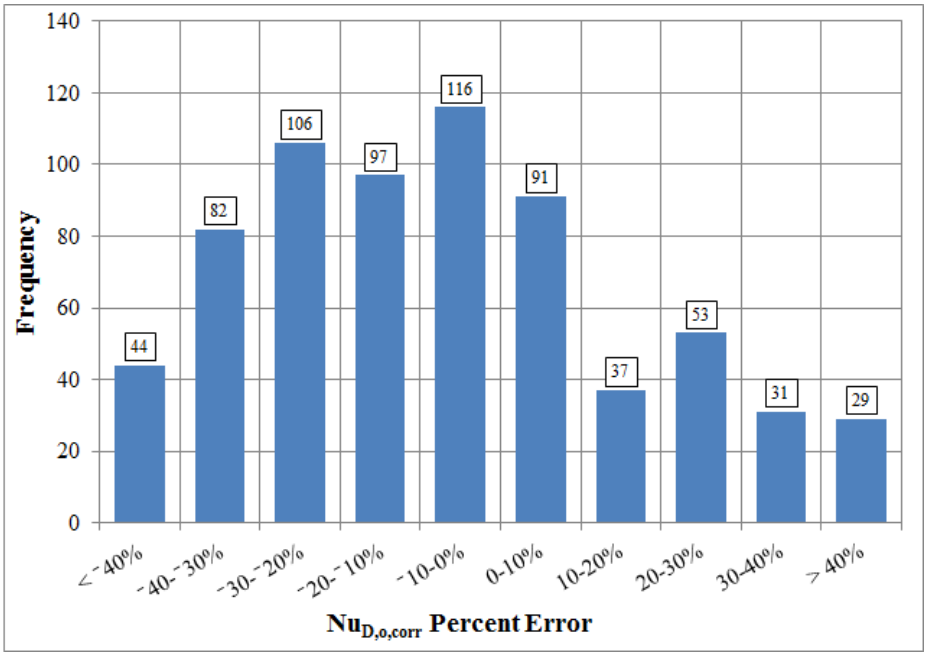

Figure 4.2: Pond heat rejection convection correlation histogram of simulated vs. experimental Nusselt number percent error

Here again, we can see that the percent error for most of the data set is scattered within ±40% of unity. This result is not ideal, but because the outside convective resistance only makes up a fraction of the total thermal resistance, heat transfer prediction results can still be reasonable.

Experimental vs. Simulated Heat Transfer Comparison

In order to compare Equation 4.4 based on how well heat transfer is predicted, a simulation was set up to compare the simulated heat transfer rate against the experimental heat transfer rate. To do this, the experimental entering fluid temperature, fluid flow rate, SHWE geometry, and surface water temperatures were all input into a model used to determine simulated SHWE heat transfer rate for that given experimental measurement. This model used Equation 4.4 as the correlation for determining the outside convective thermal resistance as well as the experimental circulating fluid inlet temperature, flow rate, and SWHE coil geometry as model inputs. A plot showing

the simulated and experimental heat transfer rates can be seen in Figure 4.3.

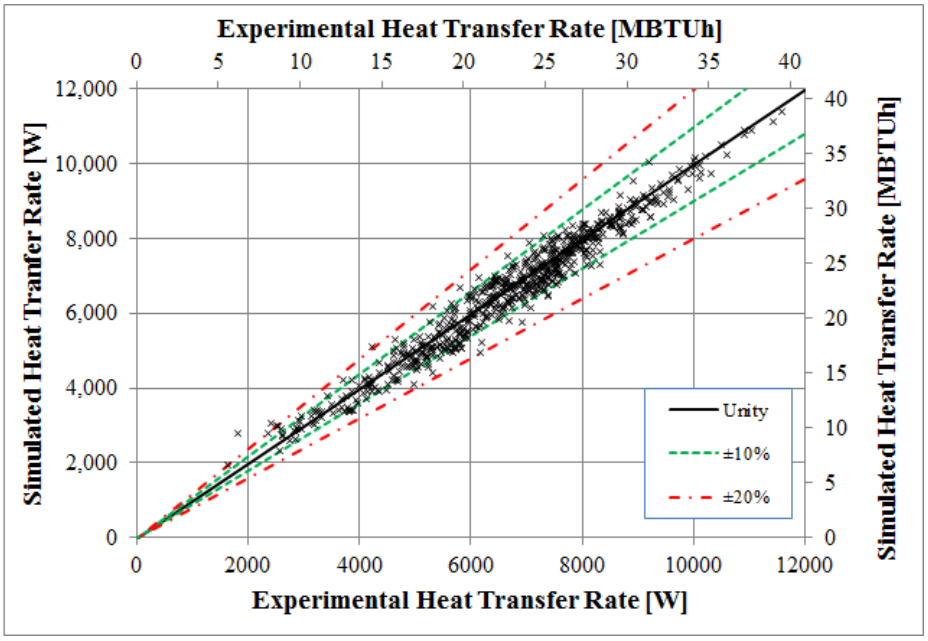

Figure 4.3: Pond heat rejection convection correlation simulated vs. experimental heat transfer rates

Here, we can see that despite the data scatter seen in Figure 4.1 for the correlated and experimental Nusselt numbers, the heat transfer rate can be predicted quite well. A histogram plot of the simulation vs. experimental heat transfer rates can be seen in Figure 4.4. From this plot, we can see that heat transfer percent error is centered around 0% error with most of the rest of the data within ±10% of the experimental data.

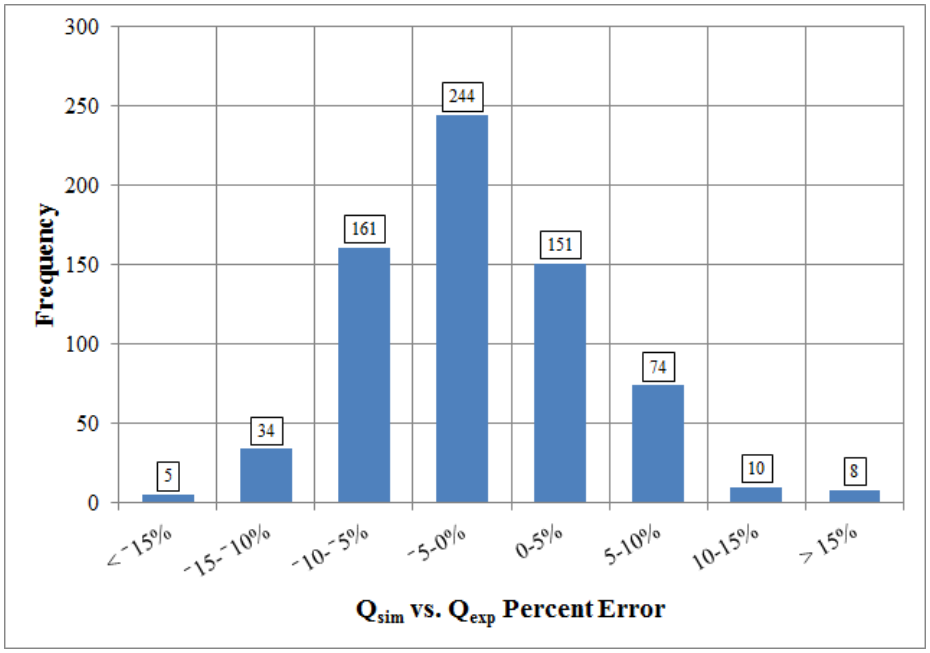

Figure 4.4: Pond heat rejection convection correlation simulated vs. experimental heat transfer rate percent error histogram

The reason for this behavior is given in Table 3.1 which shows the average thermal resistance of each thermal resistance component as a percentage of total thermal resistance. From this table we can see that the outside convection thermal resistance only makes up a relatively small portion of the total thermal resistance. On average across the three tube sizes tested, the outside thermal resistance makes up only 28% of the total thermal resistance. This implies that even given the ±40% differences in predicted Nusselt numbers, the total thermal resistance is only expected to be affected by around ±11%.

Table 4.2 summarizes the statistics for how well the Nusselt number and heat transfer results are predicted based on Equation 4.4. The key point to note is that despite the Nusselt number RMSE being approximately 27%, the heat transfer RMSE is considerably better at 6% due to what was just discussed.

Table 4.2: RMSE and MBE statistics for the pond heat rejection convection correlation

Nusselt Number		Heat Transfer Rate	
RMSE %	MBE %	RMSE %	MBE %
27.1	-6.5	6.3	-1.6

4.2.3 Pool Heat Rejection Data Convection Correlation

For this data set, the correlation described in Section 4.2.2 was taken as the base outside convection correlation. From the base case, this data set was taken and the correlation multiplier was optimized to provide the best fit to the data. It was observed that the data collected in the pool under heat rejection conditions tended to have Nusselt numbers which were much less than the data collected in the pond for the same SWHE geometry. Hence, the convection multiplier will cause the outside Nusselt number to be smaller than it would be if it were in the pond. The correlation developed for the pool heat rejection data can be seen in Equation 4.5.

$$\mathrm{Nu}_{D,o} = 0.573 \cdot \left(5 + 0.0317 \cdot \mathrm{Ra}_{D,o}^{*\,0.333} \cdot \left(\frac{\Delta y}{D_o} \right)^{0.344} \cdot \left(\frac{\Delta x}{D_o} \right)^{0.301} \right) \tag{4.5}$$

Experimental vs. Correlated Nusselt Number Comparison

Figure 4.5 below shows the correlated vs. experimental Nusselt number comparison plot. Error bars for ±10% and ±25% are show also shown. Figure 4.6 shows a histogram plot of the correlated vs. experimental percent error for Equation 4.5.

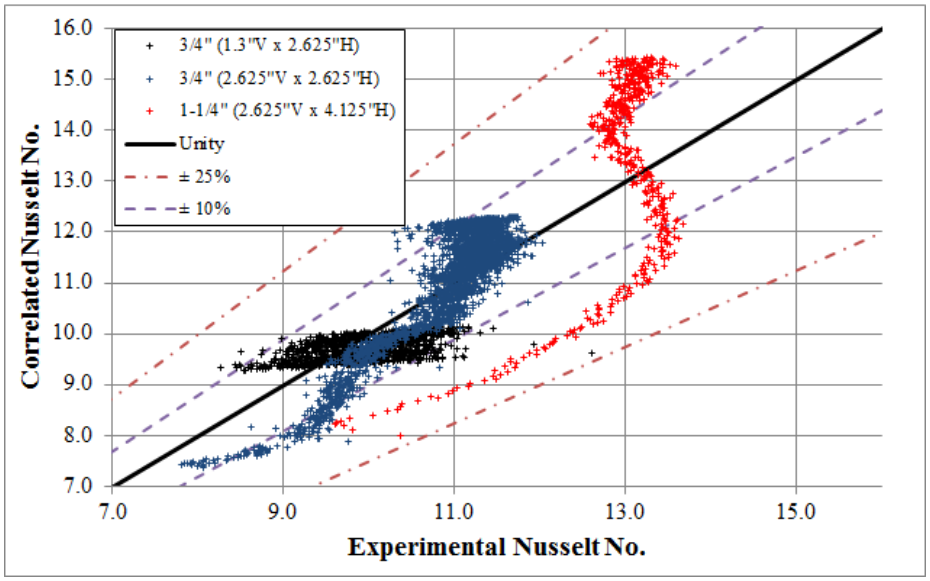

Figure 4.5: Pool heat rejection convection correlation simulated vs. experimental Nusselt number comparison

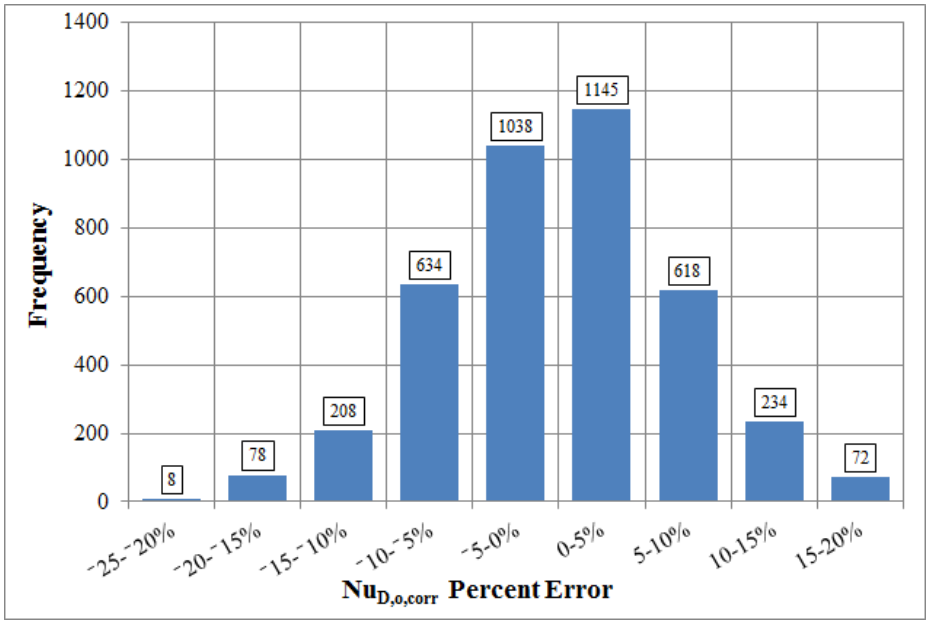

Figure 4.6: Pool heat rejection convection correlation simulated vs. experimental Nusselt number comparison histogram

From the two figures above we can see that the 3/4 in. (19 mm) data is predicted reasonably well by Equation 4.5. However, the 1-1/4 in. (32 mm) data shows trends

that are not captured by the convection correlation. The 1-1/4 in. (32 mm) data tends to be under predicted by the convection correlation in the lower range of Nusselt numbers, then over predicted at higher Nusselt numbers. The reason for this can be observed in Figure 3.5, where the experimental Nusselt number increases, as expected with increasing Rayleigh number. However, something begins occurring at $Ra_D^* = 3.5 \cdot 10^7$ when the Nusselt numbers begin decreasing with increases in Rayleigh numbers. The reason for this non-monotonic behavior is not fully understood, but the author theorizes that it is due to the constrained nature of the pool in which the experiments were performed.

Experimental vs. Simulated Heat Transfer Comparison

Comparing the heat transfer results for the pool heat rejection data, we can again see that the correlation shown in Equation 4.5 predicts the heat transfer reasonably well. Figure 4.7 shows the simulated vs. experimental heat transfer rate comparison, and Figure 4.8 shows the histogram of the simulated vs. experimental percent error.

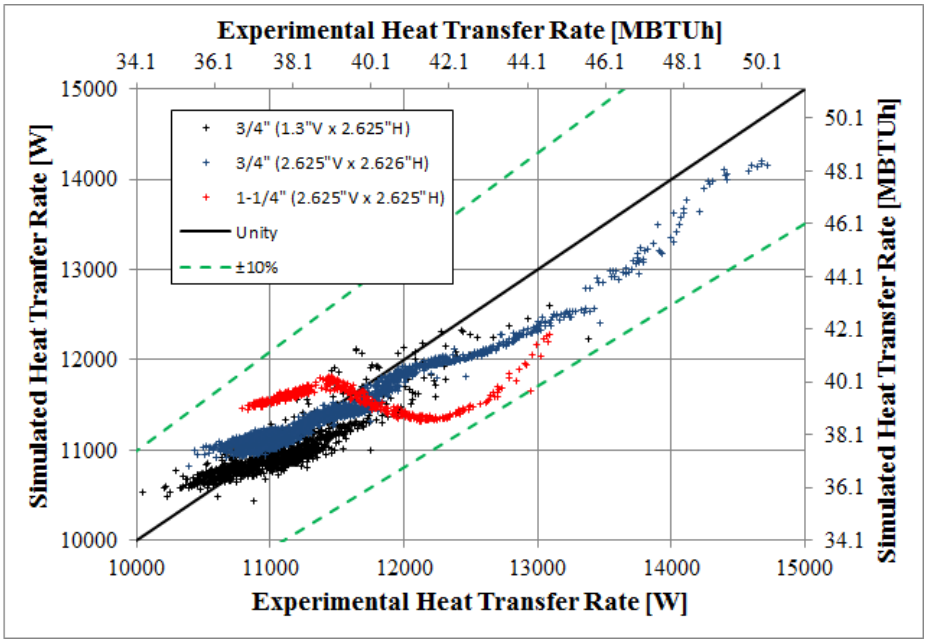

Figure 4.7: Pool heat rejection convection correlation simulated vs. experimental heat transfer rates

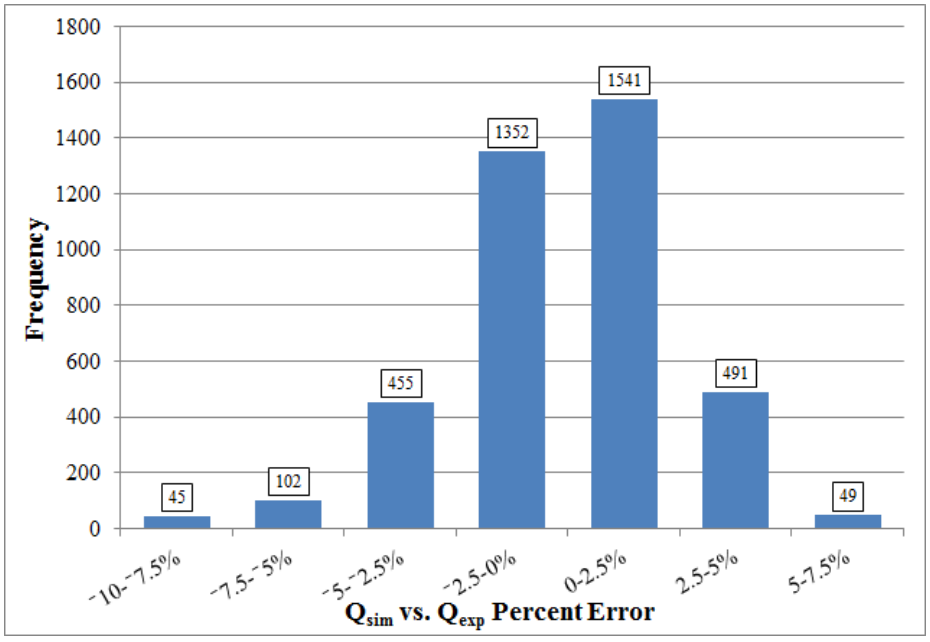

Figure 4.8: Pool heat rejection convection correlation simulated vs. experimental heat transfer rate histogram of percent error

From these figures, we can see that using Equation 4.5 to predict the outside

convection resistance correlates nearly all of the experimental data within ±10%. For the given data, this is sightly better than the results for the pond heat rejection.

Table 4.3 shows the summary of statisitcs to quantify how well Equation 4.5 predicts the outside convection resistance for the pool heat rejection data.

Table 4.3: RMSE and MBE statistics for the pool heat rejection convection correlation

Nusselt Number		Heat Transfer Rate	
RMSE %	MBE %	RMSE %	MBE %
6.9	0.0	2.5	-0.1

4.2.4 Heat Rejection Convection Correlation Comparison

To compare the two correlations described above, the correlations were compared against experimental data for each data set. Due to the limited number of overlapping geometrical configurations, the 3/4 in. (19 mm) 2.625 in. H x 2.625 in. V (67 mm x 67 mm) data was selected for comparison purposes. Figure 4.9 shows the experimental data, and the convection correlations for the specific SWHE geometry plotted together. From the figure, we can see that the Nusselt number for the pool data is considerably lower than the pond data. This is reflected in the pool convection correlation.

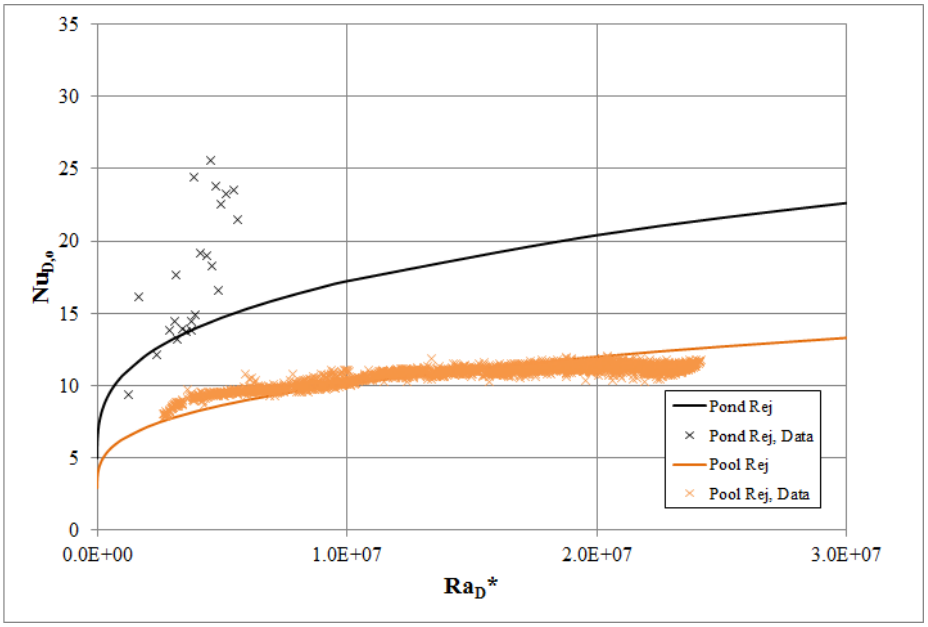

Figure 4.9: Heat rejection convection correlation Nusselt number comparison

4.2.5 Pool Heat Extraction Data Convection Correlation

Because the pool heat extraction data was selected as the base data set for heat extraction, the base convection correlation will be developed in this section. As a continuation of the discussion in Section 3.3.2, the heat extraction data is very sensitive near the surface water maximum density point. This was described previously regarding the trends shown when the convective plume flow direction changes from downward flow to upward flow.

Figure 4.10 below show the data from Figures 3.10, 3.11, and 3.12 combined into a single figure. In order to organize the data and distinguish between the data which likely to have downward flow vs. data that is likely to have upward flow, the Rayleigh number was multiplied by the flow direction scalar δ based on the conditions indicated in Table 4.4. A positive δ indicates downward plume flow, while a negative δ indicates an upward plume flow. This data can be seen in Figure 4.11 where δ is multiplied by the modified Rayleigh number.

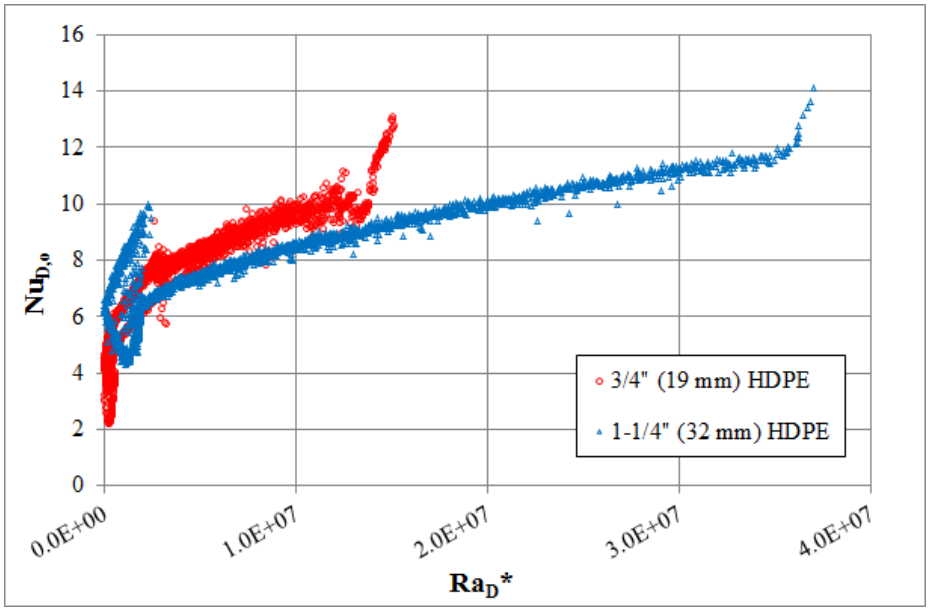

Figure 4.10: Nusselt vs. modified Rayleigh number plot of combined pool heat extraction data

Table 4.4: Flow direction scalar

$$\delta = \begin{cases} 1 \text{ if:} & \rho_{sw-T,film,o} < \rho_{sw-T,sw} \\ -1 \text{ if:} & \rho_{sw-T,film,o} > \rho_{sw-T,sw} \end{cases}$$

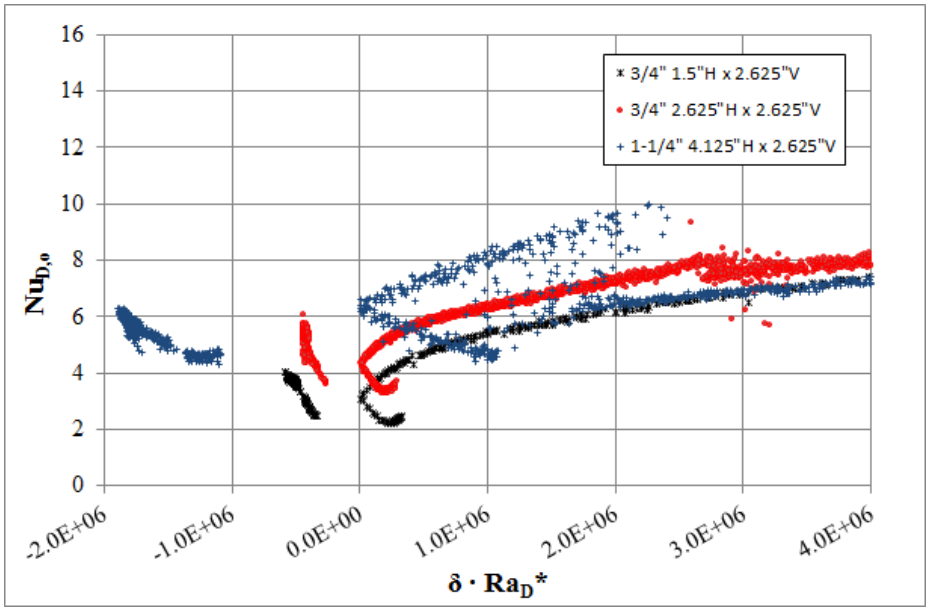

Figure 4.11: Nusselt vs. flow direction modified Rayleigh number plot of combined pool heat extraction data with flow direction scalar

In Figure 4.11 we see some of the data near the lowest Nusselt number that has been reflected about $Ra_D^* = 0$ by the flow direction scalar. For the 3/4 in. (19 mm) data, the data affected by this flow direction change go from $Ra_D^* = 0$ to approximately $Ra_D^* = 5 \cdot 10^5$. The 1-1/4 in. (32 mm) data is affected from $Ra_D^* = 0$ up to approximately $Ra_D^* = 2 \cdot 10^6$, however, there is still some scatter in the data above $Ra_D^* = 2 \cdot 10^6$.

Because the data has been shown to be very sensitive near the surface water maximum density point, it is very difficult to accurately correlate the data in this region. As is the case with the 1-1/4 in. (32 mm) data, and as will be shown in the next section for the 3/4 in. (19 mm) pond heat extraction data, Nusselt number experimental data taken in this region can give randomized results. As a result of this sensitivity, the data for the 3/4 in. (19 mm) below $Ra_D^* = 1 \cdot 10^6$ and the 1-1/4 in. (32 mm) data below $Ra_D^* = 3 \cdot 10^6$ have been omitted from use in the correlation development. Below these points, due to the highly random data, a constant Nusselt

number value will be recommended.

Equation 4.6 is the equation that was optimized to fit the pool heat extraction base data set. The correlation's range of applicability can be seen below in Table 4.5.

$$\mathrm{Nu}_{D,o} = 0.87 \cdot \left(5.75 + 0.00971 \cdot \mathrm{Ra}_{D,o}^{*\,0.333} \cdot \left(\frac{\Delta y}{D_o} \right)^{0.929} \right) \tag{4.6}$$

Table 4.5: Range of applicability for each parameter in Equation 4.6

$1.0 \cdot 10^6$	$\leq$	$Ra^*_{D,o}$	$\leq$	$4.0 \cdot 10^7$
1.3 in. (33 mm)	$\leq$	Δy	$\leq$	2.625 in. (67 mm)
2.625 in. (67 mm)	$\leq$	Δx	$\leq$	4.125 in. (105 mm)
1.05 in. (27 mm)	$\leq$	D_o	$\leq$	1.66 in. (42 mm)
0.85 in. (22 mm)	$\leq$	D_i	$\leq$	1.36 in. (36 mm)
L = 500 ft. (153 m)				

For values of Ra^*_D less than $1 \cdot 10^6$ for 3/4 in. (19 mm) pipes, and Ra^*_D less than $3 \cdot 10^6$ for 1-1/4 in. (32 mm) pipes, a constant value of $Nu_{D,o} = 5$ is used. This number represents a mean value for Nusselt number which can be expected in this range of Rayleigh numbers.

Experimental vs. Correlated Nusselt Number Comparison

Figure 4.12 shows the experimental vs. correlated Nusselt number comparison for this data set. Figure 4.13 shows the histogram plot of the experimental vs. correlated Nusselt number percent error. The histogram shows that the percent error is skewed left into negative percent errors. This indicates that the correlation is under predicting the experimental results to a certain degree.

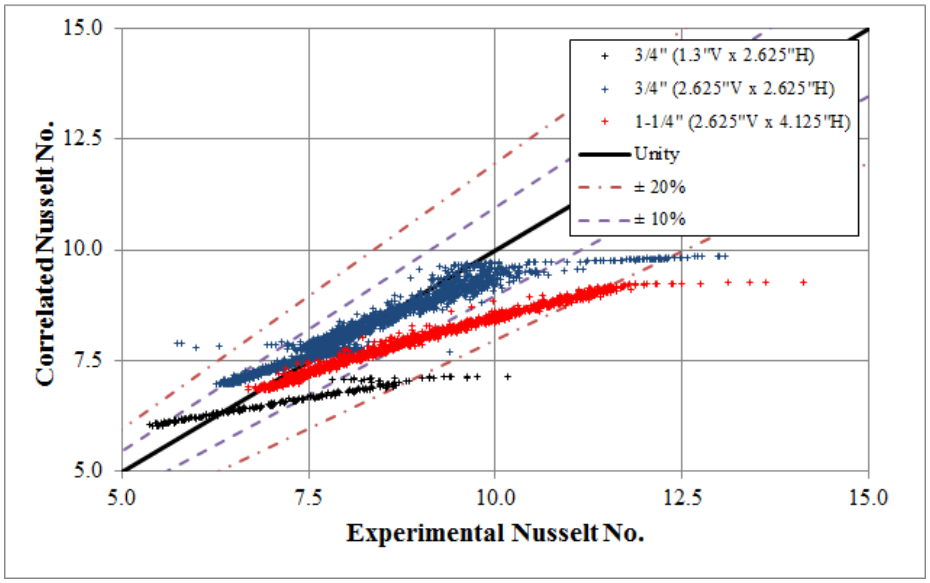

Figure 4.12: Pool heat extraction convection correlation simulated vs. experimental Nusselt number comparison

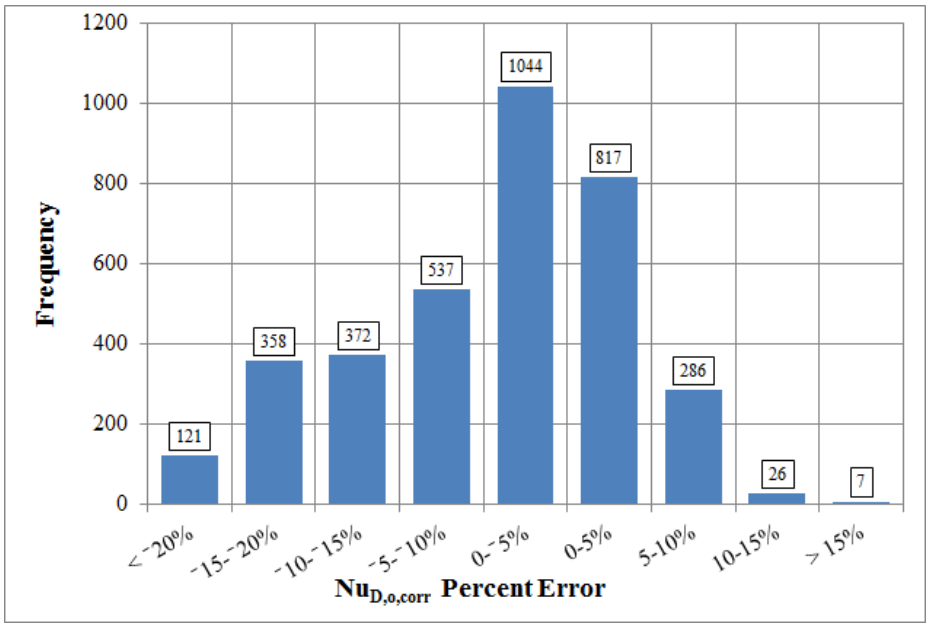

Figure 4.13: Pool heat extraction convection correlation histogram of simulated vs. experimental Nusselt number percent error

In Figure 4.12 we can see towards the right side of each data set that there is a small band of data that trails off away from the rest of the data. This small band

of trailing data is data that was recorded during the initial startup period of the experiments. This data was recorded during the time when initial systems transients were still settling.

Another trend worth noting is the fact that both 3/4 in. (19 mm) data sets are mostly centered around the 'unity' line. This implies that over the range data, the correlation will predict Nusselt number values that will be centered around the actual value. However, for the 1-1/4 in. data, the correlation tends to under predict the Nusselt number by around 0-20% over the range of experimental data. The reason for this is currently unknown.

Experimental vs. Simulated Heat Transfer Comparison

Figure 4.14 shows the simulated vs. experimental heat transfer rate comparison for pool heat extraction data set using Equation 4.6 as the outside convection correlation. Figure 4.15 shows the histogram plot of the percent error between the experimental and simulated results.

We can see that the 3/4 in. (19 mm) 2.625 in. V x 2.625 in. H (67 mm x 67 mm) results tend to be similar to the Nusselt number results shown in Figure 4.12. The other two data sets, however, tend to have the magnitude of the heat transfer under predicted by up to 10%. This occurs due to the outside Nusselt number being incorrectly predicted by Equation 4.6. Even given this, heat transfer is predicted reasonably well at lower heat transfer rates. At higher heat transfer rates, the simulated heat transfer rate deviates from the experimental value by up to 10%.

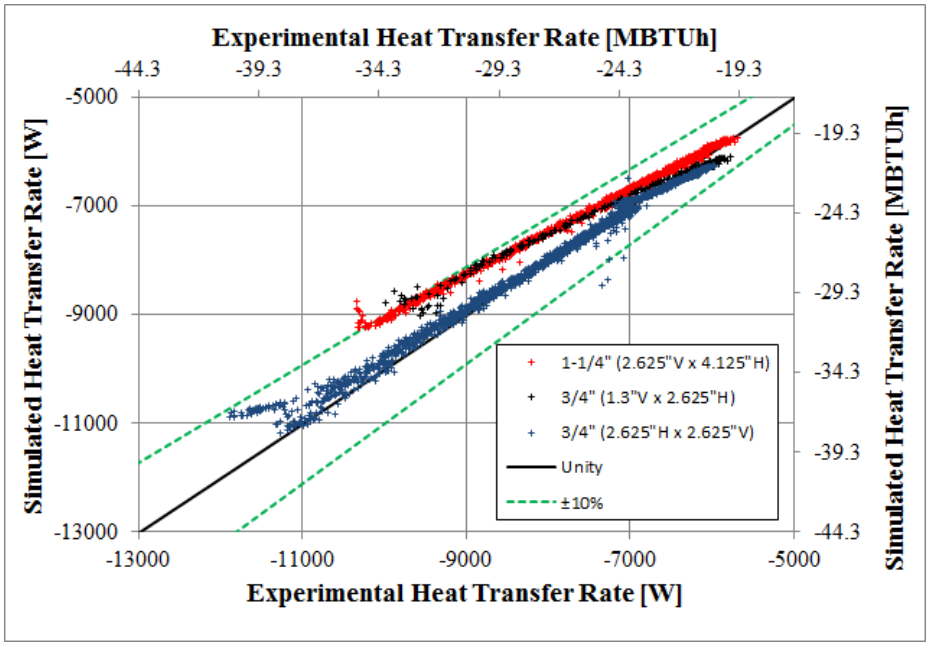

Figure 4.14: Pool heat extraction convection correlation simulated vs. experimental heat transfer rates

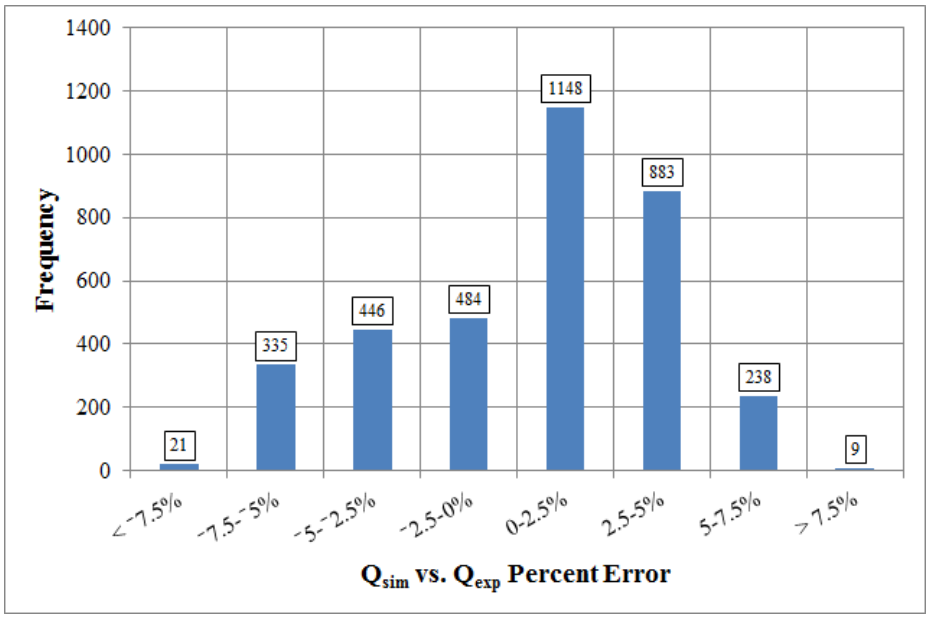

Figure 4.15: Pool heat extraction convection correlation simulated vs. experimental heat transfer rate histogram of percent error

Table 4.6 shows the statistical measures used to quantify how well the correlation

predicts Nusselt number, and how how well the simulation, using Equation 4.6 to predict outside Nusselt number, predicts heat transfer rate.

Table 4.6: RMSE and MBE statistics for the pool heat extraction convection correlation

Nusselt Number		Heat Transfer Rate	
RMSE %	MBE %	RMSE %	MBE %
9.1	-4.5	4.1	-2.0

4.2.6 Pond Heat Extraction Data Convection Correlation

To show the sensitivity of the pond heat extraction data near the surface water maximum density point, the flow direction scalar as shown in Table 4.4 is again applied to this data set. This can be seen Figure 4.16 where data from $Ra_D^* = 0$ to $Ra_D^* = 1 \cdot 10^6$ is reflected about $Ra_D^* = 0$.

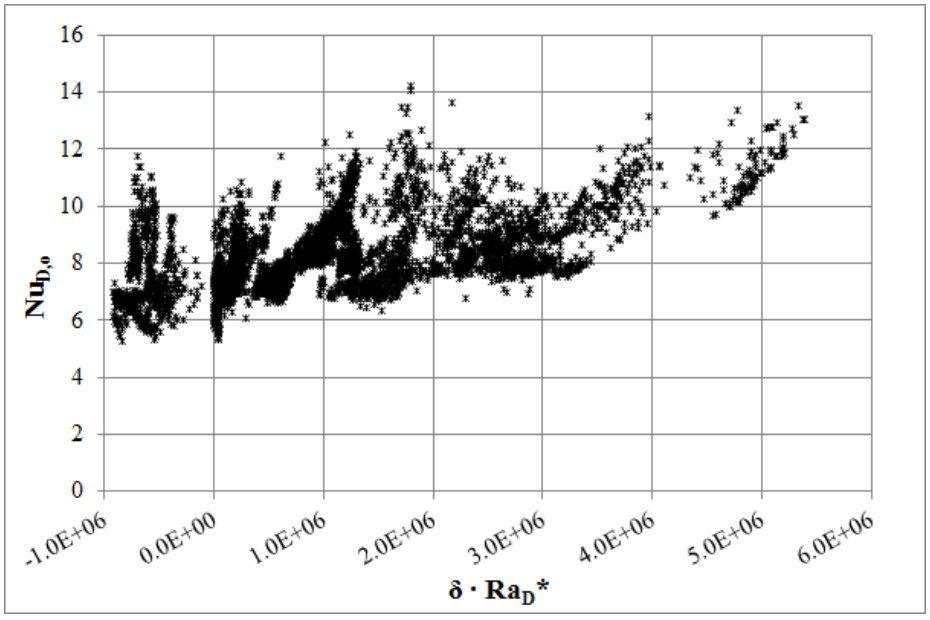

Figure 4.16: Nusselt vs. modified Rayleigh number plot of combined pond heat extraction data with flow direction scalar

As was the case with the previous data set, this data shows highly random and

data near the maximum density point. As a result of this, the data from $Ra^*_D = 0$ to $Ra^*_D = 1 \cdot 10^6$ is not used in the development of the convection correlation.

Because this is the alternative data set for heat extraction, the correlation developed in the previous section will be used for the pond heat extraction data correlation. Because the pool data tended to under predict the pond data during heat extraction conditions, the multiplier was optimized to scale the correlation shown in Equation 4.6 up to best fit the pond heat extraction data. Equation 4.7 below shows this correlation.

$$\mathrm{Nu}_{D,o} = 5.75 + 0.00971 \cdot \mathrm{Ra}^{*\,0.333}_{D,o} \cdot \left(\frac{\Delta y}{D_o}\right)^{0.929} \tag{4.7}$$

Experimental vs. Correlated Nusselt Number Comparison

Figure 4.17 shows the correlated vs. experimental Nusselt number comparison plot for the pond heat extraction data as correlated by Equation 4.7. Also shown are the $\pm 10\%$ and $\pm 25\%$ error bars. From the plot, it is obvious that there are conditions occurring in the experiment which were not accounted for the correlation. This experiment was performed outdoors in a pond which was exposed to the weather elements. Some theoretical possibilities for conditions affecting the data are wind or underwater currents. Wave action causing the support platform to move excessively could also have caused the convective boundary layers to be disturbed, thus giving the effect of lower outside convective resistance. These are all theoretical possibilities, however, the actual reason for the discrepancy is unknown at this time. By comparison, a similar behavior was observed for the pond heat rejection data in Figure 4.1.

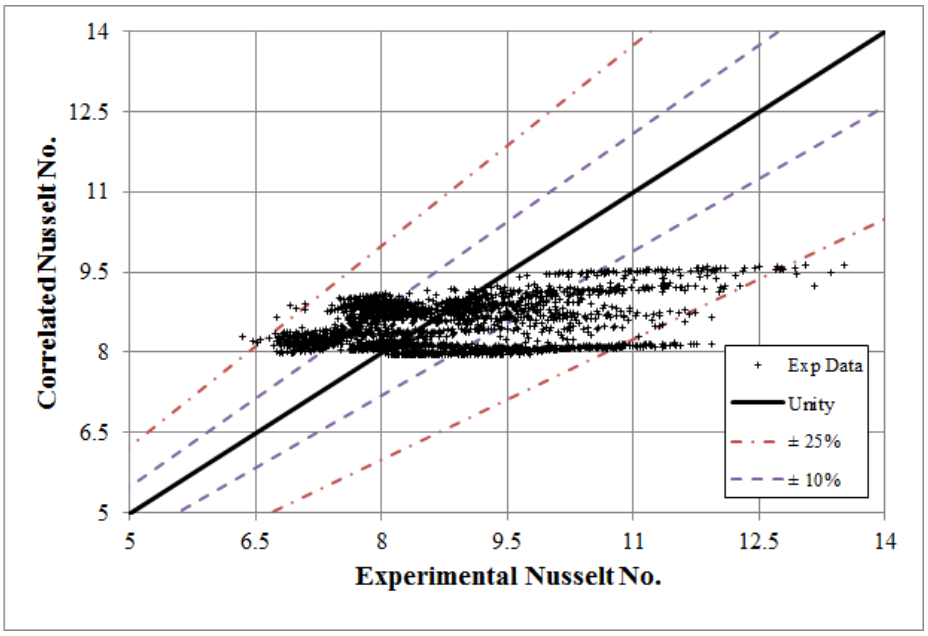

Figure 4.17: Pond heat extraction convection correlation simulated vs. experimental Nusselt number comparison

Figure 4.20 shows a histogram plot of correlated vs. experimental Nusselt number percent error. From this we see that at the very least, the data is centered around the 0% error with error mostly bounded with in ±30% error. The result is not ideal, but over the range of data, the correlated Nusselt numbers will be centered around the experimental data.

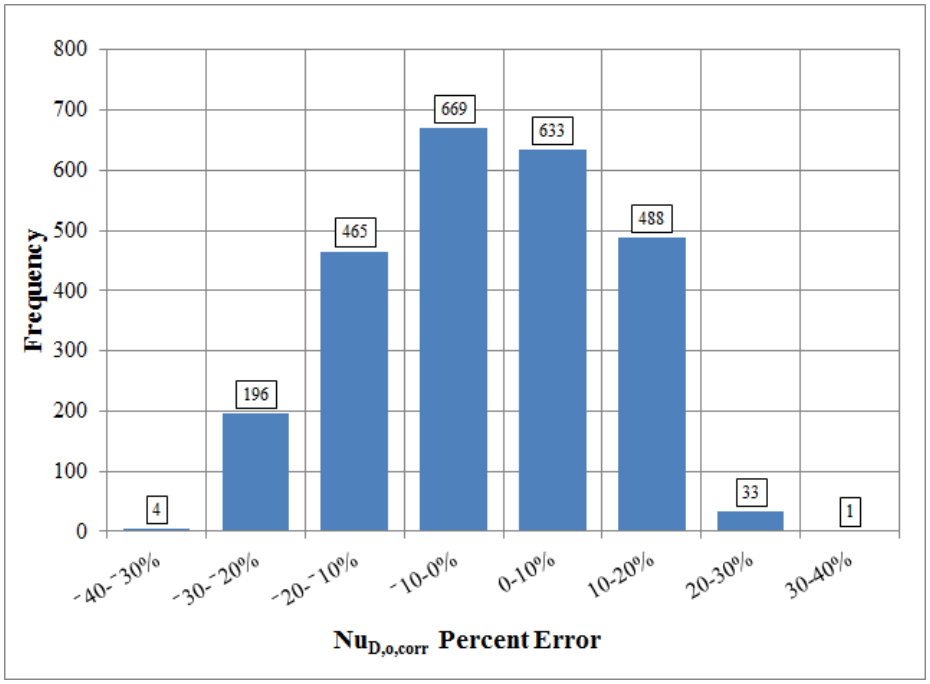

Figure 4.18: Pond heat extraction convection correlation simulated vs. experimental Nusselt number comparison histogram

Experimental vs. Simulated Heat Transfer Comparison

Figure 4.19 shows how well the simulation using the correlation described in Equation 4.7 for the outside Nusselt number predicts the SWHE heat transfer rate. Figure 4.20 shows a histogram plot of the heat transfer rate percent error. Here again we see that although the Nusselt number is not correlated perfectly, the heat transfer rates are nearly all predicted to within 10% of experimental data.

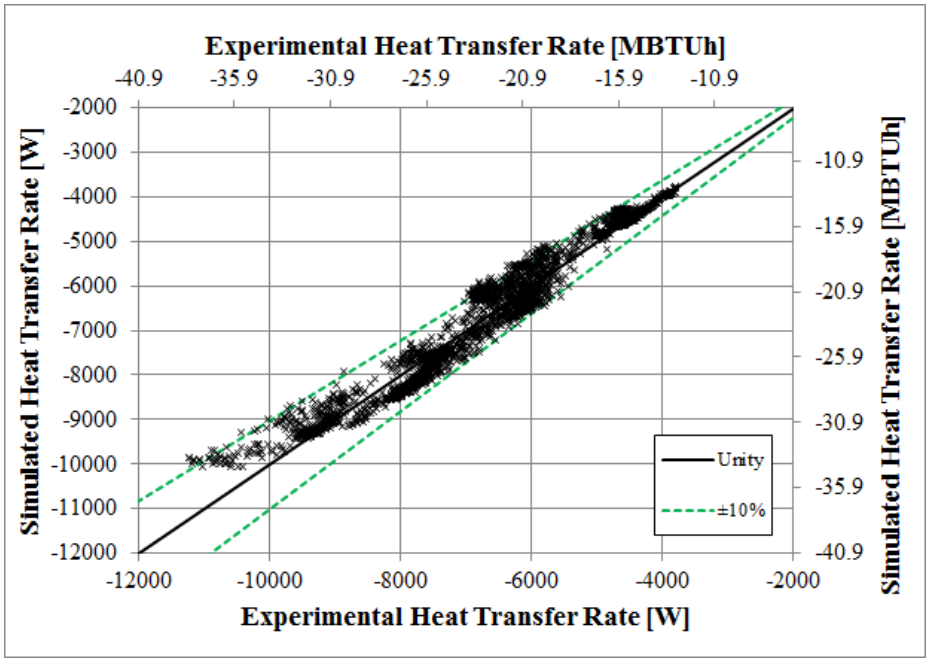

Figure 4.19: Pond heat extraction convection correlation simulated vs. experimental heat transfer rates

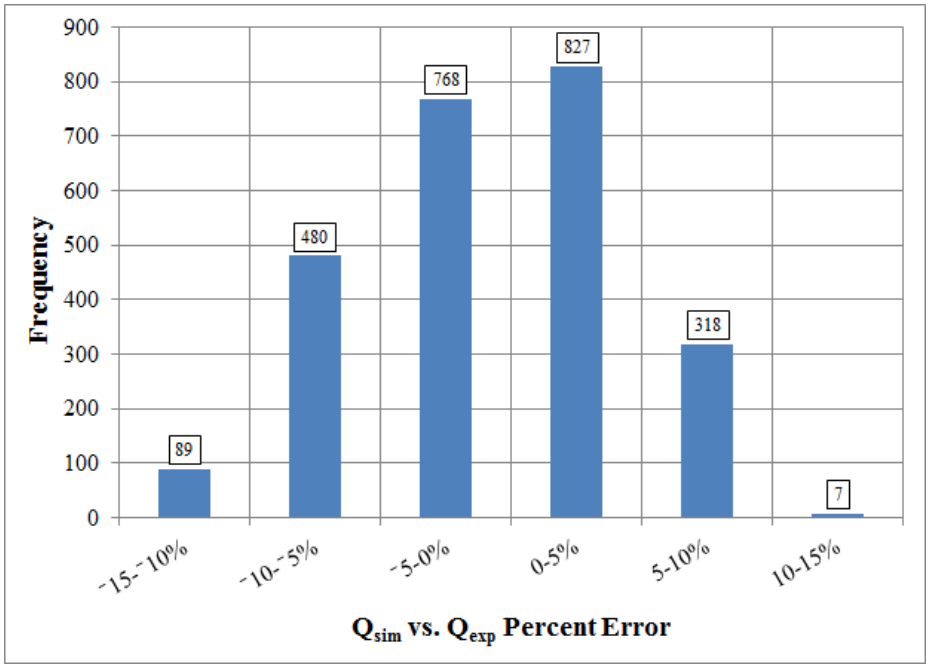

Figure 4.20: Pond heat extraction convection correlation simulated vs. experimental heat transfer rate histogram of percent error

Table 4.7 shows the RMSE and MBE statistics to quantify how well Equation 4.7 predicts the Nusselt number and heat transfer rates of the pond heat extraction data.

Table 4.7: RMSE and MBE statistics for the pond heat extraction convection correlation

Nusselt Number		Heat Transfer Rate	
RMSE %	MBE %	RMSE %	MBE %
12.2	-1.8	5.0	-0.8

4.2.7 Heat Extraction Convection Correlation Comparison

To compare the two correlations described above for heat extraction, the correlations were compared against experimental data for each data set. Again, due to the limited number of overlapping geometrical configurations, the 3/4 in. (19 mm) 2.625 in. H x 2.625 in. V (67 mm x 67 mm) data was selected for comparison purposes. Figure 4.21 shows the experimental data, and the convection correlations for the specific SWHE geometry plotted together. From the figure, we can see that the Nusselt number for the pool data is lower than the data from the pond.

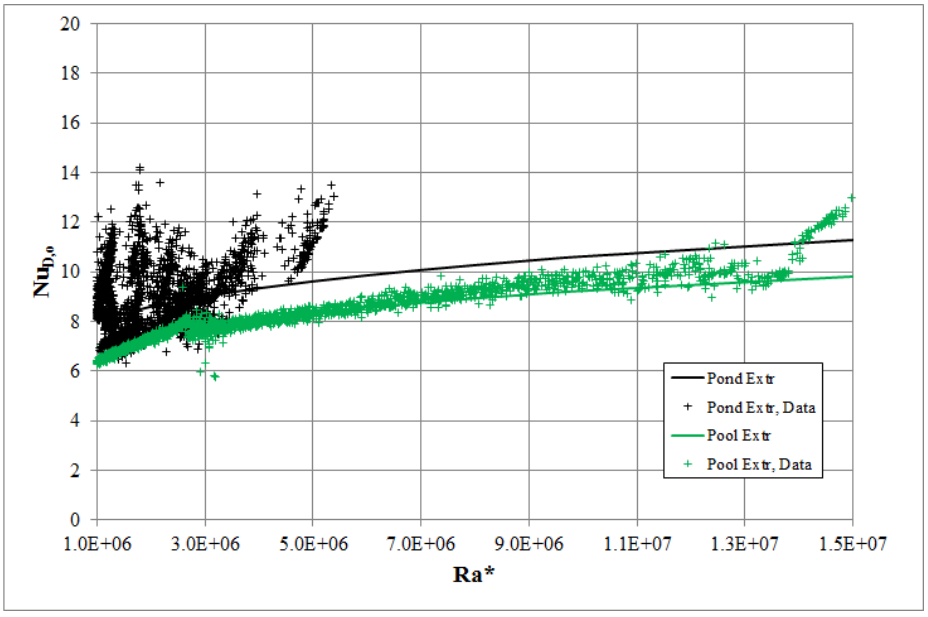

Figure 4.21: Heat extraction convection correlation Nusselt number comparison

4.3 Churchill-Chu Correlation Comparison

Up until this point, there have been no comparisons of the convection correlation derived in this work against standard correlations for straight pipes, which is what has been used for surface water heat exhangers prior to this work (Chiasson 1999). In this section, the experimental data is compared against the Churchill & Chu (1975) correlation for free convection from a horizontal cylinder. The results are compared and a summarized to give the reader another means whereby to compare the current work.

4.3.1 Pond Heat Rejection Data Comparison

For the pond heat rejection data, some benefits are realized when comparing the Nusselt number RMSE and MBE. For the Churchill & Chu (1975) correlation, RMSE percent error was 41.9% for the Churchill & Chu (1975) correlation vs. the 27.1% for the correlation presented during this work. MBE is however, slightly better going to -5.0% for the Churchill & Chu (1975) correlation vs. -6.5% for the present correlation. Figure 4.22 shows the Nusselt number as calculated by the Churchill & Chu (1975) correlation against the experimentally derived pond heat rejection Nusselt numbers. Figure 4.1 can be compared for reference to the current correlation.

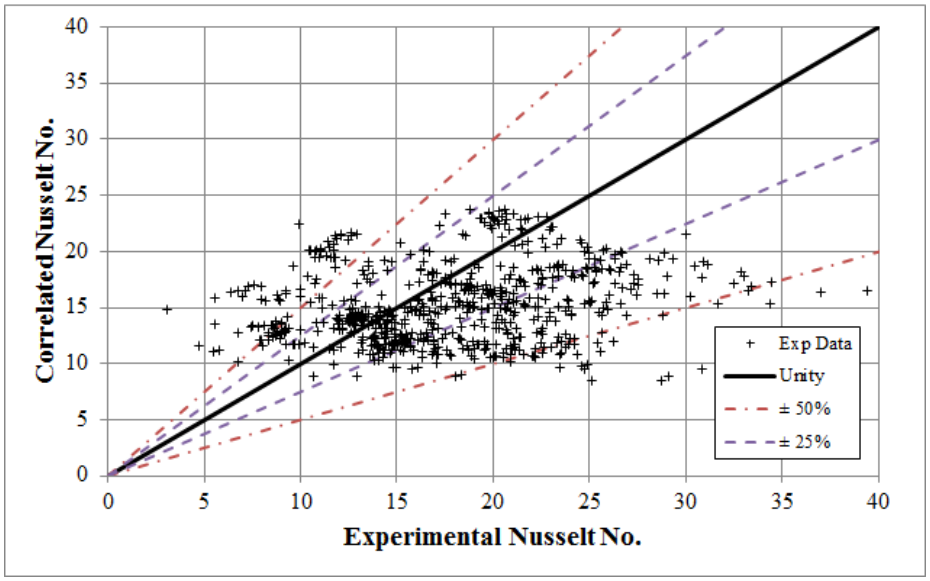

Figure 4.22: Nusselt number comparison for the Churchill-Chu correlation vs. experimental pond heat rejection data

The difference in Nusselt number has a much smaller effect on heat transfer when the Churchill & Chu (1975) correlation is used in a simulation to calculate the heat transfer rates. For the Churchill & Chu (1975) correlation, RMSE percent error was 7.1% when by comparison the correlation presented during this work had an RMSE percent error of 6.3%. Figure 4.23 show the heat transfer results for the simulation vs. the experimentally derived pond heat rejection data. For comparison, Figure 4.3 can be referenced for comparison of the correlation presented in this work.

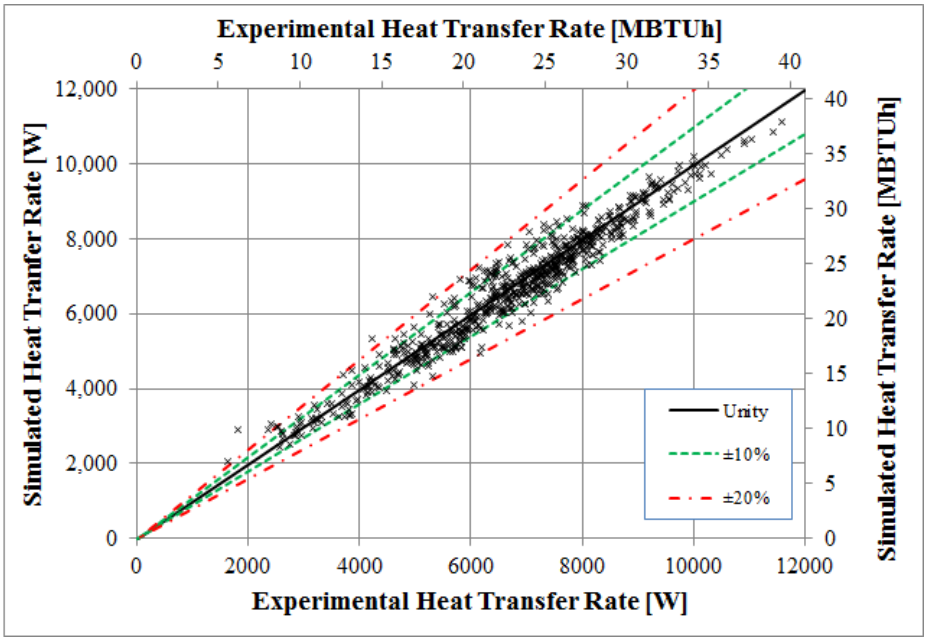

Figure 4.23: Heat transfer rate comparison for the Churchill-Chu correlation vs. experimental pond heat rejection data

4.3.2 Pool Heat Rejection Data Comparison

For the pool heat rejection data, the benefits of the current work are much more pronounced when compared to the Churchill & Chu (1975) convection correlation. Figure 4.24 shows the Nusselt number comparison for the Churchill & Chu (1975) correlation vs. the experimentally derived pool heat rejection data. The reader may reference Figure 4.5 for the Nusselt number correlation from the present work. The correlation by Churchill & Chu (1975) showed a Nusselt number RMSE percent error of 92.6% whereas the current correlation showed a 6.9% error for the same data.

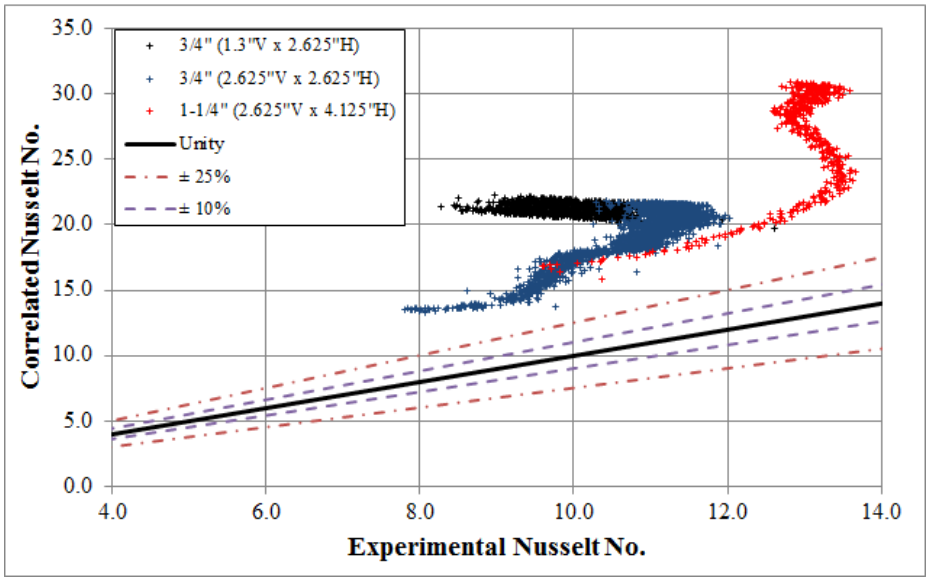

Figure 4.24: Nusselt number comparison for the Churchill-Chu correlation vs. experimental pool heat rejection data

Figure 4.25 shows the heat transfer comparison results when the Churchill & Chu (1975) correlation is utilized in the simulated comparison of the experimental data. The reader can refer to Figure 4.7 for comparison against the current work. For this case, the RMSE percent error for the heat transfer error is 15.4% whereas the correlation presented in this work is 2.5%. We can also see that the correlation over predicts Nusselt number, which is reflected in the over prediction of the heat transfer results.

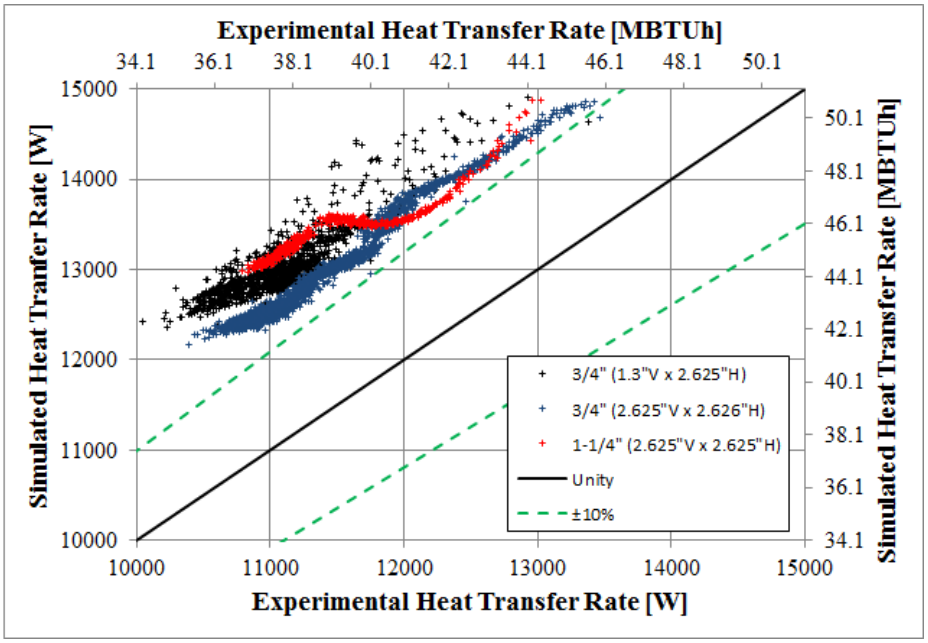

Figure 4.25: Heat transfer rate comparison for the Churchill-Chu correlation vs. experimental pool heat rejection data

4.3.3 Pond Heat Extraction Data Comparison

For the pond heat extraction data, we can see that the Churchill & Chu (1975) correlation tends to again over predict the Nusselt number. This can be seen in Figure 4.26. Figure 4.17 can also be referenced by the reader to compare against the Nusselt number predictions for the current correlation. For the Churchill & Chu (1975) correlation, the RMSE percent error is 44.9% whereas for the correlation developed in this work, the RMSE percent error is 12.2%.

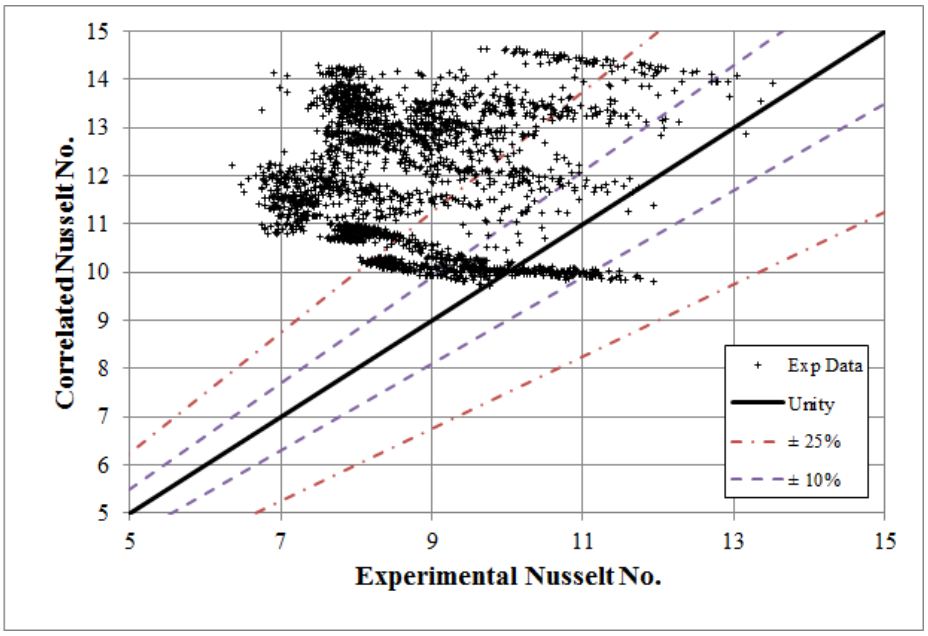

Figure 4.26: Nusselt number comparison for the Churchill-Chu correlation vs. experimental pond heat extraction data

The discrepancy in Nusselt number over prediction is reflected again in the simulated heat transfer comparison results. Figure 4.27 shows the heat transfer comparison against the pond heat extraction data. Figure 4.19 can also be referenced for comparison against the correlation presented in this work. For the Churchill & Chu (1975) correlation, the RMSE percent error is 11.8% whereas for the current correlation same error is 5.0%.

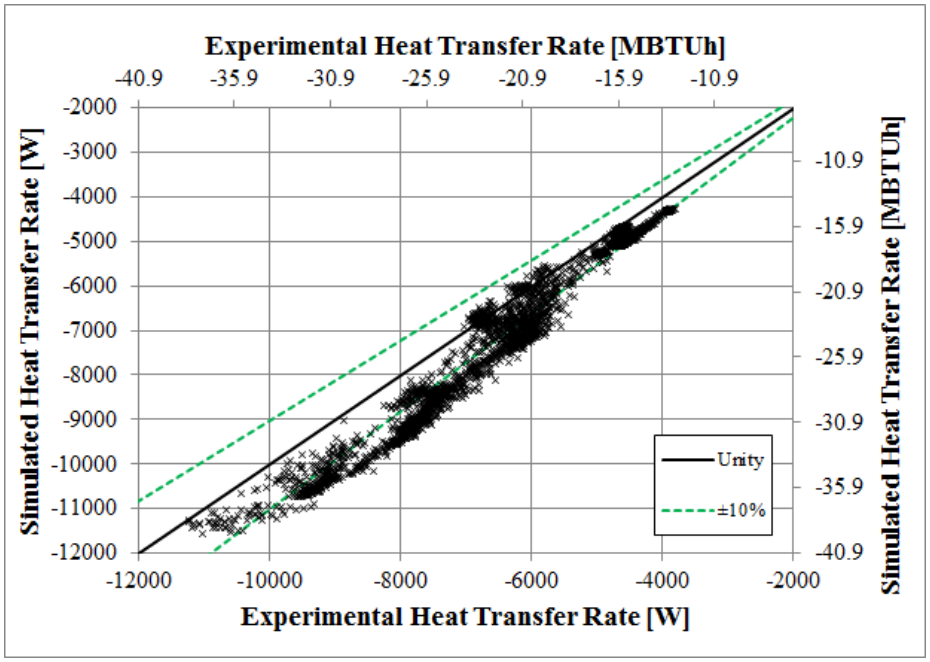

Figure 4.27: Heat transfer rate comparison for the Churchill-Chu correlation vs. experimental pond heat extraction data

4.3.4 Pool Heat Extraction Data Comparison

For the pool heat extraction data, we again see that the Churchill & Chu (1975) correlation over predicts the experimental data. This can be seen in Figure 4.28. Figure 4.12 can be referenced for comparison to the current convection correlation. The Nusselt number RMSE percent error for the Churchill & Chu (1975) correlation is 99.6% whereas the same error for the current correlation is 9.1%.

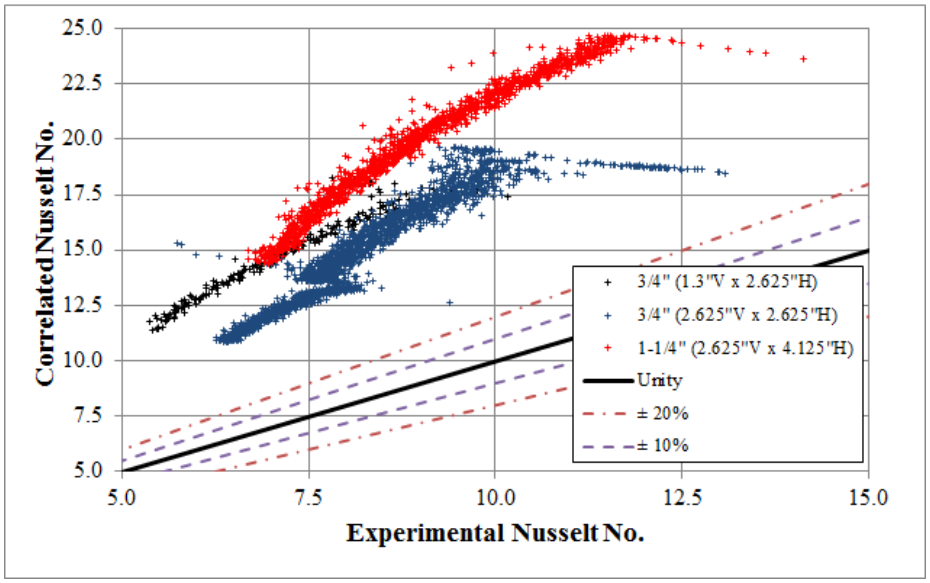

Figure 4.28: Nusselt number comparison for the Churchill-Chu correlation vs. experimental pool heat extraction data

Figure 4.29 shows the simulated heat transfer comparison for the Churchill & Chu (1975) correlation. By comparison, Figure 4.14 can be referenced for the heat transfer comparison against the current correlation. The heat transfer RMSE percent error for the Churchill & Chu (1975) correlation is 21.6% whereas the same error for the current correlation is 4.1%.

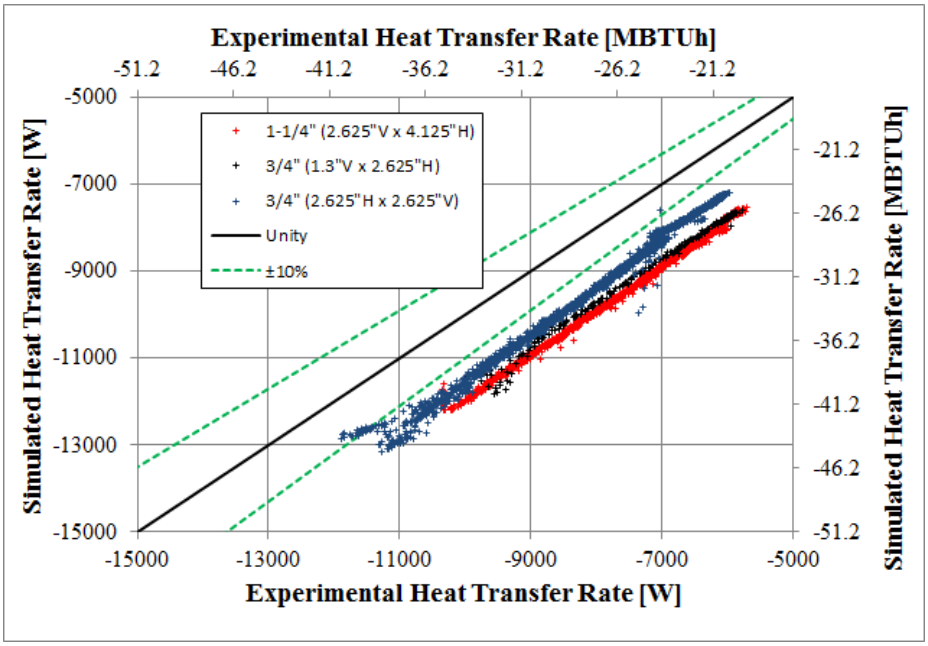

Figure 4.29: Heat transfer rate comparison for the Churchill-Chu correlation vs. experimental pool heat extraction data

4.3.5 Churchill-Chu Correlation Summary

From the previous results, we can see that the correlation presented in this work better predicts the Nusselt number and heat transfer rates when compared to the Churchill & Chu (1975) convection correlation, which is what has been used up until this work. Table 4.8 can be referenced to also to compare the current correlation against the Churchill & Chu (1975) convection correlation.

4.4 Conclusions

In this chapter, convection correlations have been developed for spiral-helical surface water heat exchangers. These correlations were developed from experimental data taken in a pond and pool in heat rejection and heat extraction modes of operation. The correlations have been shown to predict outside Nusselt number to within an RMSE value of 28% for heat rejection cases, and within 13% for heat extraction

Table 4.8: RMSE and MBE statistics for Nusselt number and heat transfer rate for the Churchill & Chu (1975) convection correlation

	Nusselt Number		Heat Transfer Rate	
	RMSE %	MBE %	RMSE %	MBE %
	Mitchell/Churchill-Chu			
Pond HR	27.1/41.9	-6.5/-5.0	6.3/7.1	-1.6/-1.2
Quiescent HR	6.9/92.6	0.0/90.2	2.5/15.4	-0.1/15.2
Pond HE	12.2/44.9	-1.8/38.4	5.0/11.8	-0.8/10.3
Quiescent HE	9.1/99.6	-4.5/97.4	4.1/21.6	-2.0/21.0

cases. When the correlations were implemented in a simulation, heat transfer rates were shown to be predicted to with 7% RMSE for heat rejection cases, and within 5% RMSE for heat extraction cases.

Revisited below is Equation 4.3, which is the general form of the correlation proposed in this chapter. Also shown below is Table 4.9 where the correlation coefficients are summarized for the different SWHE operating conditions. Correlations labeled as quiescent are recommended for use in situations where the surface water body is shallow or the SWHE would by some other means be constrained. An example of this would be a situation where the pond level has dropped over the course of a hot summer to where the water level is very near the SWHE level. This would be expected to cause convective resistance to increase and system performance to decrease.

$$\mathrm{Nu}_{D,o} = a \cdot \left(b + c \cdot \mathrm{Ra}_{D,o}^{*\,d} \cdot \left(\frac{\Delta y}{D_o} \right)^{e} \cdot \left(\frac{\Delta x}{D_o} \right)^{f} \right) \qquad \text{(4.3 revisited)}$$

Below, two tables are shown which give the range of applicability for each parameter in the outside convection correlation. Table 4.10 shows the range of applicability for the heat rejection mode of operation, while Table 4.11 shows the range of applicability for the heat extraction mode of operation.

In the heat extraction mode of operation below $Ra_D^* = 1 \cdot 10^6$, a constant Nusselt number of 5 should be applied. This is to account for the sensitivity of experimental

Table 4.9: Convection coefficient summary

Condition	a	b	c	d	e	f
Pond HR	1	5	0.0317	0.333	0.344	0.301
Quiescent HR	0.573	5	0.0317	0.333	0.344	0.301
Pond HE	1	5.75	0.00971	0.333	0.929	0
Quiescent HE	0.87	5.75	0.00971	0.333	0.929	0

Table 4.10: Range of applicability for heat rejection convection correlation

$$
\begin{array}{rcccl}
0 & \leq & Ra^*_{D,o} & \leq & 6.0 \cdot 10^7 \\
\text{1.3 in. (33 mm)} & \leq & \Delta y & \leq & \text{4.125 in. (105 mm)} \\
\text{1.3 in. (33 mm)} & \leq & \Delta x & \leq & \text{4.125 in. (105 mm)} \\
\text{1.05 in. (27 mm)} & \leq & D_o & \leq & \text{1.66 in. (42 mm)} \\
\text{0.85 in. (22 mm)} & \leq & D_i & \leq & \text{1.36 in. (36 mm)}
\end{array}
$$

L = 500 ft. (153 m)

Table 4.11: Range of applicability for heat extraction convection correlation

$$
\begin{array}{rcccl}
1.0 \cdot 10^6 & \leq & Ra^*_{D,o} & \leq & 4.0 \cdot 10^7 \\
\text{1.3 in. (33 mm)} & \leq & \Delta y & \leq & \text{2.625 in. (67 mm)} \\
\text{2.625 in. (67 mm)} & \leq & \Delta x & \leq & \text{4.125 in. (105 mm)} \\
\text{1.05 in. (27 mm)} & \leq & D_o & \leq & \text{1.66 in. (42 mm)} \\
\text{0.85 in. (22 mm)} & \leq & D_i & \leq & \text{1.36 in. (36 mm)}
\end{array}
$$

L = 500 ft. (153 m)

data in this region due to the maximum density point of the surface water.

CHAPTER 5

DESIGN TOOLS

In this chapter, tools are developed to aid in SWHP system design. In the following sections, handbook style design diagrams for space heating and space cooling are developed which are based on the experimentally derived heat transfer correlations described in Chapter 4.

5.1 Design Graph Derivation

To develop the diagrams, a simulation was developed using the previously developed outside convection correlations. In the simulation the zone load was fixed at 1 ton (3,517 W) for the case of space cooling and at 12 MBTUh (3,517 W) for the case of space heating. Other parameters such as tube size, coil geometry, circulating fluid, fluid flow rate, lake temperature, heat pump COP, tube material, tube schedule, tube fouling resistance, and surface water characteristics were also held constant for each individual case. Then, to generate the diagrams, a range of coil entering fluid temperatures were input into the model. From this, the model determined the coil length required to meet the zone load. This method allowed the zone heat transfer rate per required length of coil to be determined, which could then be plotted against approach temperature. Approach temperature is defined as the temperature difference between the coil exiting fluid temperature and the lake temperature.

5.2 Space Cooling Design Graphs

In this section design diagrams for space cooling are given. The design diagrams give the required installed pipe length for the given design conditions plotted against the approach temperature difference. For all design diagrams, the various design options are compared against the "typical" case. This case is defined as a mid-way point between what is being called the "best-case" and "worst-case" designs. Here, "best" case is used to describe the set of SWHP system and SWHE parameters that are most favorable to SWHE performance within the context of these design diagrams. The "worst" case is used to describe the SWHP and SWHE system parameters that are least favorable to system performance.

Figure 5.1 shows the required pipe length plotted against approach temperature for the "typical," "best," and "worst" HDPE design cases. Table 5.1 shows the SWHP systems and SWHE parameters that are fixed for each respective case. Heat pump COP is constant and based on the average COP from four separate off-the-shelf water-air heat pumps with a capacity from 1-3 tons at the expected heat pump entering fluid temperatures. "Best" and "worst" case surface water temperatures were taken from the high and low values from the isotherm plots obtained from Selvakumar (2013), respectively. Later, we will explain why the 95°F (35°C) lake temperature was selected as the "best" case and why the 50°F (10°C) lake was selected as the "worst" case. The rest of the parameters outlined in Table 5.1 will be given more discussion later in the section.

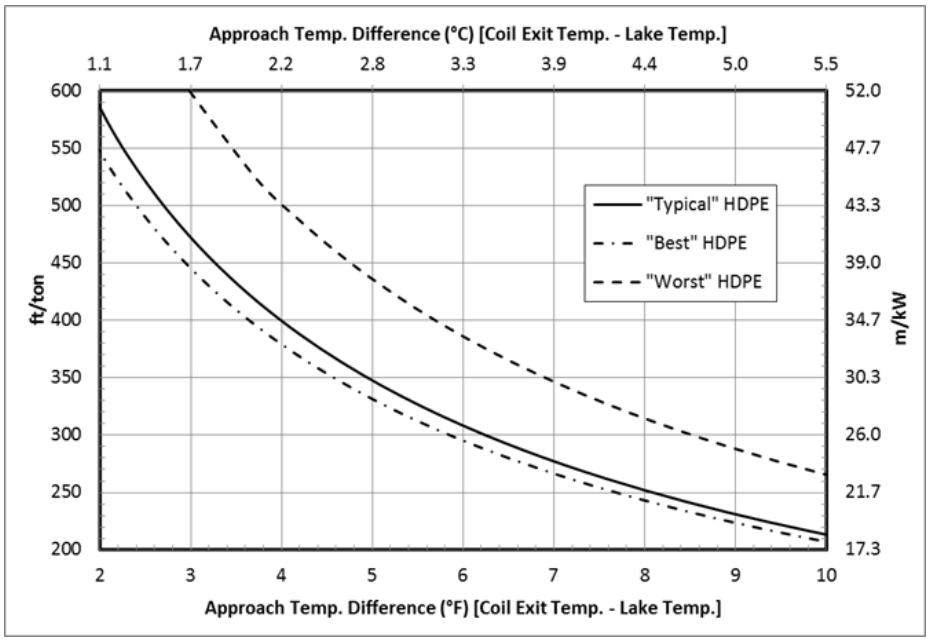

Figure 5.1: "Best" and "worst" case HDPE design diagram

Table 5.1: Parameters for the "best" and "worst" cases

	"Typical" HDPE	"Best" HDPE	"Worst" HDPE
HP COP_h	4	2.9	5.5
Lake Temp	70°F (21.1°C)	95°F (35°C)	50°F (10°C)
Vert. Spacing	2.625 in. (67 mm)	4.125 in. (105 mm)	1.3 in. (33 mm)
Horiz. Spacing	2.625 in. (67 mm)	4.125 in. (105 mm)	1.3 in. (33 mm)
Tube Size	1 in. (25 mm)	1-1/4 in. (32 mm)	3/4 in. (19 mm)
Tube Schedule	SDR-11		
Tube Material	HDPE PE 3408		
Flow Rate	3 gpm (11.4 L/min)		
Space Cooling	1 ton (3,517 W)		
Circ. Fluid	12.5% PG	Water	25% PG
Ext. Fouling	None	None	0.00053 hr-ft^2-°F/BTU 0.003 m^2-°C/W
Int. Fouling	None	None	0.000175 hr-ft^2-°F/BTU 0.001 m^2-°C/W
Surface Water Charachteristics	Pond	Pond	Pond

Figure 5.2 shows the percent error between the "typical" HDPE case and the

"best" and "worst" cases. The "typical" HDPE case is taken as the base case. From this figure, we can see that the percent difference between the "typical" and "best" case ranges from 4-8%. This means that at 4-8% reduction in installed SWHE length per ton (3,517 W) of space cooling could be achieved if the "best" method were applied. A 24% increase in installed SWHE length is required if the "worst" practice is applied.

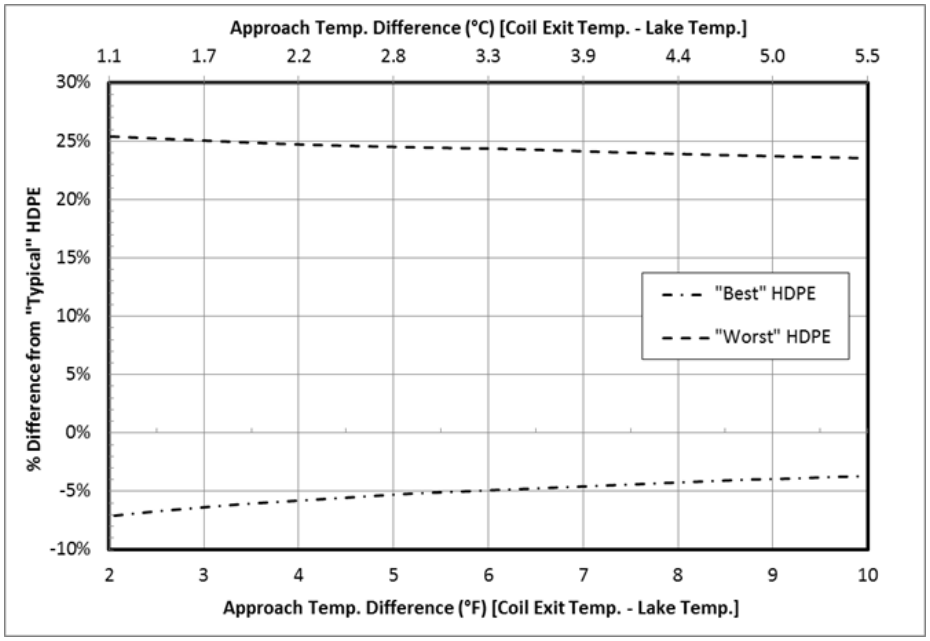

Figure 5.2: "Best" and "worst" case HDPE design diagram percent error

Figure 5.3 shows the "typical," "best," and "worst" cases for copper SWHEs. All parameters shown in Table 5.1, with the exception of the tube material, are identical for this copper SWHE design diagram. Figure 5.4 shows the percent difference from the "typcial" copper case similar to what was described previously for the HDPE SWHEs.

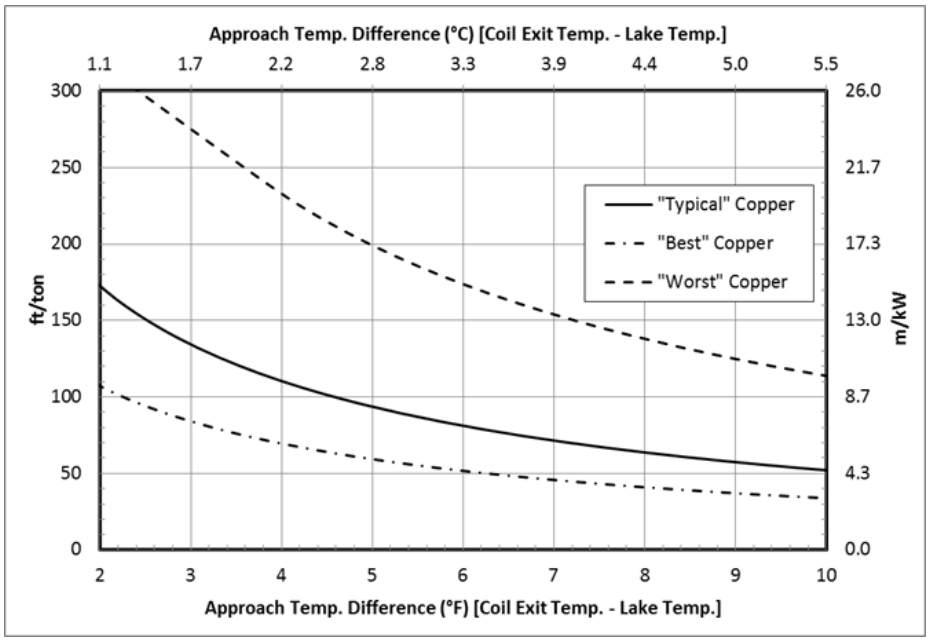

Figure 5.3: "Best-case" and "worst-case" copper SWHE design diagram

For Figure 5.4 we see that changing to the "best" case parameters for the copper SHWE could result in a 40% reduction in required SWHE tube length. However, for the "worst" case, an increase of 105-118% would be required. The copper SHWE is much more sensitive to the various cases because the pipe conduction resistance is no longer the dominate thermal resistance. For HDPE SWHEs, the pipe thermal resistance often makes up nearly half of the total thermal resistance, whereas for copper SWHEs, the pipe conduction resistance is negligible.

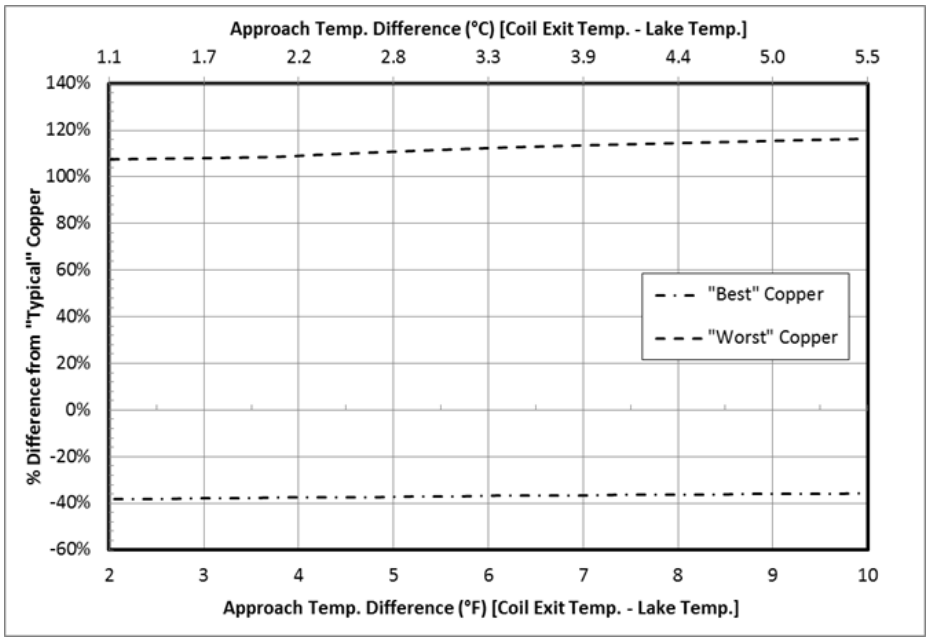

Figure 5.4: "Best-case" and "worst-case" copper SWHE design diagram percent error

From Figures 5.1 and 5.3 we have established our "typical" HDPE and copper cases. These will be the base cases for comparison purposes throughout the remainder of this section.

In Figure 5.5, variations in required pipe length due to variations in heat pump COP can be seen. From the figure, we see that for space cooling applications, lower heat pump COPs will require longer installed pipe lengths for a fixed zone load. The reverse is also true in that higher COPs will require less installed pipe. A drop in heat pump COP signifies a decrease in heat pump efficiency, i.e. more work is required for a constant output and more compressor heat must be rejected. This decrease in efficiency is reflected in the design diagrams by an increase in required pipe length.

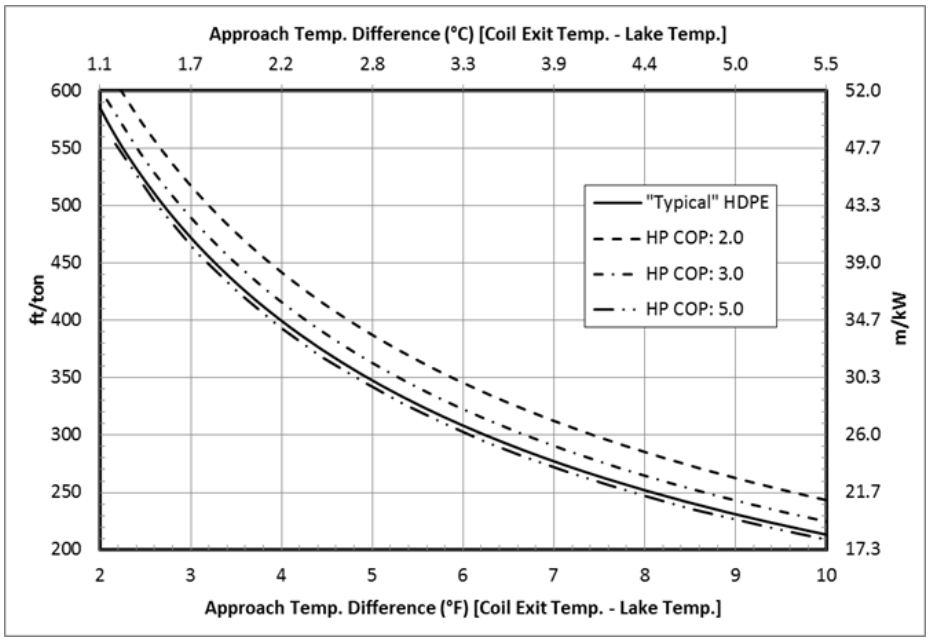

Figure 5.5: Heat pump COP design diagram

Figure 5.6 shows the percent error between the "typical" case and the different fixed heat pump COP cases. From the "typical" case which was a fixed heat pump COP of 4.0, selecting a heat pump with a COP of 2.0 will require a 7-13% increase in installed pipe length to meet the same cooling load. For the heat pump with a fixed COP of 3.0, an increase in installed pipe of about 2-4% should be implimented. Selecting a more efficient heat pump with a COP of 5.0, a decrease in required pipe length of 2-3% can be realized.

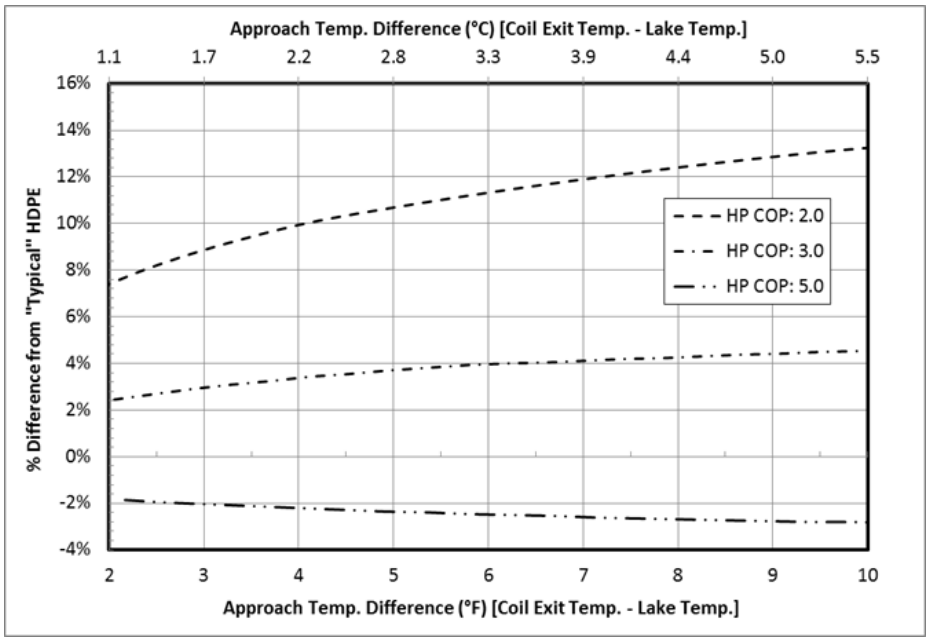

Figure 5.6: Heat pump COP design diagram percent error

Figure 5.7 shows how varying the pipe size on the "typical" HDPE case affects coil sizing. All parameters are identical to the "typical" HDPE case with the exception of the nominal pipe diameter as indicated in the figure. Figure 5.8 shows the percent difference between the "typical" case and the cases with 3/4 in. (19 mm) and 1-1/4 in. (32 mm) pipe sizes.

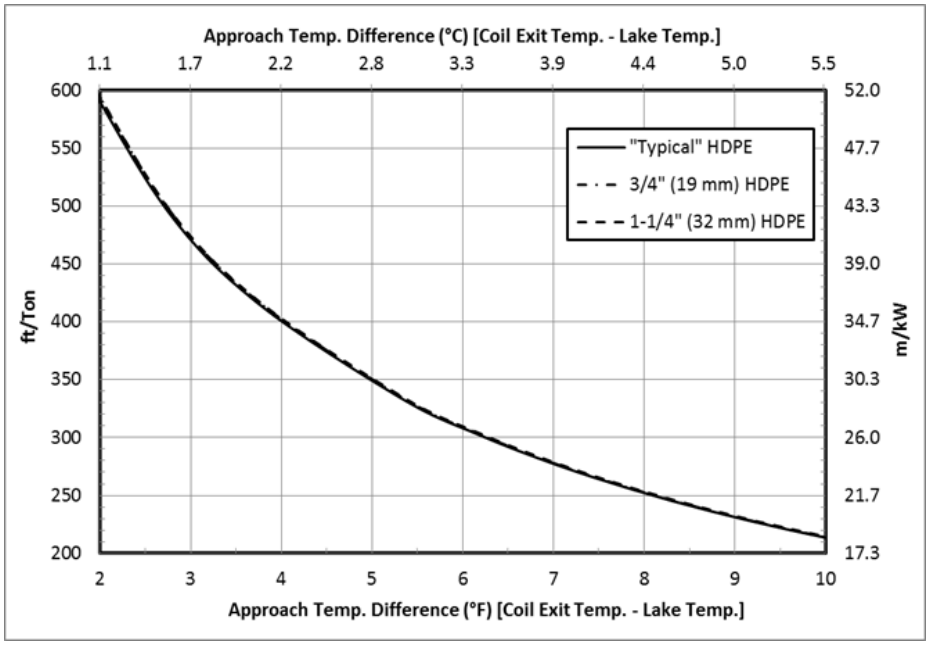

Figure 5.7: Pipe size design diagram

From Figure 5.7, we can see that changing the nominal pipe diameter has a very small influence on heat exchanger sizing when compared to the base case. Nominal differences across the range of approach temperatures are minimal which can be seen in Figure 5.8.

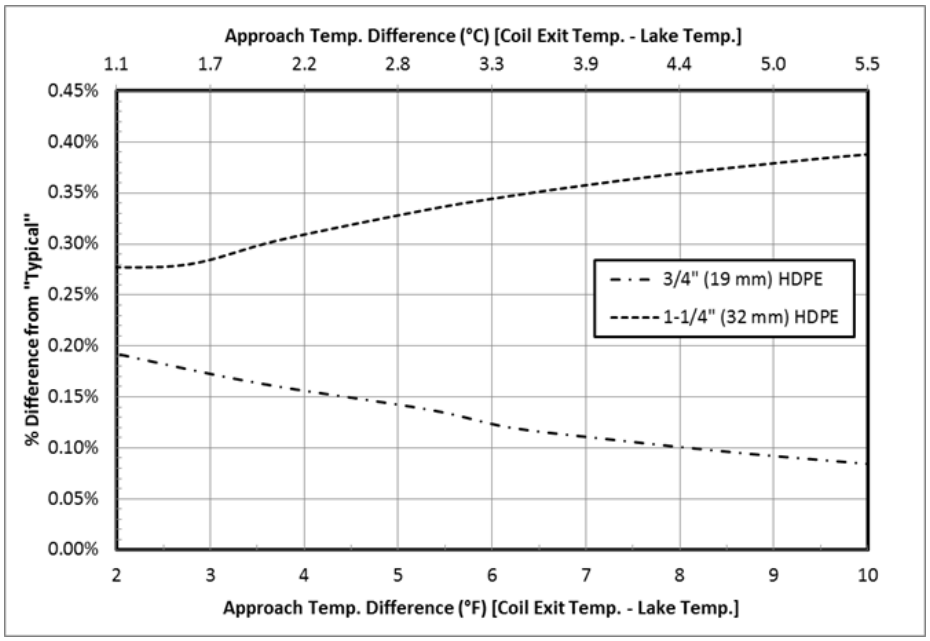

Figure 5.8: Pipe size design diagram percent error

The reason that changing pipe size has little effect is due to the fact that any increase in pipe size, and thus surface area, A_s, is offset by a decrease in convection coefficients. We also know from previously as was shown with Equation 3.35 that the ratio D_0/D_i will be constant, and therefore, so too will pipe conduction resistance. Table 5.2 below shows the convection coefficients, surface areas, and combined conductance values for the data used to generate Figure 5.7 at an approach temperature of 6°F (3.3°C). Here, we see that exactly what was described. As surface area increases, the convection coefficient decreases. As a result, the combined conductances are nearly equal to each other.

Figure 5.9 shows the variation on the base case when the largest and smallest horizontal/vertical tube-to-tube spacing is applied. All other parameters are identical to the "typical" HDPE case with the exception of the horizontal and vertical tube-tube spacing as indicated in the figure.

Table 5.2: Convection coefficients and SWHE surface areas at 6°F (3.3°C) approach temperature for Figure 5.7

Pipe Size	h_o	h_i	A, s, o	A, s, i	$((h_o A, s, o)^{-1} + (h_i A, s, i)^{-1})^{-1}$
	W/m^2K	W/m^2K	m^2	m^2	W/K
3/4 in. (19 mm)	364	1677	8.0	6.4	2281
1 in. (25 mm)	307	1131	10.0	8.0	2286
1-1/4 in. (32 mm)	257	753	12.6	10.2	2280

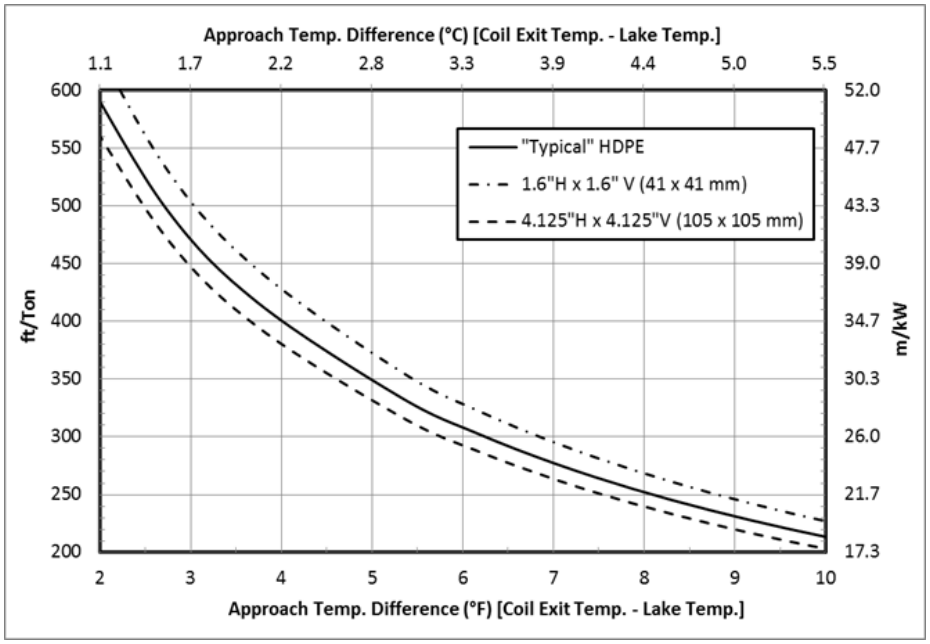

Figure 5.9: Vertical and horizontal spacing design diagram

From Figure 5.9, we see that variations in horizontal/vertical tube-tube spacing has a larger impact on the base case. This is attributed entirely to the change in outside convective resistance. The nominal difference is constant across the range of approach temperature differences at ±6% which is visible in Figure 5.10.

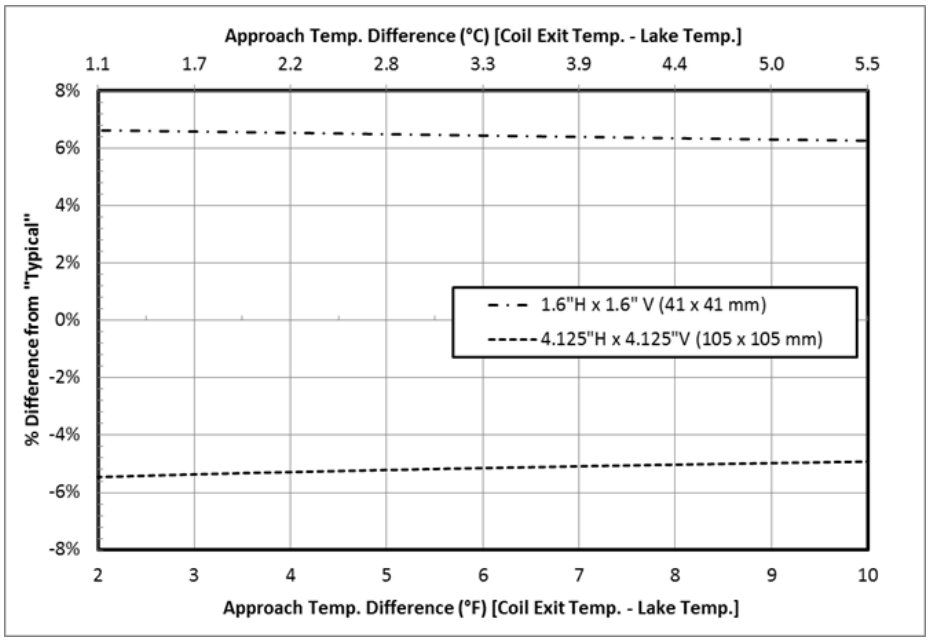

Figure 5.10: Vertical and horizontal spacing design diagram percent error

Figure 5.11 shows the variation in the base case when circulating fluid is varied. All other parameters are identical to the "typical" case with the exception of the circulating fluid as indicated in the figure.

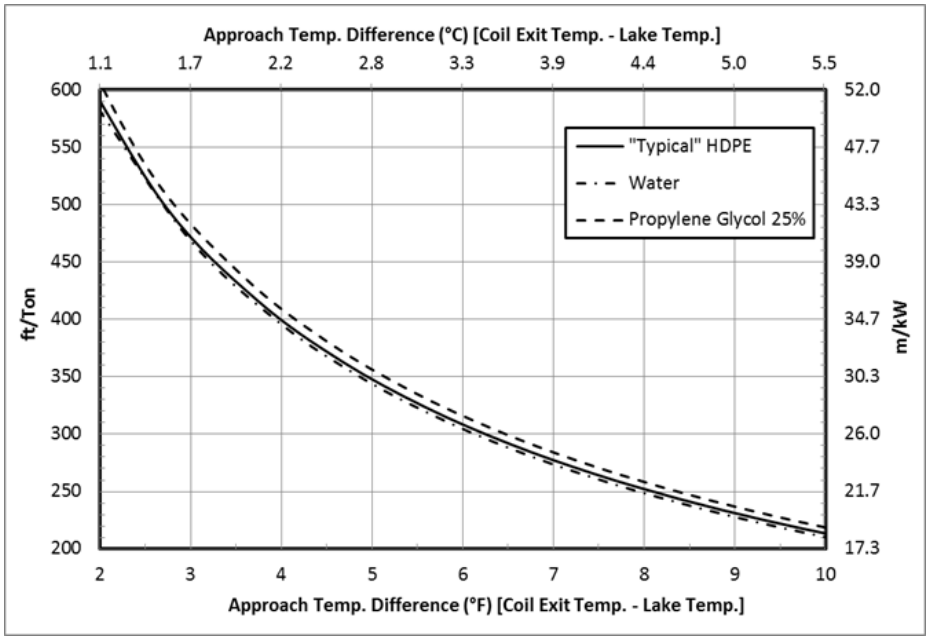

Figure 5.11: Circulating fluid comparison design diagram

In Figure 5.11, we can see that circulating fluid has a relatively small effect on the base case. Water is more thermally conductive, less viscous, has a higher specific heat, and is less dense when compared to 25% PG solution. For water, the combined effects result in a higher Reynolds number which is inversely proportional to inside convective resistance, and lower Prandtl number when compared to 25% PG solution. Since Prandtl number can be described as the ratio of viscous diffusion to thermal diffusion, lower Prandtl numbers imply a better propensity for thermal diffusion. Hence, we expect that the pure water circulating fluid to perform better than any given concentration of PG solution. The nominal difference between the "typical" case and the circulating fluid variations is ±2% which can be seen in Figure 5.12.

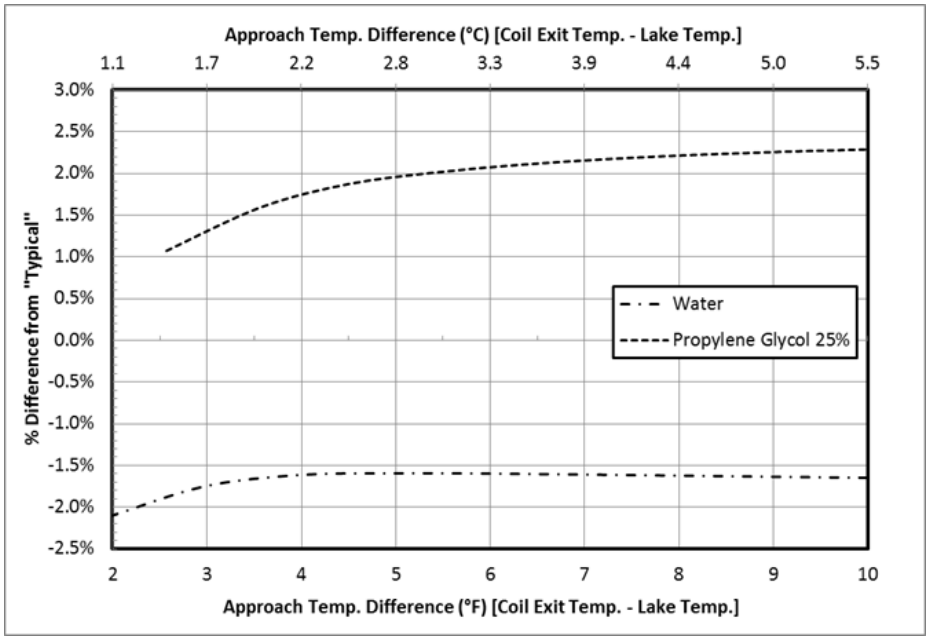

Figure 5.12: Circulating fluid comparison design diagram percent error

Figure 5.13 shows the variation in the base case when circulating fluid flow rate is varied. All other parameters are identical to the "typical" case with the exception of the circulating fluid flow rate.

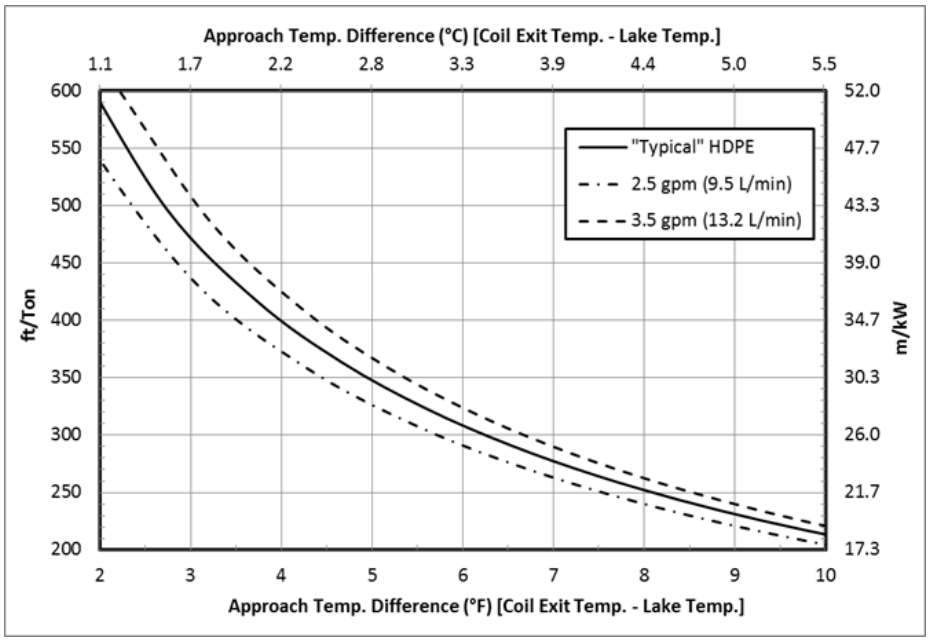

Figure 5.13: Flow rate comparison design diagram

Because it may seem counter intuitive that increasing the flow rate will require a longer tube, a brief explanation is given. The SWHE is modeled as a heat exchanger with either the log-mean temperature difference (LMTD) method, or the effectiveness-NTU (ε-NTU) method. In our case, the LMTD method is used, however, all information is also available to verify the ε-NTU method. To understand why the required pipe length increases with increasing mass flow rate, we must understand that for all cases Equation 5.1 must be satisfied.

$$\dot{Q} = \mathrm{UA}\Delta T_{lm} = \dot{m} c_{p,f} (T_{in} - T_{out}) \tag{5.1}$$

In our case, heat transfer rate is fixed. For any given approach temperature difference, the outlet temperature between the cases is also fixed due to the approach temperature definition. If we look at the right side of the equation, increasing mass flow rate requires a decrease in inlet temperature for a fixed heat transfer rate and fixed exiting fluid temperature. If the inlet temperature drops, the ΔT across the HX will therefore decrease which causes LMTD to drop. Again, in order to satisfy

the constant heat transfer condition, UA must then increase in order to balance the heat.

UA will increase in two ways. The first is due to increasing the U value from the increase in mass flow rate. This causes internal convective resistance to decease. The second is the increase in surface area. Therefore, heat exchanger length must increase with increasing flow rate to maintain the same approach temperature difference. We can see this behavior from the following data outlined in Table 5.3 which is taken from the calculations used to create Figure 5.13 at an approach temperature of 8°F (4.4°C). The lake temperature is 70°F (21.1°C) with a heat pump COP of 4.0.

Table 5.3: Parameters taken from the data used to generate Figure 5.13 at an approach temperature of 8°F (4.4°C)

Parameter	2.5 gpm (9.5 L/min)	3.0 gpm (11.4 L/min)	3.5 gpm (13.2 L/min)
ΔT_{LM} [°C]	7.33	6.90	6.59
T_{out} [°C]		25.6	
T_{in} [°C]	32.4	31.3	30.4
$T_{out} - T_{in}$ [°C]	6.8	5.7	4.9
UA [W/K]	599	638	668
$A_{s,o}$ [m^2]	7.68	8.08	8.39
$A_{s,i}$ [m^2]	6.20	6.52	6.78
h_o [W/m^{2}K]	327	323	320
h_i [W/m^{2}K]	990	1149	1305
L [m]	73.2	77.0	80.0
$\dot{m}c_{p,f}$ [W/K]	643	771	900
ε	0.61	0.56	0.52
NTU	0.933	0.827	0.743
Q_{space} [W]		3517	
Q_{coil} [W]		4396	
Q_{max} [W]	7251	7822	8394

From the table, we can verify that in order to maintain a given approach temperature, we must increase tube length. This behavior is essentially an artifact of

the approach temperature definition and the way in which the design diagrams are derived. In a real system, increasing flow rate will decrease the temperature drop across the coil but it will also increase system capacity due to the increase in mass flow rate.

As and example to demonstrate the effect of increasing flow rate, if we take the "typical" case at an approach temperature difference of 8°F (4.4°C), the approach temperature will need to increase to roughly 8.5°F (4.7°C) if the flow rate is increased to 3.5 gpm (13.2 L/min). This is determined by taking the "typical" case at a 8°F (4.4°C) approach temperature and following horizontally until the 3.5 gpm (13.2 L/min) line is intersected at approximately 8.5°F (4.7°C) approach temperature.

Figure 5.14 shows the percent difference from the different flow rate scenarios against the base case. At the lowest end of the approach temperature difference range, the percent difference ranges from +6% to -8%, while near the upper end of the approach temperature difference range, the percent differences range from +3% to -4%. Depending on the desired approach temperature difference, the designer should appropriately determine the percent correction required, depending on their situation.

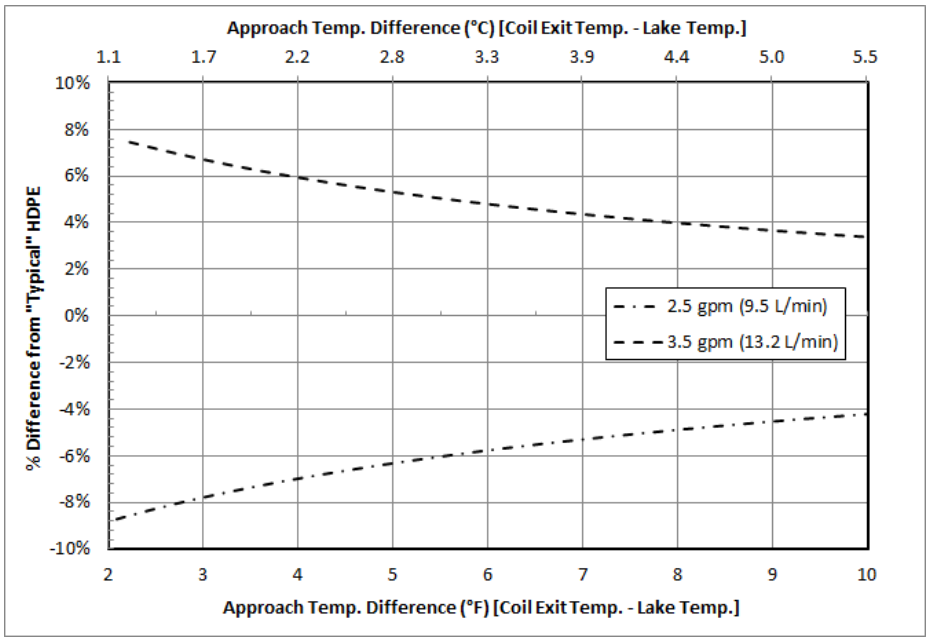

Figure 5.14: Flow rate comparison design diagram percent error

Figure 5.15 shows the variation in the base case when tube material is varied. All other parameters are identical to the "typical" case with the exception of the tube material as indicated in the figure.

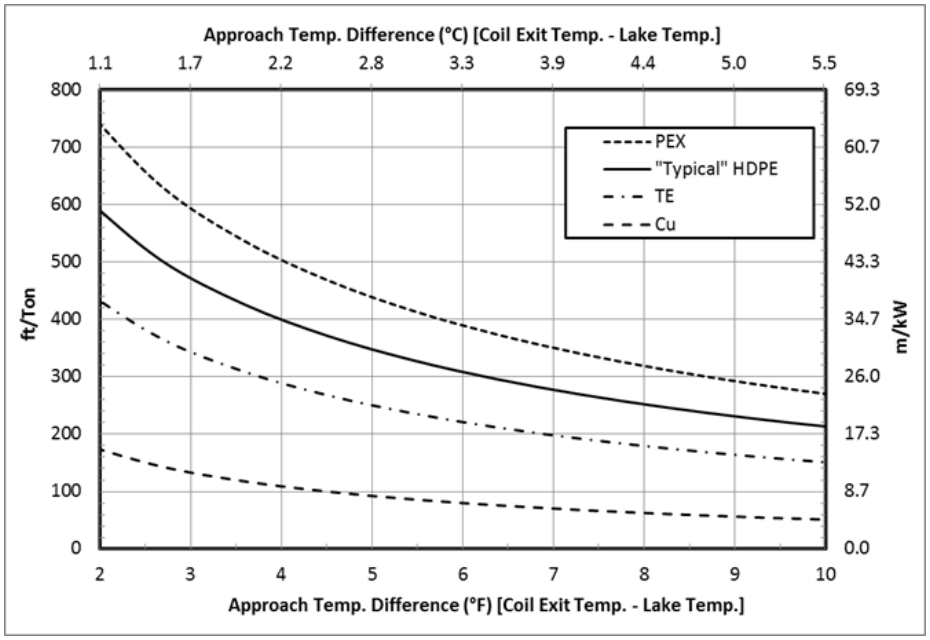

Figure 5.15: Tube material comparison design diagram

We can see from Figure 5.15 that tube material has a significant effect on required heat exchanger size. Cross linked polyethylene (PEX) is not recommended for obvious reasons. Thermal conductivity is similar to standard PE 3408 HDPE; however, the tube walls are much thicker which adds even more to the already dominant thermal resistance of the tube wall. Thermally enhanced HDPE is geometrically identical to the standard SDR-11 HDPE, however, it has a thermal conductivity that is 75% higher than that of standard HDPE. This reduces its thermal resistance and makes it an attractive alternative to standard HDPE. Copper obviously has a thermal conductivity that is much higher than standard HDPE. This makes it attractive from a heat transfer perspective, but from a financial or durability perspective designers should exercise caution.

From the base case 25% should be added if PEX piping is selected. A reduction of 30% of coil length can be realized if the thermally enhanced HDPE is used. A 70% reduction in required coil length can be expected if copper tubing is used. This can be seen for the given range of approach temperatures in Figure 5.16.

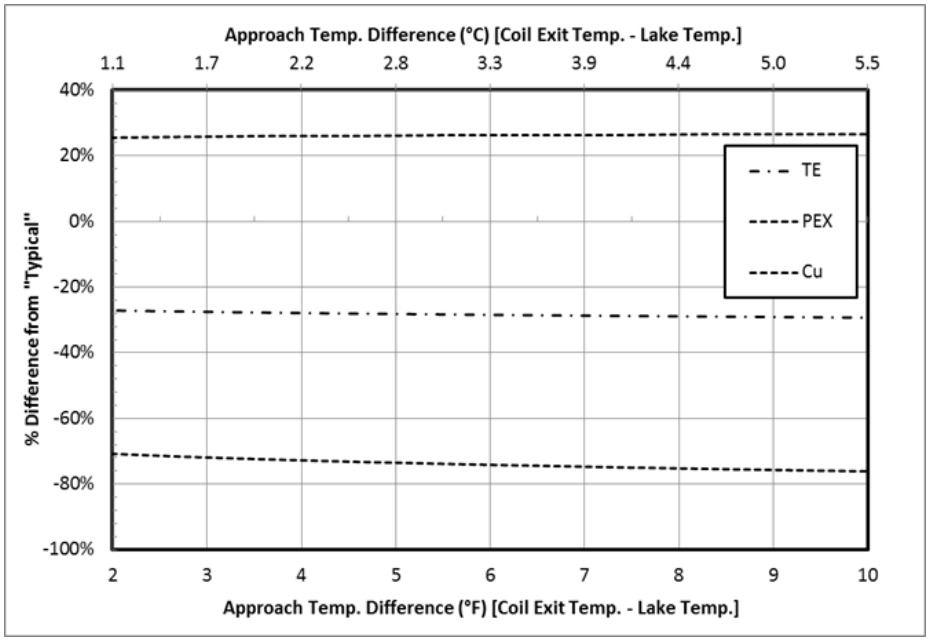

Figure 5.16: Tube material comparison design diagram percent error

Figure 5.17 shows the variation in the base case when tube schedule is varied. All other parameters are identical to the "typical" case with the exception of the tube schedule as indicated in the figure.

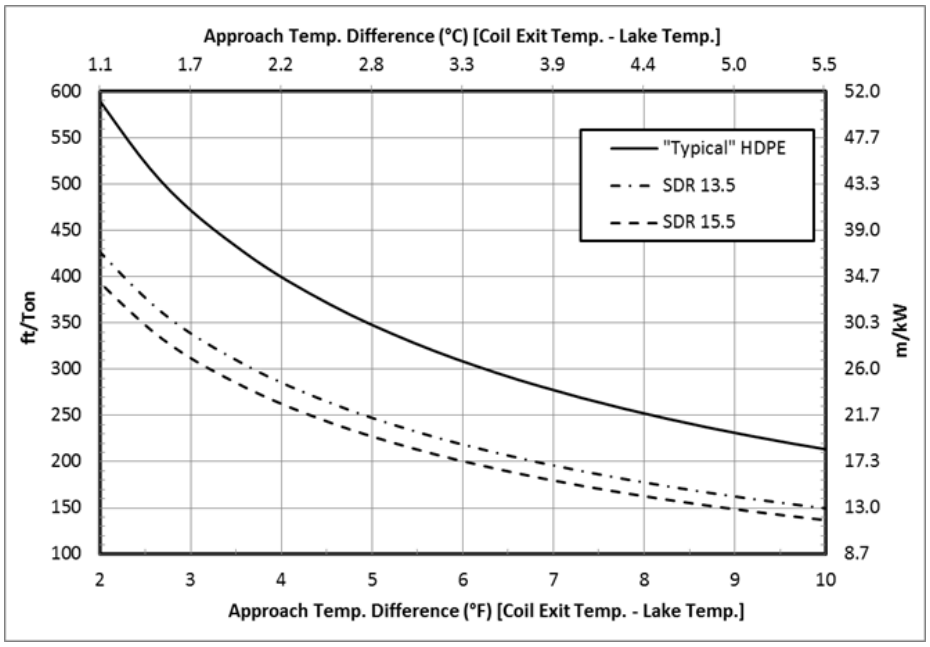

Figure 5.17: Design diagram indicating differences between different tubing schedules

From Figure 5.17 we can see that tube schedule also plays a large role in required system size. From Chapter 3, we see that the pipe can account for 60-70% of the total thermal resistance. Any reduction in this will decrease required system length. Designers can expect reductions in required length of around 29% and 35% for SDR-13.5 and SDR-15.5 pipe schedules, respectively. This is visible in Figure 5.18 over the range of given approach temperatures.

The thinner pipe, though, should be considered carefully from a durability stand point. SDR-11 HDPE is quite durable; however cases have been reported where SWHE failures have occurred due to tidal action which cause the pipes to rub on other tubes and structures. Thinner pipe walls will only lead to failure sooner if the SWHE is expected to be abraded by its surroundings.

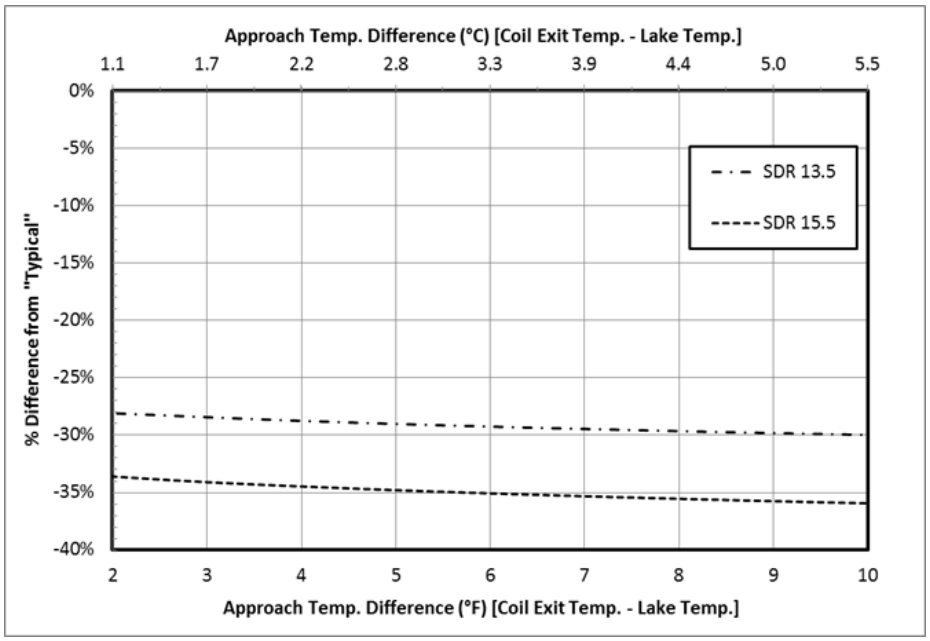

Figure 5.18: Design diagram indicating differences between different tubing schedules

Figure 5.19 shows the variation in the base case when tube external fouling is considered. All other parameters are identical to the "typical" case with the exception of the fouling as indicated in the figure.

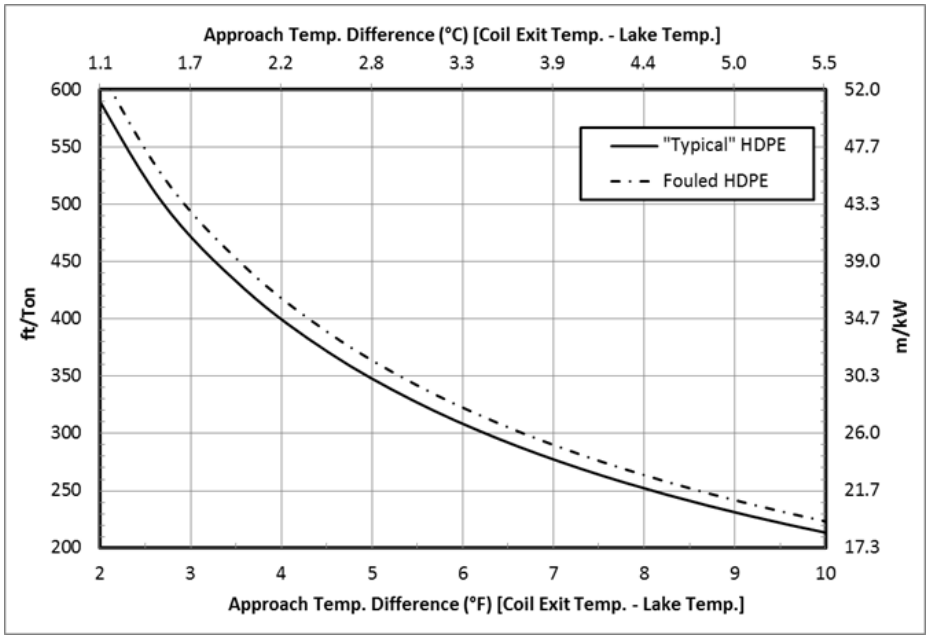

Figure 5.19: HDPE external fouling comparison design diagram

Here we see that external fouling has a small effect on the HDPE tubing because it only constitutes a small portion of the overall thermal resistance. For the base HDPE case, an increase of 4% would be required to overcome external fouling affects. This can be seen in Figure 5.20. Fouling was taken as 0.003 hr-ft^2-°F/BTU (0.00053 m^2K/W) for river water from Chenoweth (1990).

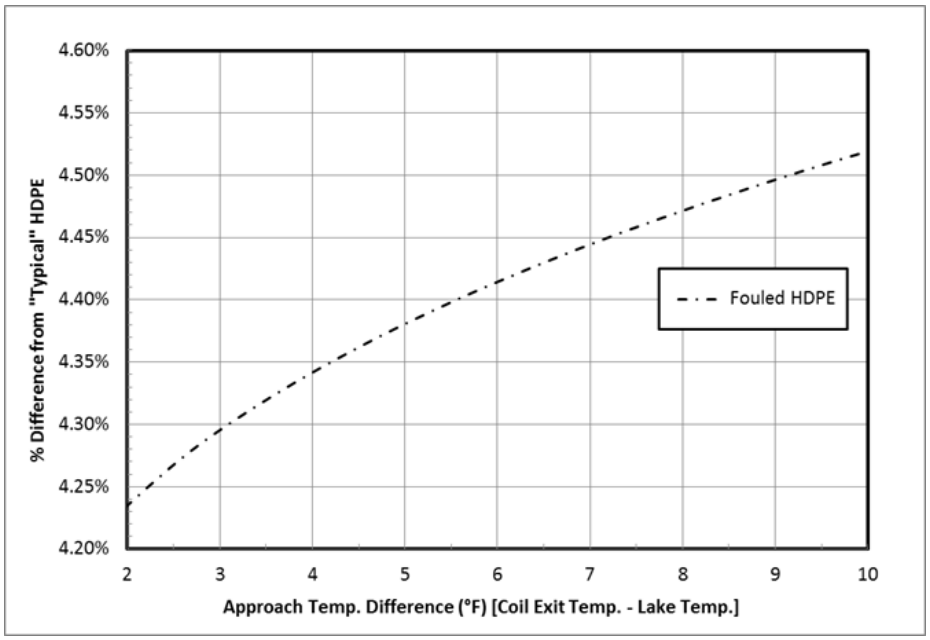

Figure 5.20: HDPE external fouling comparison design diagram percent error

Figure 5.21 shows the variation in the copper type M case when the tube external surface is fouled. All other parameters are identical to the "typical" case with the exception of the fouling and copper tubing material as indicated in the figure.

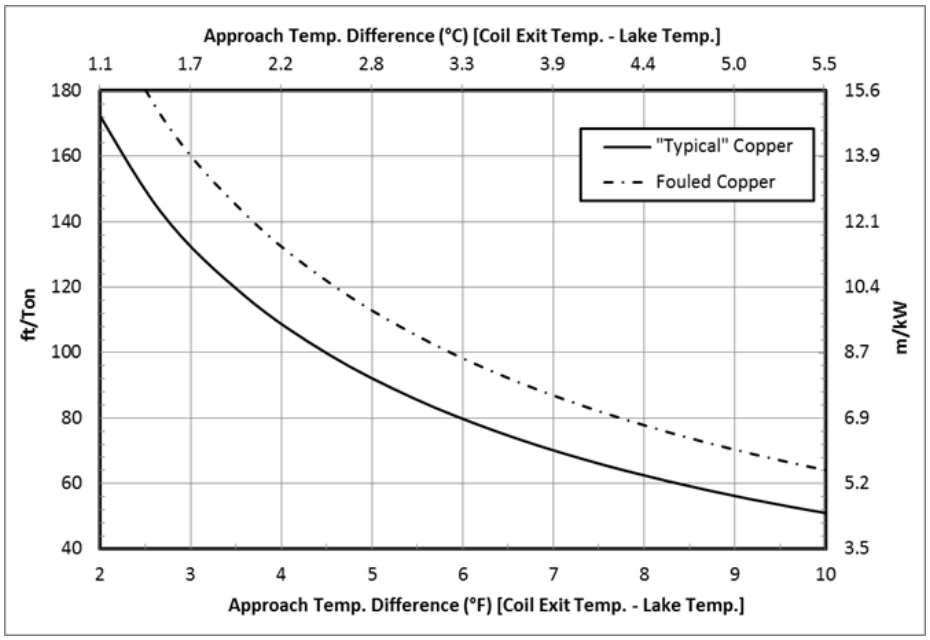

Figure 5.21: Copper external fouling comparison design diagram

Here, fouling will have a much larger effect on copper piping because tube wall resistance is a much smaller portion of the total thermal resistance. For copper, we can expect a 19-26% increase in required tube length from the lowest to highest approach temperatures indicated. The percent difference between the cases over the range of approach temperatures can be seen in Figure 5.22.

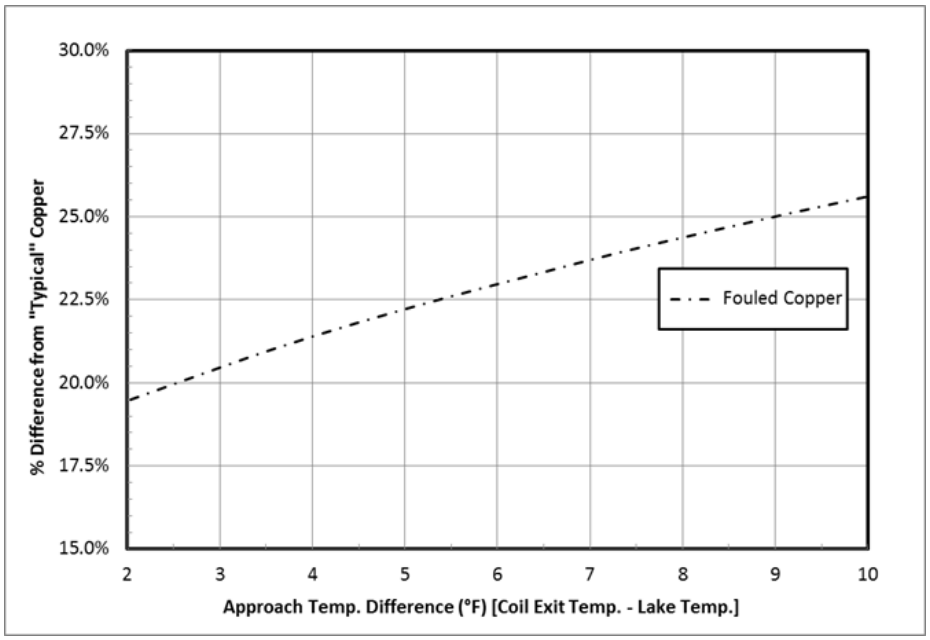

Figure 5.22: Copper external fouling comparison design diagram percent error

Figure 5.23 shows the variation in the base case when the tube internal fouling is considered. All other parameters are identical to the "typical" case with the exception of the internal fouling as indicated in the figure.

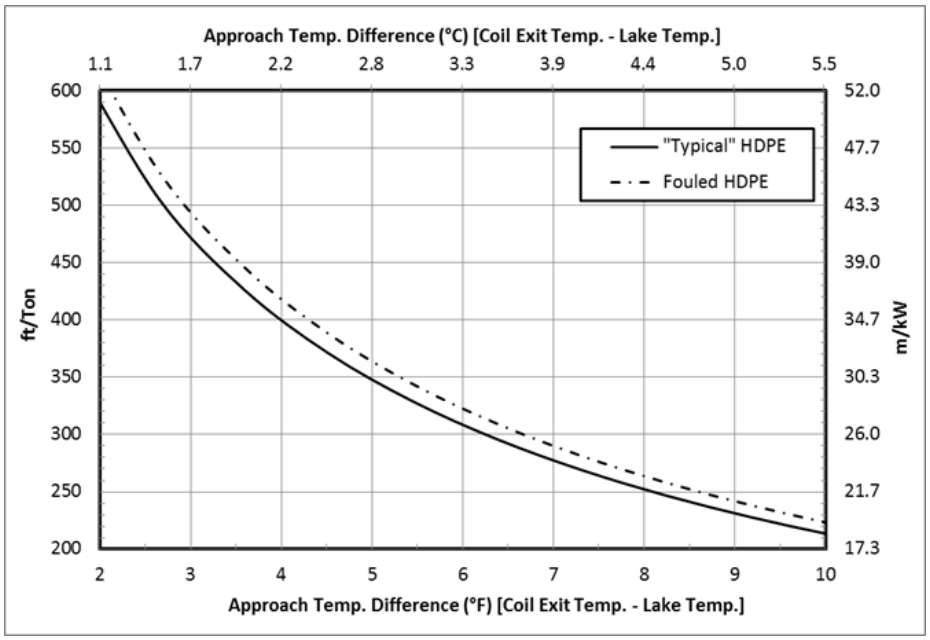

Figure 5.23: HDPE internal fouling comparison design diagram

As was the case with external fouling, we see that fouling has a small effect on the HDPE tubing because it only constitutes a small portion of the overall thermal resistance. From the base HDPE case, an increase of about 2% would be required to overcome internal fouling affects. This can be seen in Figure 5.24. Fouling was taken as 0.001 hr-ft^2-°F/BTU (0.000175 m^2K/W) for treated closed loop systems from Chenoweth (1990).

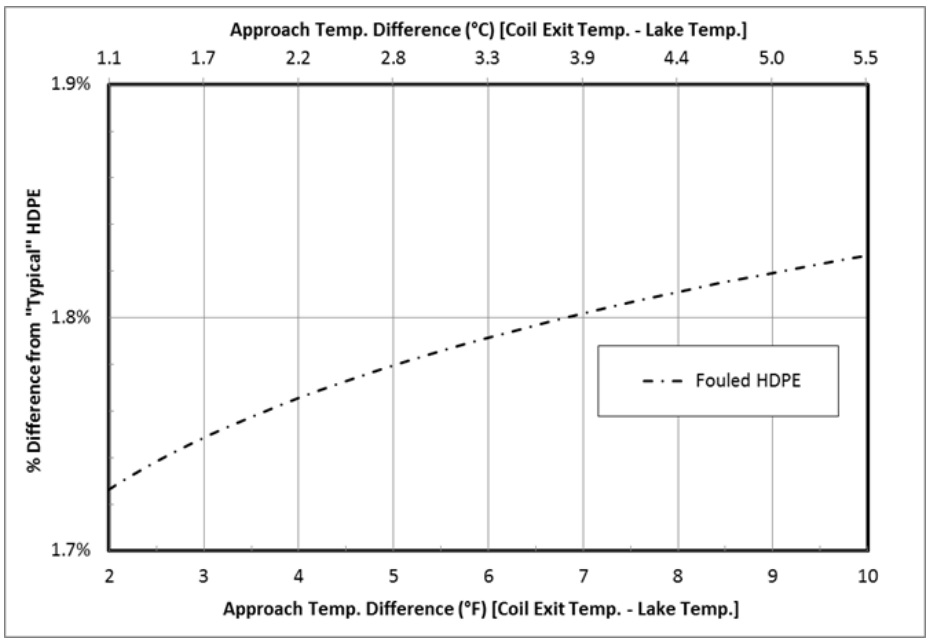

Figure 5.24: HDPE internal fouling comparison design diagram percent error

Figure 5.25 shows the variation in the copper type M case when the tube internal fouling is varied. All other parameters are identical to the "typical" case with the exception of the internal fouling and copper tubing material as indicated in the figure.

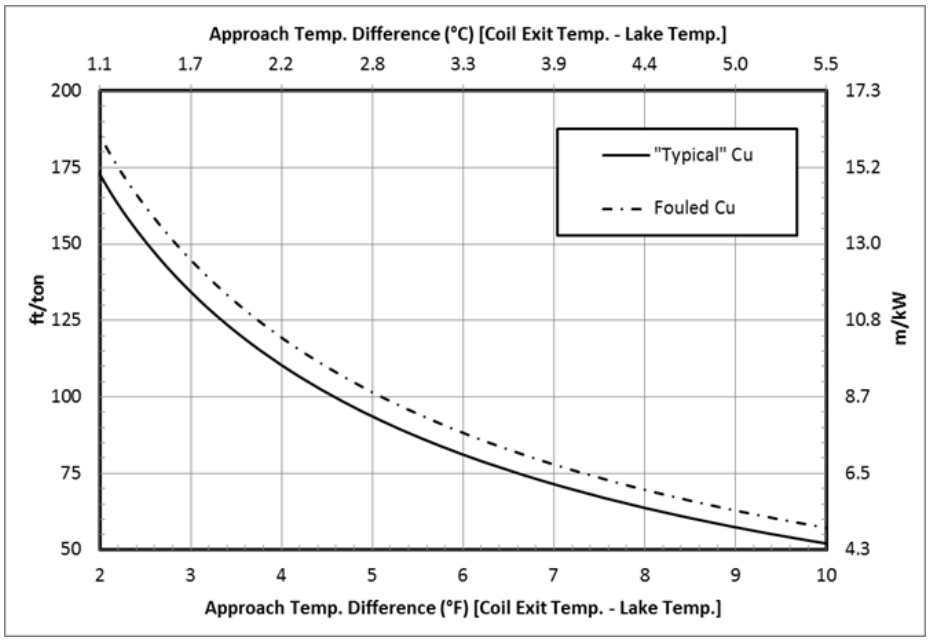

Figure 5.25: Copper internal fouling comparison design diagram

Here again, fouling will have a much larger effect on copper piping because tube wall resistance is a much smaller portion of the total thermal resistance. For copper, we can expect about a 7-9% increase in required tube length from the lowest to highest approach temperatures indicated. The percent difference between the cases over the range of approach temperatures can be seen in Figure 5.26.

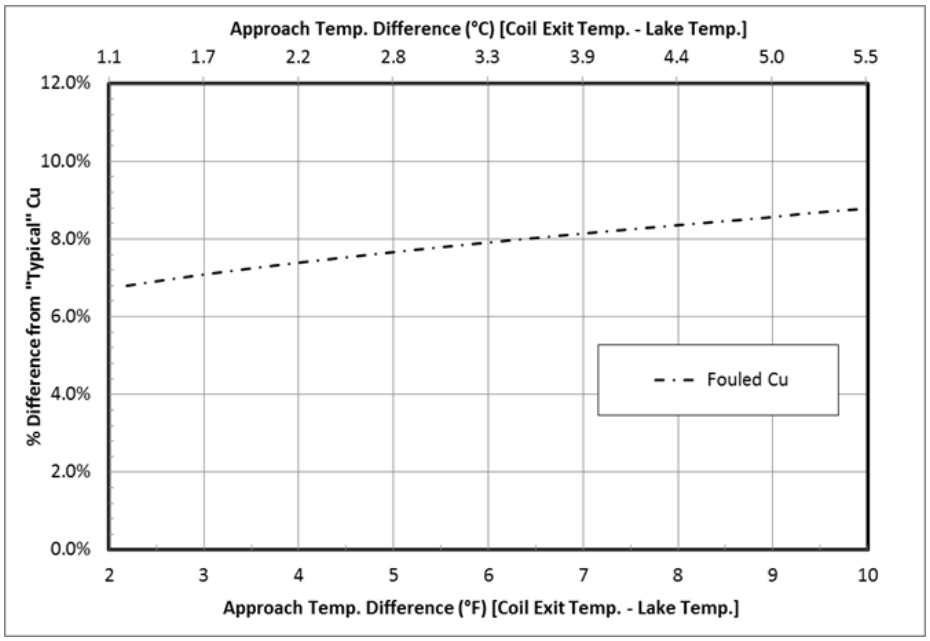

Figure 5.26: Copper internal fouling comparison design diagram percent error

Figure 5.27 shows the variation in the "typical" case when lake temperature is varied. All other parameters are identical to the "typical" case with the exception of the lake temperature as indicated in the figure.

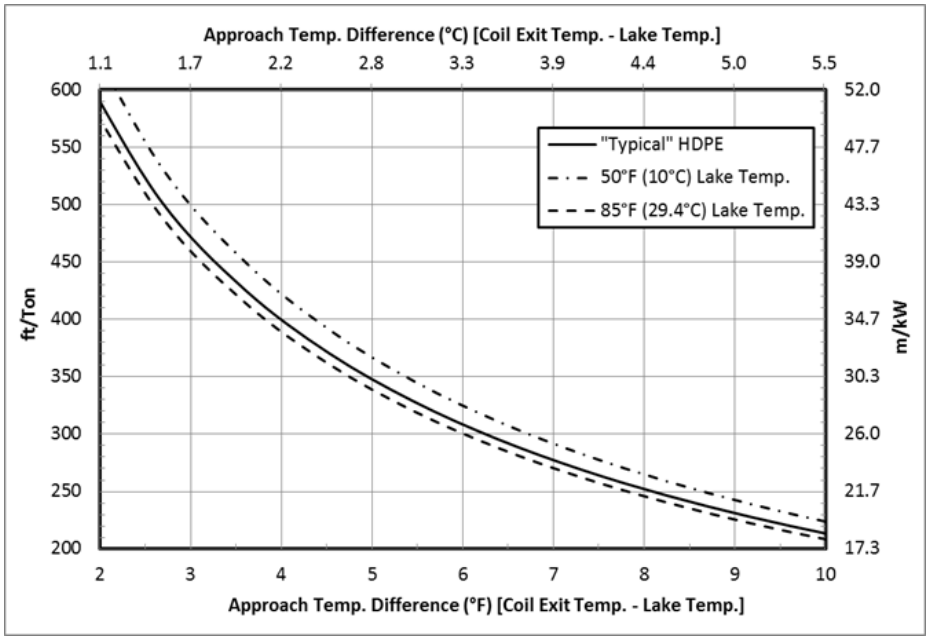

Figure 5.27: Lake temperature comparison design diagram

The percent difference due to the effect of lake temperature variation can be seen in Figure 5.28.

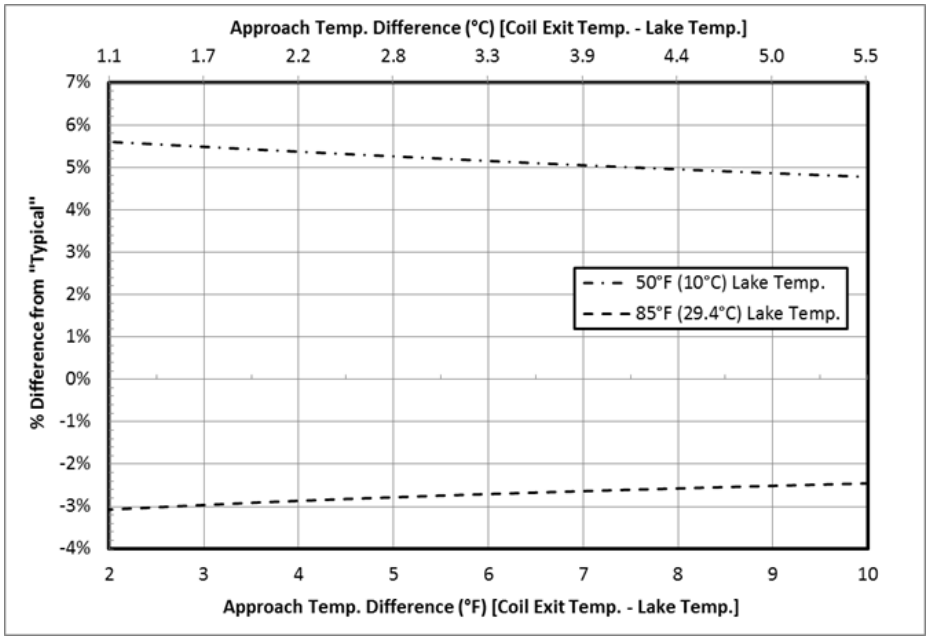

Figure 5.28: Lake temperature comparison design diagram percent error

It may seem counter intuitive that an increase in lake temperature will cause a decrease in required coil length; however this is an artifact of the approach temperature difference definition and the method whereby the diagram was derived.

$\partial\rho/\partial T$, the derivative of the density of water with respect to temperature is greater at higher water temperatures than at lower water temperatures. This is an important fact to note because $\partial\rho/\partial T$ shows up in our calculations in the thermal coefficient of expansion, which is part of the Rayleigh number. Therefore, at higher lake temperatures, Rayleigh numbers will be higher and will predict a lower outside convection resistance when compared to lower lake temperatures, even though the approach temperature differences may be identical.

From a heat transfer perspective, we understand that lower lake temperatures are more favorable from a system point of view. Figure 5.29 shows the required coil length plotted against lake temperature for four separate heat pump entering fluid

temperature (EFT) isotherms. All other parameters are identical to the "typical" HDPE case. Here we can clearly see that lower lake temperatures are more favorable from a heat transfer perspective. For example, if we have 200 ft/ton (17.3 m/kW) of installed coil, for a lake temperature of 94°F (34.4°C), the heat pump EFT will be around 105°F (40.6°C) which is going to have a much lower heat pump COP when compared to a 64°F (17.8°C) lake which will have a 75°F (23.9°C) heat pump EFT. For the example, even though the approach temperatures are identical, overall system performance will be much better at lower lake temperatures.

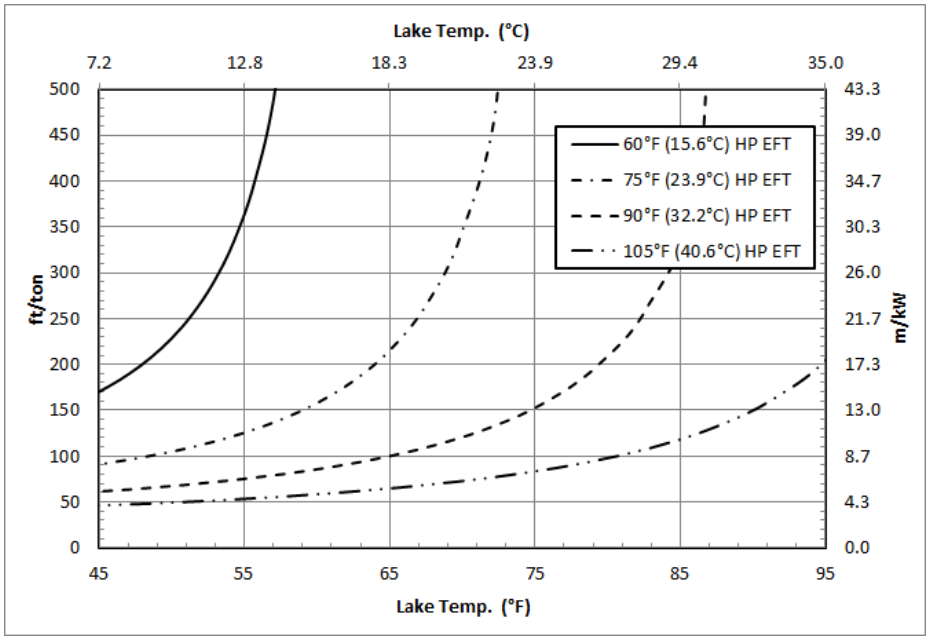

Figure 5.29: Heat pump EFT isotherm plot of required coil length plotted against lake temperature

Designers could use this discussion to compare their application and lake temperature to the "typical" lake temperature of 70°F (21.1°C) and then make a decision regarding how best to implement the results. If for example, the proposed design in in northern Canada and the lake temperature is not expected to exceed 50°F (10°C) during the cooling season, the designer may wish to consider increasing installed length by 5% to account for the lower values of $\partial\rho/\partial T$ which occur at these temperatures.

A designer in southern Florida, may consider the reverse.

Figure 5.30 shows the variation in the "typical" HDPE case when the lake is expected to have quiescent conditions, or by some other means convective motion is constrained. All other parameters are identical to the "typical" HDPE case with the exception of the outside convection coefficient as was indicated in Section 4.4.

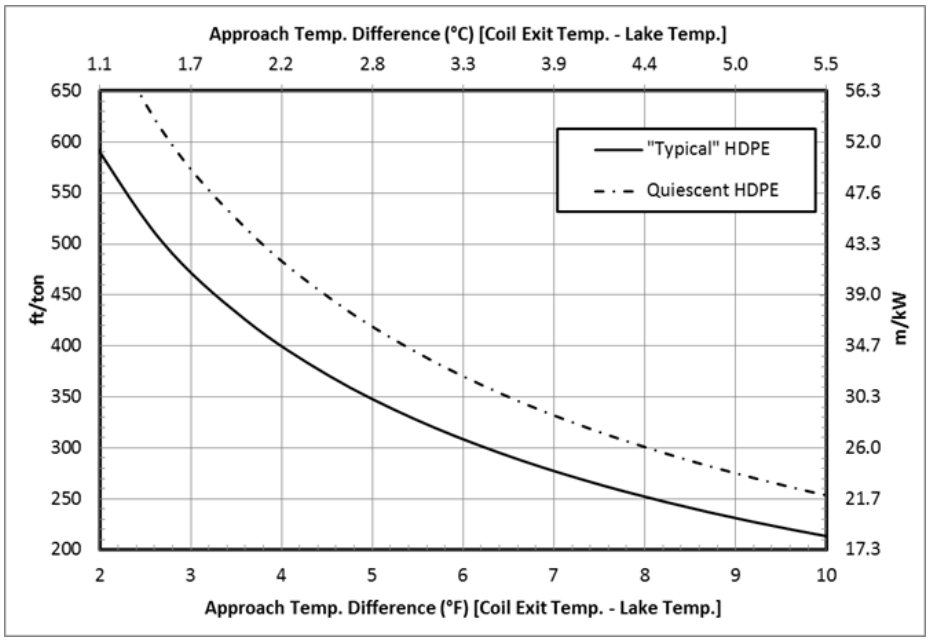

Figure 5.30: Quiescent HDPE pond design diagram

The results indicated in this figure are a result of the differences in outside convective resistance base on the experimentally derived convection correlation from Chapter 4. Due to the increase in outside convective resistance, an increase in required installation length would be required if the system was expected to operate in a surface water body that constrained the convective motion. The percent difference from the "typical" HDPE case across the range of approach temperatures can be seen in Figure 5.31.

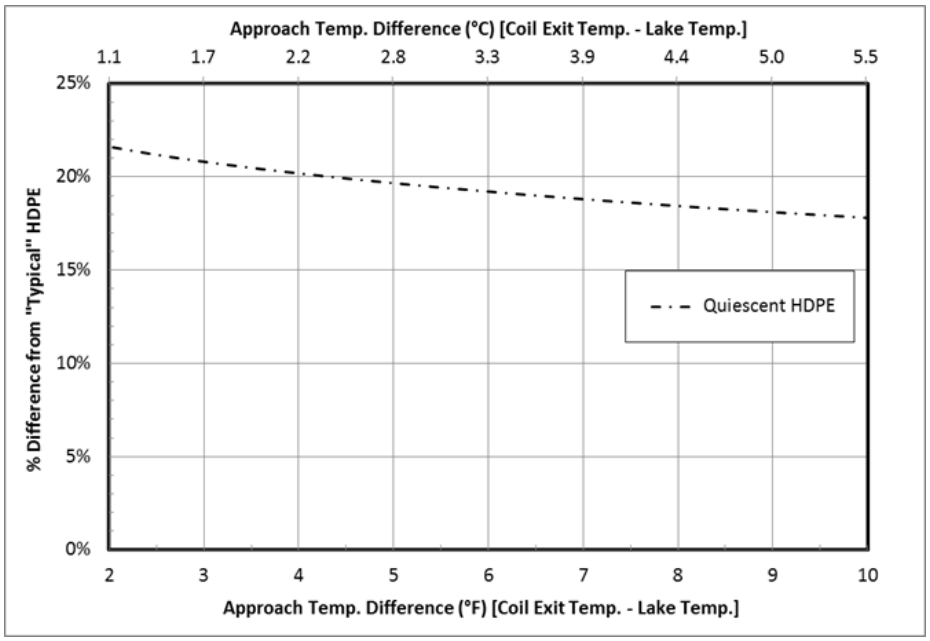

Figure 5.31: Quiescent HDPE pond design diagram percent error

Figure 5.32 shows the variation in the "typical" copper case when lake is expected to have quiescent conditions. All other parameters are identical to the "typical" copper case with the exception of the outside convection coefficient as was indicated in Section 4.4.

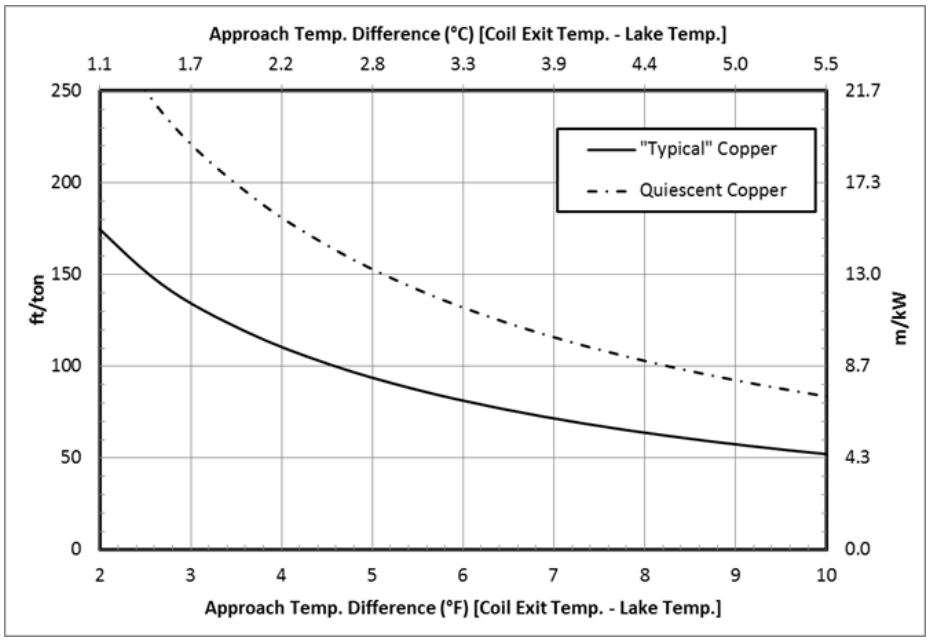

Figure 5.32: Quiescent copper pond design diagram

Here, because the outside convective resistance is a much larger portion of the SHWEs total thermal resistance, an increase of installed pipe length of around 61% would be required if quiescent conditions are expected to occur. Figure 5.22 shows the percent difference from the "typical" copper case over the range of given approach temperatures.

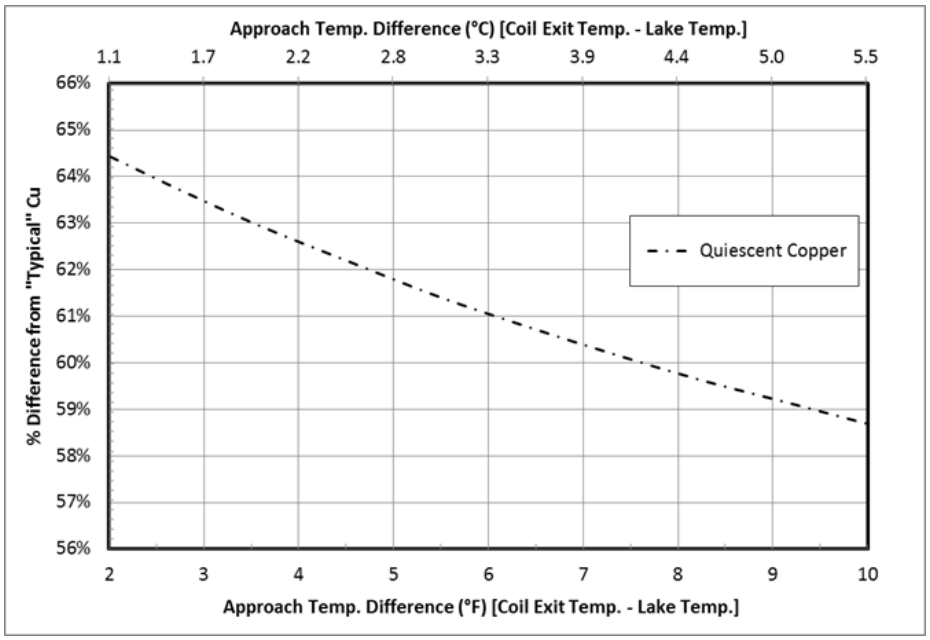

Figure 5.33: Quiescent copper pond design diagram percent error

Tables 5.4 shows a summary of the percent change from the "typical" HDPE case when comparing different design parameter variations for the same approach temperature difference. The table can be implemented by comparing a proposed design to the "typicial" design. This can then be used to determine overall percent correction by using Equation 5.2. This equation combines the percent error differences, p, from the different parameters into a single percent error correction factor, P.

$$P = (1 + p_1) \cdot (1 + p_2) \cdots (1 + p_n) \tag{5.2}$$

As an example, the "typical" case will be compared to the "best" case. When compared to the "typical" case, the "best" case has a lower COP, higher lake temperature, larger tube size and larger tube-tube spacing, and water the circulating fluid. From Table 5.4, we can see that an average percent difference for each respective parameter listed is, +3% for lower COP, -3% for higher lake temperature, -5% for larger tube-tube spacing, and -2% for water. These parameters are shown calculated in Equation 5.3.

$$P_{best} = (1 + 0.03) \cdot (1 - 0.03) \cdot (1 - 0.05) \cdot (1 - 0.02) \approx 0.93 \tag{5.3}$$

The calculation results in an approximate decrease in required tube length of 7% when comparing the "best" case to the "typical" case. This can be verified by the results shown in Figure 5.2, where the "best" case is shown to be roughly 4-8% below the "typical" case.

Table 5.4: Percent change from "typical" HDPE case for different SWHE and SWHP system parameter variations based on space cooling conditions

Parameter	% Diff. from "typical" case	Notes
HP COP_h: 2.0	+7-13%	
HP COP_h: 3.0	+2-4%	See Figure 5.6
HP COP_h: 5.0	-2-3%	
3/4 in. HDPE	<1%	
1-1/4 in. HDPE	<1%	
Small Tube Spacing	+6%	
Large Tube Spacing	-5%	
Water	-2%	
25% PG	+2%	
2.5 gpm	-8-4%	See Figure 5.14
3.5 gpm	+6-3%	
PEX	+25%	
TEHDPE	-25%	
Copper	-70%	
SDR 13.5	-30%	
SDR 15.5	-35%	
External Fouling	+4%	
Internal Fouling	+2%	
Low Lake Temp	+4%	
High Lake Temp	-3%	
Quiescent Surface Water	+18-22%	See Figure 5.31

Table 5.5 shows the percent change from the "typical" copper case due to parameter variations. This table will give an estimate of the percent change from the

"typical" copper case due to external and internal fouling, as well as quiescent pond conditions.

Table 5.5: Percent change from "typical" copper case for different SWHE and SWHP system parameter variations based on space cooling

Parameter	% Diff. from "typical" case	Notes
External Fouling	+19-26%	See Figure 5.22
Internal Fouling	+7-9%	See Figure 5.26
Quiescent Surface Water	+59-64%	See Figure 5.33

5.3 Space Heating Design Graphs

Space heating presents some significant challenges when it comes to designing surface water heat pump systems. This is due to the fact heat must be extracted from the surface water in order to provide space heating. The first law of thermodynamics tells us that in order to extract heat from the surface water body, the SWHE circulating fluid temperature must be lower than the surface water temperature. Lowering the circulating fluid temperature can become problematic if the temperature is dropped below the freezing point of water. As was shown in Chapter 3, dropping the circulating fluid temperature below the freezing point of the surface water body can cause ice-on-coil freezing. Should enough ice build on the SWHE, system performance will decrease. Potential SWHE damage could also occur if the SWHE becomes buoyant and begins to float.

When compared to systems used for space heating, space cooling systems are not inherently safe from a system design perspective. If a SWHE for a space cooling system is undersized, circulating fluid temperatures will rise until the heat transfer rate between the system and the lake are balanced. However, for space heating applications, an undersized system will cause loop temperatures to drop, possibly below the freezing point of the surface water. This potentially could cause icing

which can reduce system performance or damage the SWHE.

In this section, no "typical" design case will be given. Only the most conservative estimates of what can be done in the region prior to coil icing. Also, no information will be given for sizing coils under ice-on-coil freezing conditions.

Figure 5.34 shows a lake temperature isotherm plot showing required coil length plotted against approach temperature difference. Table 5.6 shows the SHWE and SWHP system parameters used to generate Figure 5.34.

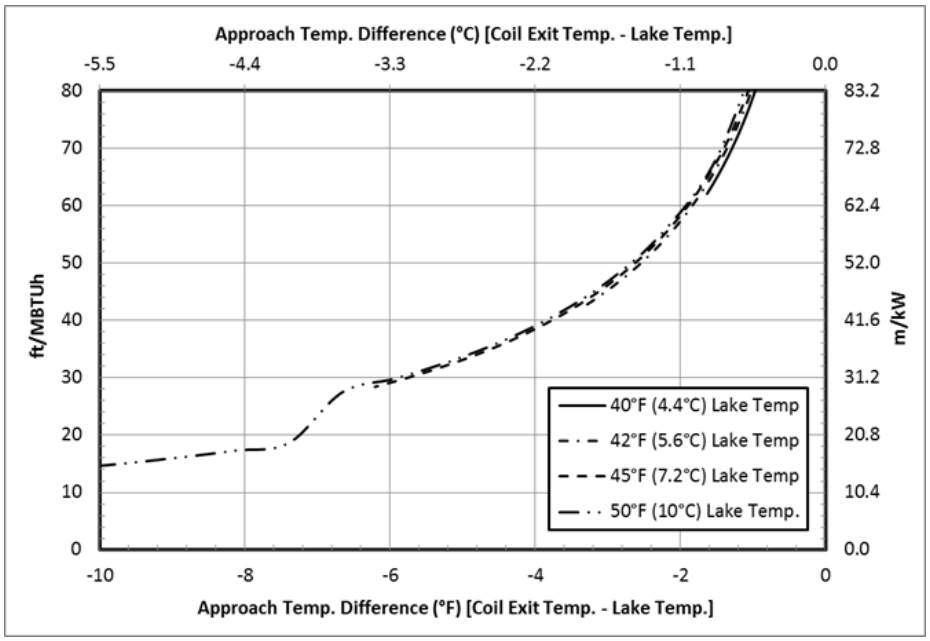

Figure 5.34: Space heating design diagram for HDPE SWHE

For the 50°F (10°C) lake temperature curve, the sharp decrease in required pipe length below an approach temperature of -7° (-4°C) is due to the discontinuous nature of the convection correlation for heat extraction. This behavior was described in Section 4.2.5.

A similar diagram was created for copper heat exchangers. This is shown below in Figure 5.35. All parameters are identical to the parameters shown in Table 5.6 with the exception of the tube material, which was changed to copper, and tube size which was changed to a 1 in. (25 mm) nominal Type M tube size.

Table 5.6: SWHE and SWHP system parameters used to generate Figure 5.34

Lake Temp	40°F (4.4°C)	42°F (5.6°C)	45°F (7.2°C)	50°F (10°C)
HP COP_c	2.9	3.2	3.5	3.8
Tube Spacing	4.125 in. H x 4.125 in. V (105 mm x 105 mm)			
Tube Size	3/4 in. (19 mm)			
Tube Material	HDPE			
Flow Rate	3 gpm (11.4 L/min)			
Space Heating	12,000 BTU/h (3,517 W)			
Circulating Fluid	12.5% Propylene Glycol			
Fouling	None			
SW Correlation	Pond			

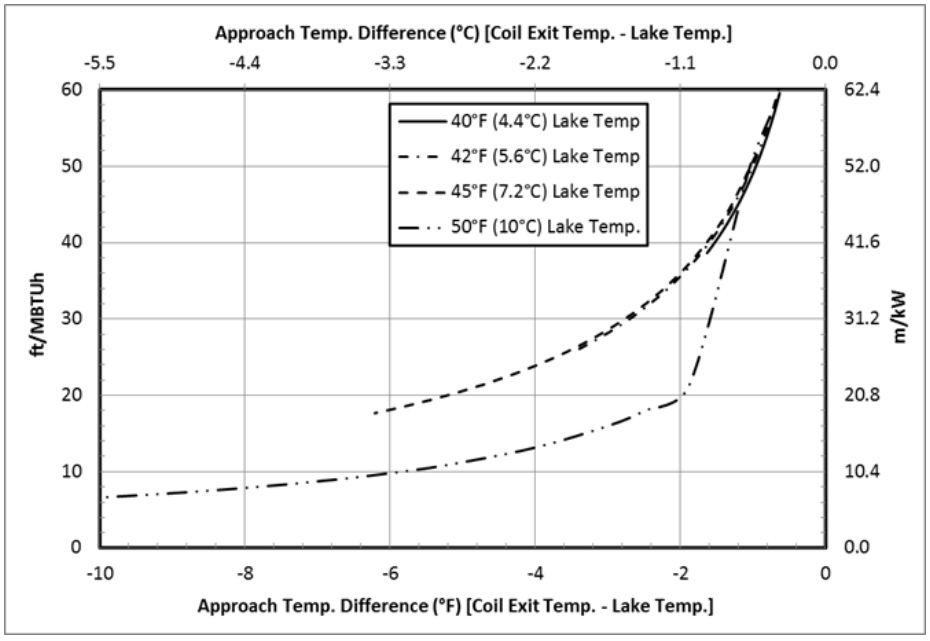

Figure 5.35: Space heating design diagram for copper SWHE

Here again, the 50°F (10°C) lake temperature curve indicates the discontinuous nature of the convection correlation for heat extraction. As was the case with the HDPE design diagram, the outside Rayleigh numbers for the lake temperature curves less than 50°F (10°C) never exceed $Ra_D^* = 1 \cdot 10^6$. Comparing the HDPE and copper

diagrams shows, as expected, that the copper coil length could be reduced if copper is selected.

Extrapolation beyond the lower limit of the curves provided in Figures 5.34 and 5.35 is not permitted due to the fact that coil freezing may occur which would cause system performance to decrease. Also, if sufficient ice is allowed to form on the coil, the buoyant forces may tear the coil free from its anchors, potentially damaging or destroying the surface water heat exchanger.

From our experience, coiled heat exchangers perform with relatively little performance degradation under initial icing conditions, so long as the ice forming on the tube surface has not intersected the ice forming on adjacent tube surfaces. However, if the gap between the tubes is allowed to bridge, the heat exchanger essentially becomes a solid block of ice eliminating surface water flow between the tubes. Outside convective resistance will become so large that no heat transfer will be able to take place.

One method that may allow for continued operation when lake temperatures drop to unfavorably low levels is to increase the circulating fluid flow rate. This could be used for lakes where the lake temperature is only expected to drop to dangerously low temperatures for a small period of time. Increasing the circulating fluid flow rate will allow operation at extended temperatures up to a certain point. Figure 5.36 shows an approach temperature difference isotherm plot of minimum lake temperature as a function of circulating fluid flow rate. For Figure 9-14, coil inlet temperatures were set at 32.5°F so as to avoid coil icing.

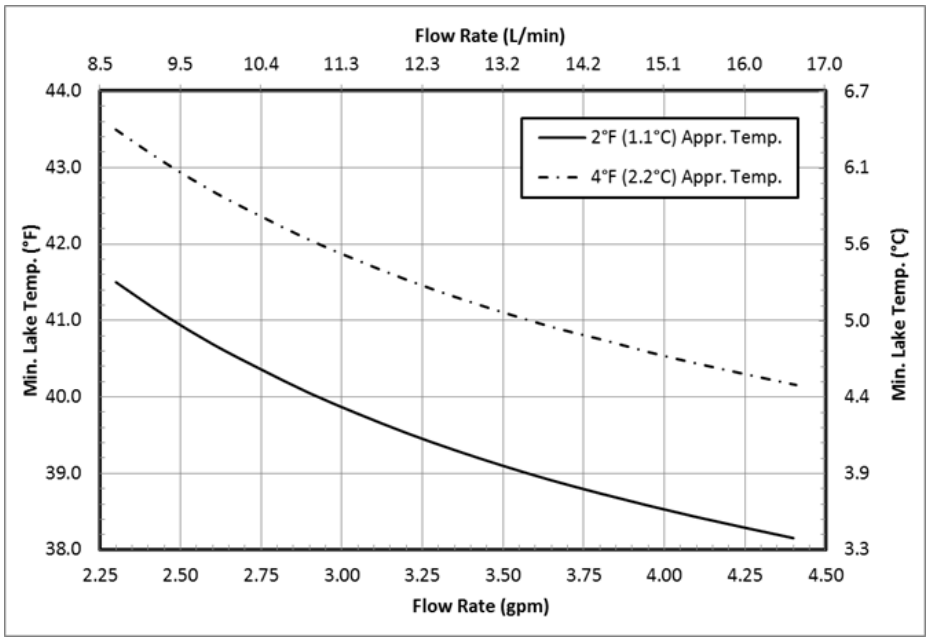

Figure 5.36: Approach temperature isotherm plot of minimum lake temperature plotted against required flow rate

We can see from Figure 5.36 that increasing fluid flow rate may allow for operation at lower lake temperatures, but only to a certain extent. The additional energy expended pumping the fluid at a higher flow rate may be equal to, or greater than the energy required to add the necessary supplementary heating.

The companion to Figure 5.36 which was taken from the same simulation is Figure 5.37. This figure shows the tube length required at the given lake and approach temperatures to meet the zone heating load.

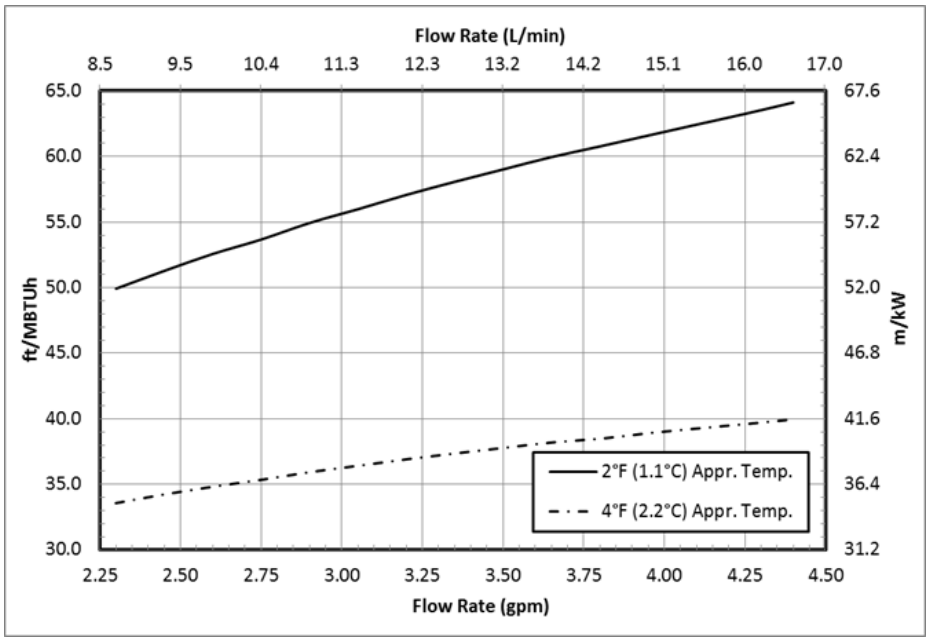

Figure 5.37: Approach temperature isotherm plot of required tube length plotted against required flow rate

As a general recommendation, coil tube-tube spacing should be kept at as great a distance as possible if the potential for icing exists. This will allow for the greatest safety factor if high heating periods are encountered and some freezing occurs. However, if the designer determines that under their given circumstances, coil icing is likely, supplementary heating should be provided or other heat exchanger designs should be explored.

CHAPTER 6

CONCLUSIONS

6.1 Conclusions

The work presented in this thesis began by developing equipment to experimentally measure external convection coefficients for spiral-helical surface water heat exchangers. These surface water heat exchangers are used to reject heat to, or extract heat from surface water bodies for space cooling, or space heating applications. Once the experimental equipment was developed, experiments were performed under heat rejection and heat extraction conditions. The experiments were performed in a 3 acre (1.2 ha) test pond, as well as a 15 ft (4.6 m) test pool. For heat rejection experiments, the equipment initially developed by Austin (1998) and later modified by Hansen (2011) was use to heat and circulate water in a closed loop. For the heat extraction experiments, a new experiment was developed which utilized two heat pumps with a nominal capacity of 4 tons (14 kW) to cool and circulate propylene glycol solution in a closed loop.

After the completion of the experiments, experimentally derived convection correlations for spiral-helical surface water heat exchangers were developed from parameter estimation techniques. These convection correlations are summarized in Section 4.4. These correlations have been shown to predict outside Nusselt number to within 28% RMSE for heat rejection cases, and within 13% RMSE for heat extraction cases. When implemented in a simulation to compare predicted heat transfer rates these correlations predict heat transfer rate to with 7% RMSE for heat rejection cases, and within 5% RMSE for heat extraction cases.

From the convection correlations summarized in Section 4.4, design diagrams were developed for SWHE design purposes. For the case of heat rejection, many different SWHE and SWHP system parameters were varied in a simulation to determine SWHE performance and sensitivity when compared to the "typical" case. The parameters which were varied are: heat pump COP, lake temperature, horizontal/vertical tube-tube spacing, pipe size, pipe schedule, pipe material, circulating fluid flow rate, circulating fluid, internal and external fouling, and pond or quiescent surface water conditions. The design diagrams for space cooling are presented in Section 5.2, as well as the method for combining the percent differences for multiple parameters.

For space heating, a design diagram was given in Section 5.3, as well as some general recommendations for space heating application. As part of the design recommendaions for space heating applications, the tube-tube spacing should be kept as large as is feasible. This allows a margin of safety in case ice-on-coil conditions occur. Supplemental heating should also be considered when designing surface water heat pump systems for space heating applications.

6.2 Recommendations for Future Work

During the course of this work, several topics were identified which are classified as future research topics which were beyond the scope and time limits of this project. These topics are outlined in the following points.

1. **Surface water cooling comparisons to conventional cooling systems.** A comparison of surface water cooling systems to conventional cooling systems is a topic which was identified while performing research for the publication Mitchell & Spitler (2013). Although there are many potential locations where these systems could be deployed, little information is available comparing the life cycle costs of these systems. This information is critical for a designer to seriously consider this design option.

2. **SWHP system to GLHE system comparisons.** There is currently no information available to designers comparing the potential life cycle cost implications of choosing a SWHP system vs. a GLHE system, assuming that both options are available. This work would clarify the issues associated with ground heat storage, balanced heating and cooling loads, geographical and climatalogical effects.

3. **Plate heat exchanger convection correlations in standing and flowing water.** There is currently little published information regarding the performance of surface water plate heat exchangers. These heat exchangers are an attractive alternative to spiral-helical or other HDPE SWHEs due to the reduced labor associated with their construction. These heat exchangers are used in a diverse range of operating conditions from stagnant ponds, flowing rivers, to coastal waters. Hansen (2011) performed some work to determine overall heat exchanger performance, however interior convection resistance was roughly estimated. Some additional work to correlate plate interior and exterior convection coefficients would be useful for system designers and modelers.

4. **Tesing using Copper SHWEs.** Because the thermal resistance of copper is inherently low, testing with copper SHWEs would eliminate the uncertainty in the external convection coefficient measurements. An alternative approach to the approach taken in this work would be to test using smaller copper SHWEs in a large tank. A method could then be developed to scale the heat transfer results to match actual size SWHEs.

5. **Test and compare alternative surface water heat exchangers.** There is currently no work that compares the different varieties of surface water heat exchangers on common terms. Other varieties of surface water heat exchangers that are of interest are, slinky coils on the bottom, plate heat exchangers, and

capillary type heat exchanegers.

REFERENCES

ASTM. 2012. *Standard Specification for Polyethylene (PE) Plastic Pipe (DR-PR) Based on Controlled Outside Diameter -- ASTM D3035*. West Conshohocken, PA: ASTM International.

Austin, W. A. 1998. Development of an In-situ System for Measuring Ground Thermal Properties. M.S. Thesis. Oklahoma State University: Stillwater, OK.

Backlund, L 1982. In Swedish--Resultant från prov i storsjön med värmeväxlare för utvinning av termisk energi ur vattendrag. *Sjövärmesystem.* Stockholm, Sweden: May, 1982. 14-28. Stockholm, Sweden: Byggforskningsrådet.

Billfalk, L ed. 1982. In Swedish—*Sjövärmesystem-BFR-seminarium.* Stockholm, Sweden: May, 1982. Stockholm, Sweden: Byggforskningsrådet.

Cengel, Y. A. and A. J. Ghajar. 2011. *Heat and Mass Transfer-Fundamentals and Applications,* 4th Edition. New York, NY: McGraw-Hill.

Chenoweth, J. M. 1990. Final Report of the HTRI/TEMA Joint Committee to Review the Fouling Section of the TEMA Standards. *Heat Transfer Engineering.* 11(1): 73-107.

Chiasson, A.D. 1999. Advances in Modeling of Ground Source Heat Pump Systems. M.S. Thesis. Oklahoma State University: Stillwater, OK.

Churchill, S. W. and H. H. S. Chu. 1975. Correlating Equations for Laminar and Turbulent Free Convection From a Horizontal Cylinder. *International Journal of Heat and Mass Transfer.* 18(9): 1049-1053.

Ciani, J. 1978. Sea/lake Water Cooling for Naval Facilities. Report N-1528. Port Heuneme, CA: Civil Engineering Laboratory.

DOE 2010. Buildings Energy Data Book -- Table 1.1.3. Department of Energy. URL: http:// buildingsdatabook.eren.doe.gov. Accessed: March 10, 2013.

Eliadis, C. 2003. Deep Lake Water Cooling - A Renewable Technology. *Electrical Line.* 9(3): 26-28.

Gonthier, S. 2012. Geoperformx Thermally Enhanced Pipe for Geothermal Applications. International Ground Source Heat Pump Associaion. URL: http://www.igshpa. okstate.edu/membership/members_only/proceedings/2012/10-4-2012-1030-Session-A-VERSAPROFILES%20copy.pdf. Accessed: August 23, 2013.

Hansen, G. M. 2011. Experimental Testing and Analysis of Spiral-Helical Surface Water Heat Exchangers. M.S. Thesis. Oklahoma State University: Stillwater, OK.

Heffernan, V. 2001. Toronto Waterfront: Toronto Cools Off Naturally - A Deep Lake Water Cooling System. *Canadian Consulting Engineer.* 2001(12): 22-24.

Holman, J. P. and W. J. Gajda. 1984. *Experimental Methods for Engineer,* 4th Edition. New York, NY: McGraw Hill.

Incropera, F. P., D. P. Dewitt, T. L. Bergman and A. S. Lavine. 2007. *Fundamentals of Heat and Mass Transfer,* 6th Edition. Hoboken, NJ: John Wiley and Sons, Inc.

Kavanaugh, S. P. 1991. *Ground and Water Source Heat Pumps - A Manual for the Design and Installation of Ground-Coupled, Ground Water and Lake Water Heating and Cooling Systems in Southern Climates.* Tuscaloosa, AL: University of Alabama.

Kavanaugh, S. P. and M. C. Pezent. 1990. Lakewater Applications of Water-to-air Heat Pumps. *ASHRAE Transactions.* 96(1): 813-820.

Kavanaugh, S. P. and K. Rafferty. 1997. *Ground Source Heat Pumps: Design of Geothermal Systems for Commercial and Institutional Buildings,* Atlanta, GA: American Society of Heating, Refrigeration, and Air-Conditioning Engineers.

Leraand, T. K. and J. C. Van Ryzin. 1995. Air Conditioning with Deep Seawater: A Cost-effective Alternative for West Beach, Oahu, Hawaii. *OCEANS '95. MTS/IEEE. Challenges of Our Changing Global Environment.* San Diego, CA, October 9-12. 2: 1100-1109.

Liu, X., S. J. Rees and J. D. Spitler. 2003. Simulation of a Geothermal Bridge Deck Anti-icing System and Experimental Validation. *Proceedings of the Transportation Research Board 82nd Annual Meeting.* Washington, D.C. January 12-16.

Lockhart, D. 2013. Telephone conversation with author, Feburary 15, 2013.

Mitchell, M. S. and J. D. Spitler. 2013. Open-loop Direct Surface Water Cooling and Surface Water Heat Pump Systems -- A Review. *HVAC&R Research.* 9(2): 125-140.

Nelder, J. A. and R. Mead. 1965. A Simplex-method for Function Minimization. *Computer Journal.* 7(4): 308-313.

Peer, T. 2012. Email conversation with author, August 7, 2012.

Peer, T. and W. S. Joyce. 2002. Lake Source Cooling. *ASHRAE Journal.* 44(4): 37-39.

Polypipe 2013. PolyPlus PE3408/4710 High Performance Pipe for Municipal & Industrial Appolications. PolyPipe. URL: http://www.duraline.com/sites/default/files/downloads/DL_PP_M&I_PolyPlus.pdf. Accessed: June 15, 2012.

Rauwendaal, C. 1986. *Polymer Extrusion,* New York, NY: Macmillan Publishing Company.

Rogers, G. F. C. and Y. R. Mayhew. 1964. Heat Transfer and Pressure Loss in Helically Coiled Tubes with Turbulent Flow. *International Journal of Heat and Mass Transfer.* 7(1): 1207-16

Seban, R. A. and E. F. McLaughlin. 1963. Heat Transfer in Tube Coils with Laminar and Turbulent Flow. *International Journal of Heat and Mass Transfer.* 6: 387-395.

Selvakumar, M. 2013. Appliation of Lake and Surface Water Heat Exchanger Simulations for Energy Calculations and Determination of Design Temperature Constraints. M.S. Thesis Oklahoma State University: Stillwater, OK.

Steinhart, J. S. and S. R. Hart. 1968. Calibration curves for thermistors. *Deep Sea Research and Oceanographic Abstracts.* 15(4): 497-503.

Sumner, J. A. 1948. The Norwich Heat Pump. *Industrial and Mechancial Engineering.* 156: 22-29.

Svensson, T. and L.-O. Sörman. 1982. In Swedish--Värmeupptangning med bottenförlagda slangar i stillastående vatten. Report: Series B:36. Götenberg, Sweden: Chalmers University of Technology.

Svensson, T. and L.-O. Sörman. 1983. In Swedish--Värmeupptangning med bottenförlagda slangar i rinnande vatten. *Sjövärmesystem.* Stockholm, Sweden, May, 1982. 14-28. Stockholm, Sweden: Byggforskningsrådet.

Taylor, J. R. 1997. *An Introduction to Error Analysis - The Study of Uncertainties in Physical Measurements,* 2nd Edition. Sausilito, CA: University Science Books.

VITA

Matt Sandy Mitchell

Candidate for the Degree of

Masters of Science

Thesis: EXPERIMENTAL INVESTIGATION AND DESIGN TOOL DEVELOPMENT FOR SURFACE WATER HEAT PUMP SYSTEMS

Major Field: Mechanical and Aerospace Engineering

Biographical:

Personal Data: Born in Rexburg Idaho in August of 1984.

Education:

Received a Bachelors of Science in Mechanical Engineering from Brigham Young University–Idaho, Rexburg, Idaho in July 2010.
Completed the requirements for the degree of Master of Science with a major in Mechanical and Aerospace Engineering at Oklahoma State University in December, 2013.

Experience:

After completion of the B.S. degree, worked for Applied Engineering Services in Idaho Falls, ID as a Designer for 8 months prior to attending Oklahoma State University.

Professional Affiliations:

Student member: ASME, ASHRAE.